The NTHMP Landslide Tsunami Benchmark Workshop, Galveston, January 9-11, 2017

James T. Kirby[1], Stephan T. Grilli[2], Cheng Zhang[1], Juan Horrillo[3],
Dimitry Nicolsky[4],Philip L.-F. Liu[5]

[1]Center for Applied Coastal Research
Department of Civil and Environmental Engineering,
University of Delaware, Newark, DE 19716 USA
[2]Department of Ocean Engineering, University of Rhode Island,
Narragansett RI 02882 USA
[3]Department of Maritime Systems Engineering, Texas A&M University at Galveston
Galveston, TX
[4]Geophysical Institute, University of Alaska Fairbanks, Fairbanks, AK 99709 USA
[5]School of Civil and Environmental Engineering
Cornell University, Ithaca, NY USA,
and
Department of Civil and Environmental Engineering
National University of Singapore, Singapore

Research Report CACR-18-01
Center for Applied Coastal Research, Department of Civil and Environmental Engineering
University of Delaware, Newark DE 19716 USA

Work supported by Grant NA15NWS4670029 from the
National Tsunami Hazard Mitigation Program (NOAA) to the University of Delaware.

July 23, 2018

Abstract

A landslide tsunami model benchmarking and validation workshop was held, January 9-11, 2017 in Galveston, TX. This workshop, which was organized on behalf of NOAA-NWS's National Tsunami Hazard Mitigation Program (NTHMP) Mapping and Modeling Subcommittee (MMS), followed the template of earlier NTHMP-MMS model benchmarking workshops held in Galveston, TX (*Horrillo et al.*, 2014) and Portland, OR (*Lynett and thirty-seven alia*, 2017)), with the expected outcome being to develop: (i) a set of community accepted benchmark tests for validating models used for landslide tsunami generation and propagation in NTHMP inundation mapping work; (ii) workshop documentation and a web-based repository, for benchmark data, model results, and workshop documentation, results and conclusions, and (iii) provide recommendations as a basis for developing best practice guidelines for landslide tsunami modeling in NTHMP work.

A set of seven benchmark tests were selected by the steering committee, in coordination with the complete MMS committee, of which 3 were identified to perform detailed model/data and model/model comparisons. These consisted of a 3D laboratory test of a sliding solid mass, a 2D laboratory test of a deforming submarine landslide, and a field case describing submarine landslides in Port Valdez, AK during the 1964 Alaska Earthquake. Potential participants with interest and expertise in landslide tsunami modeling, experiment,s and field work, were invited to attend the workshop and given information on how to access the benchmark data. Eventual workshop participants included NTHMP modelers and investigators (13), a group of multi-disciplinary experts both US-based and international (15), USGS experts (3), plus a few additional participants from the private sector (2). Participants who were modelers were invited to simulate as many benchmarks as possible, with a minimum of 2 among the 3 benchmarks specified for more in-depth comparisons. Each modeler or modeling group were asked to apply their own model and submit all results, in a specified format for each benchmark, to the steering committee before the workshop. Results were presented by each group and compared during the workshop, and discrepancies with the benchmarking data and among models were discussed.

Models ranging from non-dispersive, nonlinear shallow water equation (NLSWE) type to full Navier-Stokes solvers were applied and their results compared to the reference benchmark data; model results were also compared to each other to determine consistency within model type or class. The most obvious outcome of the model/data comparison was that models of NLSWE type were found to be inappropriate for describing seaward propagation of landslide-generated waves for almost any distance away from the source region for the events considered. In contrast, all models which retained a degree of frequency dispersion were seen to be adequate in predicting wave evolution away from the source region, with comparable accuracy seen for Navier-Stokes models and non-hydrostatic models at all distances and with a slow increase in error with distance noted for Boussinesq models. The marked discrepancy between NLSWE models and other models was less distinct in the field benchmark case, where results from different models were more different largely due to variations in model setup.

The workshop steering committee was composed of Drs. J.T. Kirby and S.T. Grilli (co-chairs), and Drs. J. Horrillo, and D. Nicolsky, all MMS members, and Dr. P. L.-F. Liu, who served as external evaluator.

Contents

List of Figures

List of Tables

1 Introduction

1.1 Background

In its FY2009 Strategic Plan, the NTHMP required that all numerical tsunami inundation models be verified as accurate and consistent through a model benchmarking workshop/process. This was completed in FY2011, but only for seismic tsunami sources and in a limited manner for idealized solid underwater landslides. Recent work by various NTHMP states/areas, however, has shown that landslide tsunami hazard may be dominant along significant parts of the US coastline, as compared to hazards from other tsunamigenic sources.

- Along the US East Coast, a large volcanic subaerial landslide tsunami on La Palma (Canary Islands) is the dominant, albeit long return period, tsunami source (*Ward and Day*, 2001; *Løvholt et al.*, 2008; *Abadie et al.*, 2012; *Tehranirad et al.*, 2015). Many large underwater landslide scars, some a few 10Ka old, have been mapped by USGS (*ten Brink and alia*, 2008; *ten Brink et al.*, 2014) along the continental shelf slope and Atlantic Margin; more recent USGS work (*Chaytor et al.*, 2016) also shows large potential landslides in or near the Florida straight. Earlier work has shown that many of these landslides would have been strongly tsunamigenic (*Geist et al.*, 2009; *Grilli et al.*, 2009, 2015). In 1929, in this broad geographic area and oceanic margin, a large landslide tsunami was triggered off of the Grand Banks by a M7.1 local earthquake, which caused extensive inundation and over 20 fatalities along the Newfounland coasts (*Fine et al.*, 2005).

- In the Gulf of Mexico, the majority of the tsunami inundation mapping work that is being done as part of NTHMP (*Horrillo et al.*, 2013) is based on a few major underwater landslide, also mapped by USGS (*ten Brink and alia*, 2008).

- In California, Oregon and Washington states, while both local and far-field seismic sources likely dominate tsunami hazard, many large historical landslides have been mapped which were also likely to have been strongly tsunamigenic. Notable examples in California include the Goleta slide off of Santa Barbara (*Greene et al.*, 2005) and the Big Sur slide in the Monterey Canyon (*Greene and Ward*, 2003). Recent work on the Tohoku 2011 tsunami (e.g., *Tappin et al.* (2014)) indicates that very large megathrust earthquakes (such as anticipated in the future for the Cascadia subduction zone), may also trigger very large landslides which could contribute significant additional wave activity in addition to the co-seismic tsunami. Hence, their study, siting and modeling should be done ahead of time, in preparation for such large seismic events.

- In Alaska, numerous landslides, both underwater and subaerial, have been triggered by large earthquakes (e.g., the M9.2 1964 event; *Ichinose et al.* (2007)) and artesian flows, and have caused tsunamis with significant local runup and inundation. In

this region, the most notable such event is the Lituya Bay 1958 subaerial slide that triggered a tsunami in a narrow fjord, causing over 500 m runup on the other side of the fjord (*Fritz et al.*, 2001, 2009; *Weiss et al.*, 2009).

- Hawaii, larger landslides associated with volcano flank motion and collapse have occurred (e.g., Kalapana 1975; *Day et al.* (2005)) causing significant runup. Such events will continue to occur in the future as a result of the continuous build up and weathering of volcanoes.

- Puerto Rico, a number of large historical landslide tsunami events have been mapped by USGS and modeled (e.g., in the Mona passage; *López-Venegas et al.* (2008, 2015)).

In past years, there has been considerable model development and benchmarking activity for seismically induced tsunamis, in particular under the auspice of NTHMP: the Galveston benchmarking workshop for tsunami elevations in 2011 (*Horrillo et al.*, 2014) as well as the 2015 Portland workshop for tsunami velocities in 2015 (*Lynett and thirty-seven alia*, 2017). For landslide tsunamis, however, both the model development and benchmarking efforts have been lagging. In 2003, the east coast NTHMP principal investigators (PIs), Kirby and Grilli, and Dr. Liu, were co-organizers of a NSF sponsored landslide tsunami workshop in Hawaii, and a similar follow-up workshop took place on Catalina island in 2006. Since then, to our knowledge, no similarly large and comprehensive benchmarking workshop has been organized. In 2011, following the NTHMP model benchmarking workshop, Horrillo, the Gulf of Mexico NTNMP PI, organized a landslide tsunami workshop devoted to a review of the state-of-the-art in modeling. Later that year, the USGS Woods Hole group (ten Brink, Chaytor, and Geist) organized a similar workshop, during which the state-of-the-art in field work, geology, Probabilistic Tsunami Hazard Assessment (PTHA), and landslide tsunami modeling were reviewed.

A decade ago, investigators were both challenged and satisfied with modeling solid block landslides (e.g., *Grilli and Watts*, 1999, 2005; *Grilli et al.*, 2002; *Lynett and Liu*, 2003; *Watts et al.*, 2003, 2005; *Liu et al.*, 2005) and laboratory experiments were developed for those cases and used for tsunami model benchmarking (in particular, as part of the Galveston 2011 workshop, experiments by *Enet and Grilli* (2007) were used for landslide tsunami benchmarking; see also *Ataie-Ashtiani and Najafi-Jilani* (2008)). In contrast, some early models (e.g., *Heinrich*, 1992; *Harbitz et al.*, 1993; *Assier-Rzadkiewicz et al.*, 1997; *Fine et al.*, 1998) and a number of more recent models have simulated tsunami generation by deformable slides, based either on depth-integrated two-layer model equations, or on solving more complete sets of equations in terms of featured physics (dispersive, non-hydrostatic, Navier-Stokes). Examples include solutions of 2D or 3D Navier-Stokes equations to simulate subaerial or submarine slides modeled as dense Newtonian or non-Newtonian fluids (*Ataie-Ashtiani and Shobeyri*, 2008; *Weiss et al.*, 2009; *Abadie et al.*, 2010, 2012; *Horrillo et al.*, 2013), flows induced by sediment concentration (*Ma et al.*, 2013), or fluid or granular flow layers penetrating or failing underneath a 3D water domain (for ex-

ample, the two-layer models of *Kirby et al.*, 2016; *Ma et al.*, 2015, in which the upper water layer is modeled with the non-hydrostatic σ-coordinate 3D model NHWAVE (*Ma et al.*, 2012)). For a more comprehensive review of recent modeling work, see *Yavari-Ramshe and Ataie-Ashtiani* (2016).

A number of recent laboratory experiments have modeled tsunamis generated by subaerial landslides made of gravel (*Fritz et al.*, 2004; *Ataie-Ashtiani and Najafi-Jilani*, 2008; *Heller and Hager*, 2010; *Mohammed and Fritz*, 2012) or glass beads (*Viroulet et al.*, 2014). For deforming underwater landslides and related tsunami generation, 2D experiments were performed by *Assier-Rzadkiewicz et al.* (1997), who used sand, and *Ataie-Ashtiani and Najafi-Jilani* (2008), who used granular material. Well-controlled 2D glass bead experiments were reported and modeled by *Grilli et al.* (2017) using the model of *Kirby et al.* (2016).

1.2 Organization and time line

At the summer NTHMP meeting in 2014, the NTHMP-MMS recommended that a landslide tsunami model benchmarking workshop be organized in the near future on behalf of NTHMP. Following this recommendation, as part of their FY15 NTHMP project, J.T. Kirby (University of Delaware) and S.T. Grilli (University of Rhode Island) received funding to organize and conduct such a workshop, as co-chairs, following the template of other similar workshops organized in the past, in Galveston in 2011 and in Portland in 2015. To help them preparing the workshop scientific program and select and prepare benchmark problems, a steering committee led by the two co-chairs was formed, including Drs. J. Horrillo (Texas A&M University - Galveston) and D. Nicolsky (University of Alaska), who are NTHMP-MMS members. The committee met during the NTHMP 2016 annual and 2016 summer meetings and conducted conference calls to develop the workshop agenda and tentatively select a set of relevant landslide tsunami benchmarks (analytical, numerical, experimental, and field). In the summer 2016, a non-NTHMP external evaluator, Dr. P.L.-F. Liu (Cornell University) was identified, who accepted to join the organizing committee and help in selecting and reviewing the proposed benchmarks, workshop plans, and outcomes. Dr. Liu was also tasked to provide an objective and impartial opinion with respect to the stated performance of the various models being benchmarked and validated. Since the long wave workshop he organized in Catalina in 1990, Dr. Liu has organized many tsunami benchmarking workshops and been a leader in the community in tsunami modeling, experiments, and field work. He co-organized, with the PIs, the 2003 landslide tsunami NSF workshop in Hawaii and has performed (solid block) landslide tsunami experiments that have been used as benchmarks by others (*Liu et al.*, 2005, , see Benchmark 3 below).

By the end of summer 2016, a workshop webpage was built by the co-chairs as a receptacle for the benchmark information and data, as well as other practical information regarding the workshop (www.udel.edu/kirby/landslide/). The workshop dates and venue

were selected by the committee to be January 9-11, 2017 in Galveston, TX. The steering committee finalized the benchmark selection based on a subset of available laboratory date sets for solid slide experiments and deformable slide experiments, including both submarine and subaerial slides (see discussion and references above that motivated this selection). One benchmark based on a historic field event (Valdez, AK, 1964) was also selected and developed. All the necessary benchmark data was acquired and validated by steering committee members and posted on the workshop webpage by the end of September 2016 (see details below).

Potential participants were then invited to attend the workshop and given information on how to access the data. These prospective participants included NTHMP modelers and investigators (about 10), together with a group of selected experts both US-based and international (about 15) and USGS experts (5), plus a few additional participants from the private sector. A participant list with affiliations is given later. Participants who were modelers were invited to simulate as many benchmarks as possible, with a minimum of 2 mandatory specified benchmarks (see below) to warrant financial support to attend the workshop. Each modeler or modeling group were asked to apply their own model and submit all results, in a specified format for each benchmark, to the steering committee before the workshop. Results were to be presented by each group and compared during the workshop, and discrepancies with the benchmarking data and among models discussed.

Although this was anticipated to be a more challenging exercise than for seismic tsunamis, owing to the wider variety of rheologies and types of landslide, and of models applied to those, the goal of the workshop was for participants to attempt to reach a consensus at the end of the workshop, on both acceptable modeling approaches (and associated model classes) for various types of landslide tsunamis, and acceptable levels of discrepancies with various types of benchmarking data.

Finally, it was planned for the scientific committee to prepare a workshop proceedings (this document) and a manuscript for publication in a peer-reviewed journal based on the workshop findings, as done for earlier workshops in Galveston 2011 (*Horrillo et al.*, 2014) and Portland 2015 (*Lynett and thirty-seven alia*, 2017).

1.3 Objectives

The objectives and expected outcome of the NTHMP Landslide Tsunami Benchmark Workshop were to develop: (i) a set of community accepted benchmark tests for validating models used for landslide tsunami generation and propagation in NTHMP inundation mapping work; (ii) workshop documentation and a web-based repository for benchmark data, model results, and workshop documentation, results and conclusions. This report presents the chosen benchmark tests, and describes the technical findings based on model/data and model/model comparisons. An associated web site (http://www.udel.edu/kirby/landslide/) provides links to benchmark data, model results, analysis tools, individual modeler write-ups, and documentation of additional invited presentations (where available).

2 Workshop participants and list of presentations

Figure 1: Workshop participants: Front, L-R: Finn Løvholt, Ray Cakir, Giorgio Bellotti, Jorge Macias, Stephan Grilli, Dmitry Nicolsky, Fatemah Nemati, Rick Wilson. Second Row: Stéphane Abadie, Isaac Fine, Aurelio Mercado, Juan Horrillo, Stephanie Ross, Lauren Schambach, Olivier Kimmoun, Pat Lynett, Phil Liu. Back: Wei Cheng, Jim Kirby, Dave Tappin, Fengyan Shi, Cheng Zhang, Hermann Fritz, Jason Chaytor, Homma Lee, Brendan Dooher, Alberto Lopez.

2.1 Workshop participants

The NTHMP Landslide Tsunami Benchmark Workshop was attended by 33 participants (see Fig. 1), in Galveston, TX; January 9-11, 2017 (if clearly demonstrated, the primary fields of each participant is marked in parentheses):

1. Abadie, Stéphane; Université de Pau et Des Pays de L'Adour, Anglet, France (modeling)
2. Bellotti, Giorgio; Universitá di Roma Tres, Rome, Italy (modeling and experiments)
3. Cakir, Ray; Washington Dept. of Natural Resources, Olympia, WA
4. Chaytor, Jason; U.S. Geological Survey, Woods Hole, MA (field work)
5. Cheng, Wei; Texas A&M University at Galveston, Galveston, TX (modeling)

6. Dooher, Brendan; Pacific Gas & Electric Co., San Ramon, CA (geohazard, industry)
7. Fine, Isaac; Institute of Ocean Sciences, BC, Canada (modeling)
8. Fritz, Hermann; Georgia Tech, Atlanta, GA (experiments and field work)
9. Grilli, Stephan; University of Rhode Island, Narragansett, RI (modeling and experiments)
10. Horrillo, Juan; Texas A&M University, Galveston, TX (modeling)
11. Kian Kian, Rozita; Texas A&M University, Galveston, TX (modeling)
12. Kimmoun, Olivier; Ecole Centrale Marseille, France (modeling and experiments)
13. Kirby, Jim; Center for Applied Coastal Research, University of Delaware, Newark, DE (modeling and experiments)
14. Lee, Homa USGS Coastal and Marine Geology Program, Montara, CA (field work)
15. Liu, Philip L-F; Cornell University, Ithaca, NY and National University of Singapore (modeling and experiments)
16. Lo, Hong-Yueh (Peter); Cornell University Ithaca, NY (modeling)
17. Lopez, Alberto; University of Puerto Rico Mayaguez, PR (modeling)
18. Løvholt, Finn; Norwegian Geotechnical Institute Oslo, Norway (modeling)
19. Lynett, Patrick; University of Southern California, Los Angeles, CA (modeling, experiments and field work)
20. Ma, Gangfeng; Old Dominion University, Norfolk, VA (modeling)
21. Macias, Jorge; University of Málaga, Málaga, Andaluca, Spain (modeling)
22. Mercado-Irizarry, Aurelio; University of Puerto Rico Mayaguez, PR (geohazard)
23. Misra, Shubhra; Chevron Corp., Houston, TX (geohazard, industry)
24. Nemati, Fatemeh; University of Rhode Island, Narragansett, RI (modeling)
25. Nicolsky, Dmitry; University of Alaska at Fairbanks, Fairbanks, AK (modeling)
26. Ross, Stephanie; U.S. Geological Survey, Menlo Park, CA (field work)
27. Salaree, Amir; Northwestern University, Evanston, IL
28. Schambach, Lauren; University of Rhode Island, Narragansett, RI (modeling)

29. Shi, Fengyan; University of Delaware, Newark, DE (modeling)
30. Sunny, Richard C.; Texas A&M University, College Station, TX
31. Tappin, David; British Geological Survey, Nottingham, United Kingdom (field work)
32. Wilson, Rick; California Geological Survey, Sacramento, CA (geohazard, field work)
33. Zhang, Cheng; University of Delaware, Newark, DE (modeling)

2.2 Agenda of presentations

Day 1: Monday January 9th

- 9-9:15 Welcoming, logistics - Horrillo, Girimaji
- 9:15-9:45 Rationale and goals for present workshop - Stephan Grilli
- 9:45-10:00 Review of previous benchmarking workshops - Philip Liu
- 10-10:30 "The Geology of Submarine Landslide Tsunamis" - David Tappin
- 10:30-11 Break
- 11-11:45 Description of benchmark problems - Jim Kirby
- 11:45-12:15 "Physical Modeling of Tsunamis generated by 2D and 3D granular Landslides in various Scenarios from Fjords to conical Islands" -Hermann Fritz
- 12:15-1:45 Lunch
- 1:45-1:50 Quick intro to organization of modeling talks - Jim Kirby
- 1:50-2:20 Model descriptions and results: Landslide-HySEA - Jorge Macias
- 2:20-2:35 Model descriptions and results: Alaska GI'-L - Dmitry Nicolsky
- 2:35-2:55 Model descriptions and results: FBSlide - Isaac Fine
- 2:55-3:10 "New experiments on landslide tsunami on a conical island" - Giorgio Bellotti
- 3:10-3:35 Break
- 3:35-3:55 "The Tsunami Generated by the October 17, 2015 Taan Fjord Landslide" - Pat Lynett
- 3:55-4:20 Model descriptions and results: Globouss and BoussClaw - Finn Løvholt
- 4:20-4:45 Model descriptions and results: LS3D and 2LCMFLOW - Behzad Ataie-Ashtiani (Kirby presenting)

Day 2: Tuesday January 10th

- 9-9:15 Summary of Day 1 - Grilli

- 9:15-9:55 "Characterizing East and Gulf Coast Landslide Sources" - Jason Chaytor
- 9:55-10:45 Model descriptions and results: NHWAVE - Gangfeng Ma, Cheng Zhang, Stephan Grilli, Fengyan Shi
- 10:45-11:15 Break
- 11:15-11:55 Model descriptions and results: Tsunami3D - Juan Horrillo
- 11:55-12:25 "Small scale experiments of subaerial and submarine landslides" - Olivier Kimmoun
- 12:25-1:45 Lunch
- 1:45-2:05 Model descriptions and results: Coulwave, mild-slope equation - Pat Lynett
- 2:05-2:20 Brief intro to SPH modeling of slides - Phil Liu
- 2:20-2:50 Model descriptions and results: THETIS - Stephane Abadie
- 2:50-3:20 "Geotechnical and Geologic Constraints on Tsunamigenic Submarine Landslides" - Homma Lee
- 3:20-3:45 Break
- 3:45-5:00 Comparison of model results for benchmarks 2, 4 and 7 - Jim Kirby

Day 3: Wednesday January 11th

- 9-9:10 Summary of Day 2
- 9:10-9:30 Discussion of development of a data and modeling web repository - Kirby and Grilli
- 9:30-10:45 Discussion: Topics to be determined based on participant interest.
- 10:45-11:00 Closure

2.3 Web resources

The website http://www.udel.edu/kirby/landlside/, provides a detailed overview of the chosen benchmark tests and workshop agenda. The website has been augmented with a new section that provides this technical report, links to individual modeler writeups, additional invited presentations, and formatted model output, analysis results, and matlab tools used to perform the analysis. This part of the website may be accessed directly at http://www.udel.edu/kirby/landslide/reporting.html.

3 Description of Benchmarks

This section describes seven benchmark tests (or test configurations with multiple examples) that were chosen prior to the workshop. Of these, modelers were asked to carry out tests for Benchmarks 2, 4 and 7. Analysis of these results is provided in Section 6.

Each of the seven following sections is adapted from the corresponding benchmark web page. References here to filenames for provided benchmark data correspond to live links on the web page version. References for the corresponding web pages are included in the title of each section below.

3.1 Benchmark 1: Two-dimensional submarine solid block (http://www.udel.edu/kirby/landslide/problems/benchmark_1.html)

This benchmark problem is based on the 2D laboratory experiments of *Grilli and Watts* (2005). The geometry of the slide is shown in Figure 2.

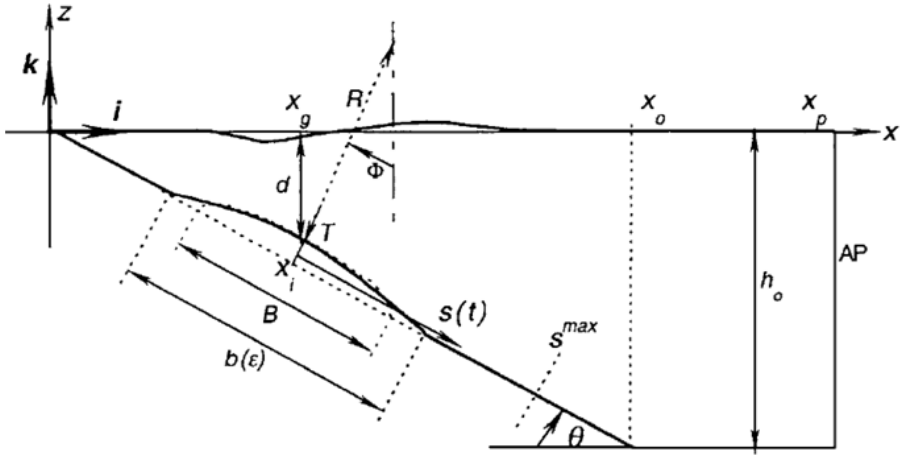

Figure 2: Sketch of main parameters and variables for wave generation by 2D slide (*Grilli and Watts*, 2005).

The 2D slide model is semi-elliptical, lead-loaded, and rolling down a smooth slope with $\theta = 15^\circ$ (2 mm above the slope), in between two vertical side walls, 20 cm apart (Figure 3). The water depth is $h_0 = 1.05$ m. Melted lead was poured in a central cavity in the model, to achieve an average density 1.806 in the fresh water tank, corresponding to ρ_l =1,850 kg/m^3 in sea water of density ρ_w = 1,025 kg/m^3. The model dimensions were length $B = 1$ m, maximum thickness $T = T_{ref} = 0.052$ m, and width $w = 0.2$ m. The model initial submergence d was varied in experiments and the free surface elevation

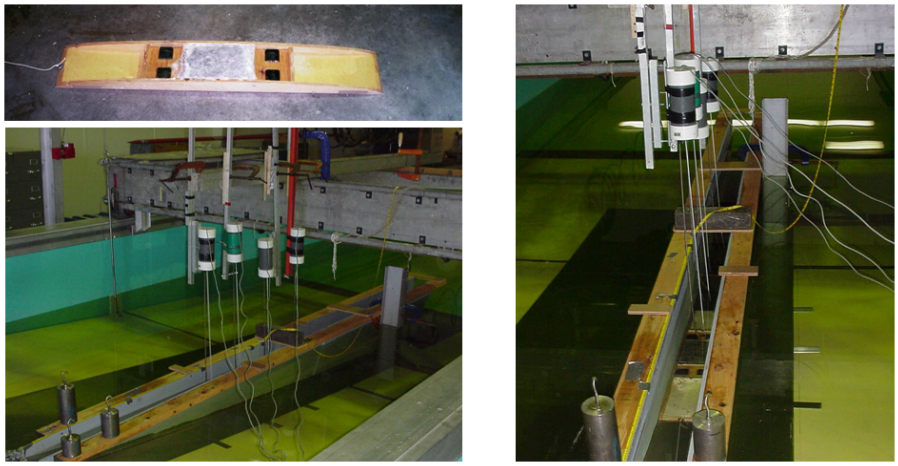

Figure 3: Experimental set-up, with views of sidewalls, capacitance wave gages, and lead-loaded rolling semi-elliptical slide model (*Grilli and Watts*, 2005).

recorded at 4 capacitance wave gauges installed at locations: $x = 1.175, 1.475, 1.775, 2.075$ m, the first location being identical to x_g (Figure 2).

A micro-accelerometer was embedded at the model center of mass and inclined perpendicular to the slope, which recorded the slide acceleration in experiments. The latter was twice integrated to obtain the slide center of mass motion as a function of time $S(t)$. This motion was found to be highly repeatable in replicates of experiments and through curve fitting, after a short acceleration ramp-up over time t_i (see details in *Grilli and Watts*, 2005, Appendix), to match well the theoretical law of motion

$$\frac{S}{S_0} = \ln\left\{\cosh\left(\frac{t}{t_0}\right)\right\} \tag{1}$$

with

$$t_0 = \frac{u_t}{a_0}; \qquad S_0 = \frac{u_t^2}{a_0} \tag{2}$$

being the characteristic time and distance of motion, respectively, defined as a function of the terminal slide velocity u_t and the slide initial acceleration a_0. For $d = d_{ref} = 0.259$ m, measurements yielded : $a_0 = 0.75$ m/s^2, $t_i = 0.09$ s, $t_0 = 1.677$ s, and $S_0 = 2.110$ m.

Figure 4 shows a comparison for this case of experimental results with numerical simulations (Fully Nonlinear Potential Flow BEM model) for the surface elevation at the 4 selected wave gages $g0 - g1$ located at $x/h_0 =$ a) 1.175, b) 1.475, c) 1.775, d) 2.075 or $x = 1.234, 1.549, 1.864, 2.179$ m (Figure 2). The original data for two replicates of one of

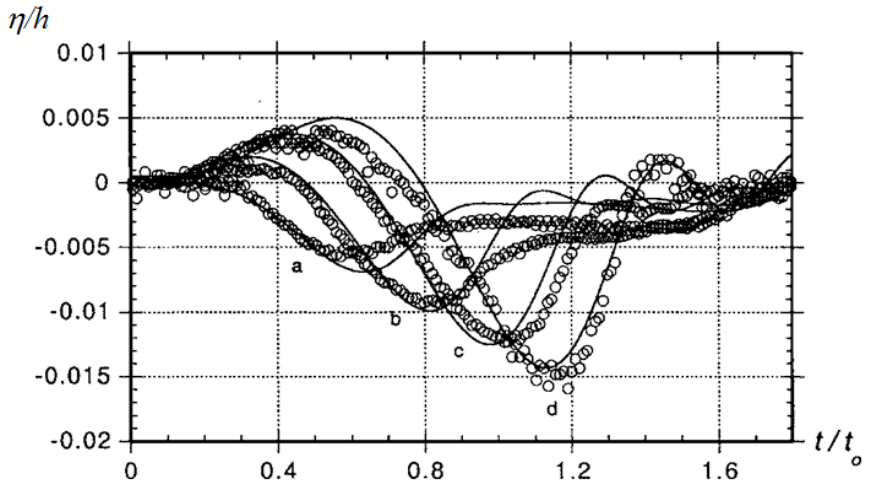

Figure 4: Wave generation by 2D slide (Figures 2, 3), for $d = d_{ref} = 0.259$ m. Time series of non-dimensional surface elevation η/h_0, in laboratory experiments (o) and simulations (-), measured/computed at 4 wave gauges g0-g1 located at x/h_0 = a: 1.175, b:1.475, c:1.775, d: 2.075. Horizontal axis is non-dimensional time t/t_0 (*Grilli and Watts*, 2005).

Grilli and Watts experiments was located and plotted in Figure 5 (trials 4 and 5) of this experiment. Because there were a few replicates of each experiment, those in Figure 5 are not exactly the same data as shown in Figure 4, which may have resulted from averaging of replicates of the experiment. Also, there appears to be some high-frequency noise in the original data (which in the data files is given at 200 Hz, unlike the 100 Hz noted in the paper), which may have been filtered out to produce Figure 4.

3.1.1 Provided data

Time series of raw data from Figure 5 were provided in Matlab formatted mat files *bench1_trial4.mat* and *bench1_trial5.mat* and in excel format as *bench1_trial4.xls* and *bench1_trial5.xlsx*. (Data files may be obtained online for this and the following benchmarks by referring to the individual benchmark pages on the Landslide Tsunami Workshop website http://www.udel.edu/kirby/landslide/ or at the NTHMP website.)

3.1.2 Benchmark problem

The benchmark here consists of using the above information on slide shape, density, submergence and kinematics, together with reproducing the experimental set-up to simulate

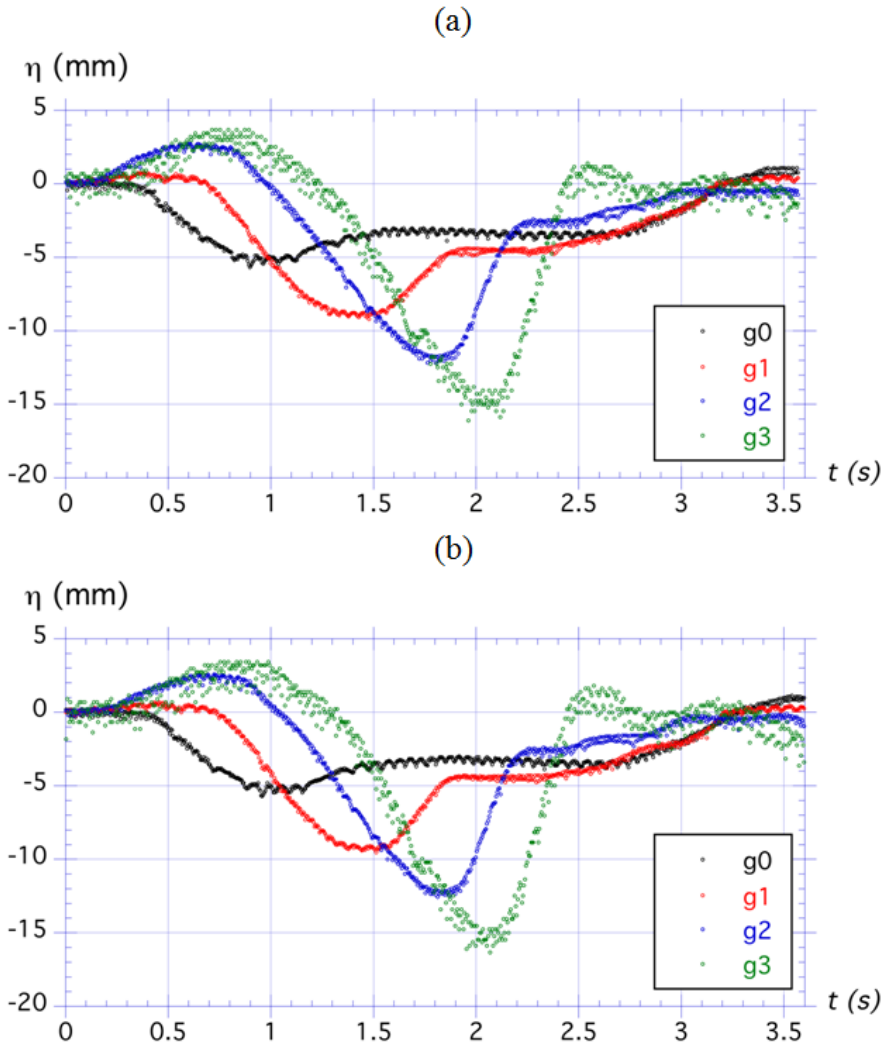

Figure 5: Wave generation by 2D slide (case of Figures 2–3). Two sets of experimental results (a: trial 4 and b: trial 5) from *Grilli and Watts* (2005) 2D slide experiments (case of Figures 2, 3) for $d = d_{ref} = 0.259$ m (Figure 4). Labels $g0$ to $g3$ denote measurements of surface elevation at gages located at $x = 1.234, 1.549, 1.864$ and 2.179m.

surface elevations measured at the 4 wave gages (average of 2 replicates of experiments), as shown in Figure 5, and present a comparison model-experiments similar to Figure 4.

3.2 Benchmark 2: Three-dimensional submarine solid block (http://www.udel.edu/kirby/landslide/problems/benchmark_2.html)

This benchmark problem is based on the 3D laboratory experiments of *Enet and Grilli* (2007). The experiments were performed in the University of Rhode Island (URI) fresh water wave tank of width 3.6 m and length 30 m, with a still water depth of 1.5 m over the flat bottom portion. The model slide slid down a plane slope built in the tank with an angle $\theta = 15°$. A definition sketch and an overview of the experiment are provided in Figures 6 and 7.

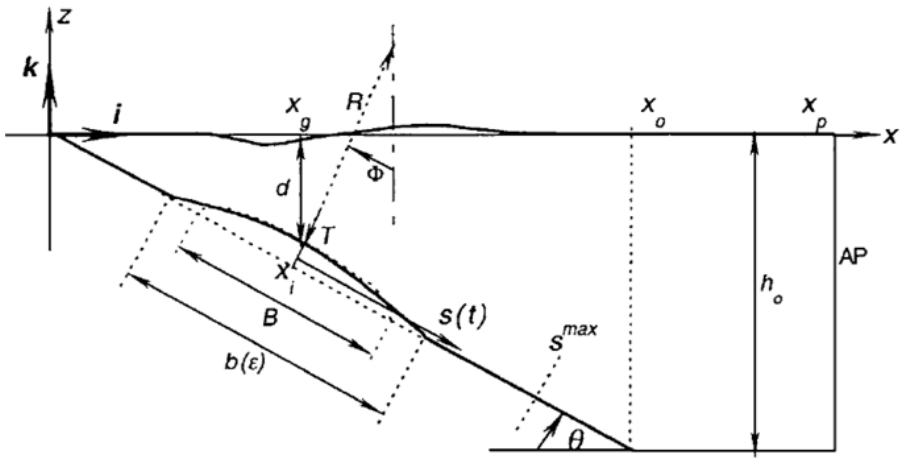

Figure 6: Sketch of main parameters and variables for wave generation by 3D slide. (*Grilli and Watts*, 2005, from).

The submarine slide model was built as a streamlined Gaussian-shaped aluminum body (Figure 8) with elliptical footprint, with down-slope length $b = 0.395$ m, cross-slope width $w = 0.680$ m, and maximum thickness $T = 0.082$ m. The slide shape is defined by

$$\zeta(\xi, \chi) = \frac{T}{1-\epsilon} \max\left[0, \mathrm{sech}(k_b \xi)\mathrm{sech}(k_w \chi) - \epsilon\right] \tag{3}$$

where

$$\begin{aligned} k_b &= \frac{2}{b}\cosh^{-1}\frac{1}{\epsilon} \\ k_w &= \frac{2}{w}\cosh^{-1}\frac{1}{\epsilon} \end{aligned}$$

and where(ξ, χ) are the local down-slope and span-wise coordinates with origin at the slide

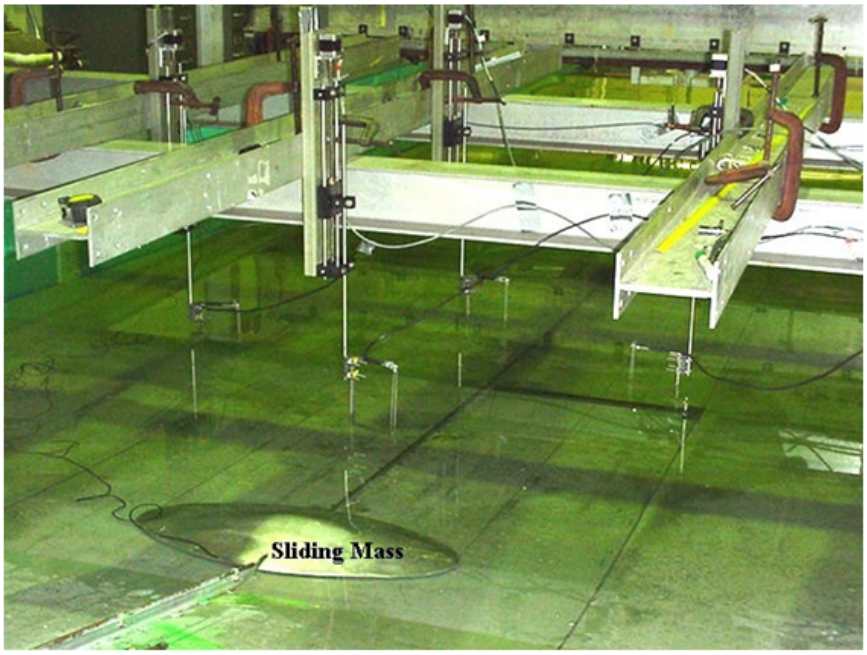

Figure 7: Wave generation by underwater 3D slide. Experimental set-up for the experiments of *Enet and Grilli* (2007).

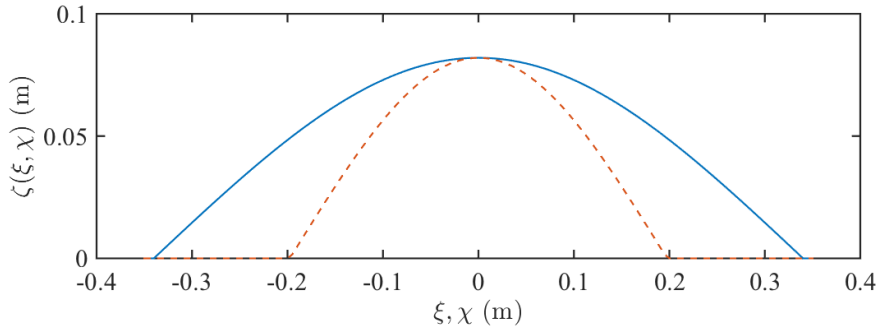

Figure 8: Vertical cross-sections of landslide model geometry defined by Eq. (3). Solid and dashed lines represent cross-sections along axes $\xi = 0, \chi = 0$ respectively. Dimensions are in meters.

center. With this geometry and parameters, the slide volume is given by

$$V_b = bwT\frac{I_2}{C^2}\left(\frac{I_1/I_2 - \epsilon}{1-\epsilon}\right) \tag{4}$$

with

$$\begin{aligned}
\begin{pmatrix} I_1 \\ I_2 \end{pmatrix} &= \int_0^C \begin{pmatrix} f \\ g \end{pmatrix} d\mu \\
f(\mu) &= \operatorname{sech}(\mu)\tan^{-1}(\sinh g) \\
g(\mu) &= \cosh^{-1}\left(\frac{\operatorname{sech}\mu}{\epsilon}\right) \\
C &= \cosh^{-1}\left(\frac{1}{\epsilon}\right)
\end{aligned}$$

This volume was measured after fabricating the slide, to $V_b = 7.72 \times 10^{-3}$ m^3, which using the above equations and slide geometric data, yields $\epsilon = 0.717$, for which the coefficient of V_b in (4) is 0.3508.

The slide was released at time $t = 0$ from a series of 7 initial submergence depths d (Figure 6; Table 1). During its motion, the slide was guided by a rail located on the slope/tank axis, using low friction wheels, and slid a short distance (4 mm) above the plane slope. For each submergence depth d, the slide initial abscissa x_i and the abscissa of the slide point of maximum thickness x_g are defined and related by

$$x_g = x_1 + T'\sin\theta = \frac{d}{\tan\theta} + \frac{T'}{\sin\theta} \tag{5}$$

with $T' = T + 0.004$m. The slide had a central cavity housing the micro-accelerometer, which is partly filled with water. Taking this into consideration, slide mass was measured as $M_b = \rho_b V_b = 16.00$ kg, and its bulk density (based on measured volume) was $\rho_b = 2.073$ kg/m^3.

Measured data included:

- slide kinematics, obtained from a composite of the slide acceleration measured using a micro-accelerometer embedded within the slide, as well as the time of passage of the slide through three electromechanical gates (see *Enet and Grilli*, 2007, for details)
- surface elevation at up to four capacitance wave gages $g1$ to $g4$ (Figure 9)
- wave runup R (i.e., maximum vertical elevation on the slope) at the tank axis $y = 0$.

Wave gauge $g1$ was moved between each experiment to always be located at ($x = x_0, y = 0$). The coordinates of gages $g2$ - $g4$ remained fixed for all tests and are given in Table 2.

The measured slide kinematics were found to have a good match to the theoretical law of motion (Eqs. (1) - (2) for Benchmark 1) derived for slides, with the terminal velocity and initial acceleration defined as

$$u_t = \sqrt{gd}\sqrt{\frac{b\sin\theta}{d}\left(1-\frac{\tan\psi}{\tan\theta}\right)\frac{(\gamma-1)}{C_d}\frac{2(f^2-\epsilon)}{f-\epsilon}} \tag{6}$$

$$a_0 = g\sin\theta\left(1-\frac{\tan\psi}{\tan\theta}\right)\left(\frac{\gamma-1}{\gamma+C_m}\right) \tag{7}$$

where g is gravitational acceleration, $\gamma = \rho_b/\rho_w$ is the slide specific gravity, C_m is the slide added mass coefficient, C_d the slide drag coefficient, and $C_n = \tan\psi$, the slide basal Coulomb friction. Based on Eq. (6), for $\epsilon = 0.717$, we find $C = 0.8616$ and $f = 0.8952$. In each experiment, the hydrodynamic coefficients C_m and C_d were calculated as least-square fits, by applying Eqs. (1) - (2) for Benchmark 1 and (6) to the measured slide kinematics (Figure 10), expressed as a composite of center of mass acceleration and time of passage at the known position of the 3 electromechanical gates (see *Enet and Grilli*, 2007, for details). Results are given in Table 1.

Experiments were performed for 7 initial submergence depths d, which are listed in Table 1, together with values of related slide parameters and some measured tsunami waves characteristics. (Note the slight difference between the actual measured value of x_g and the theoretical value, due to experimental variance.) Regarding tsunami wave elevations, Table 1 lists, for each case, the measured characteristic tsunami amplitude η_0 (maximum depression at gauge g1) and maximum runup on the tank axis R. These small runup values were measured using a small digital camera directly viewing the waterline motion over a graduated scale. One should be cautioned that runup values might have been slightly affected by effects of the slide guiding rail.

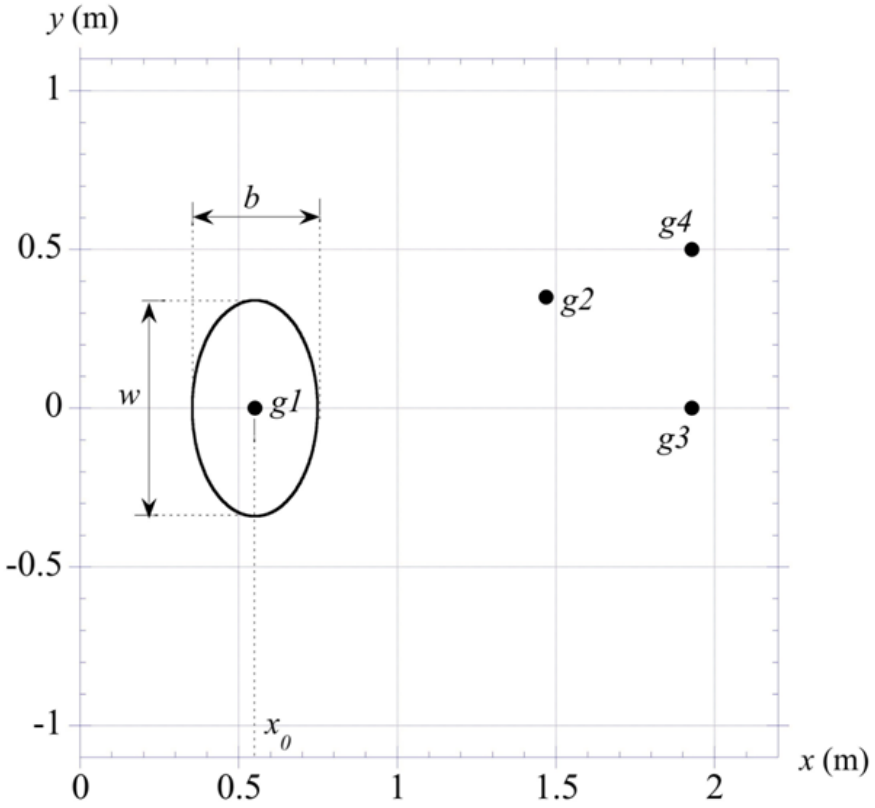

Figure 9: Wave generation by underwater 3D slide. Landslide and gage locations (Table 1). Figure is drawn for the case with $d = 61$ mm.

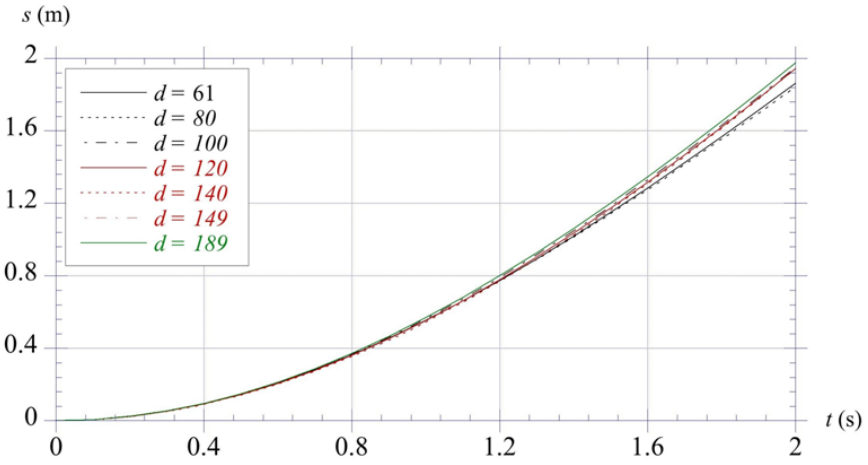

Figure 10: Wave generation by underwater 3D slide. Experimental slide kinematics, as a function of initial submergence depth d , calculated with Eqs. (1) - (2) using average experimentally fitted values of S_0 and t_0 from Table 1.

Each experiment was repeated twice, and both the raw and average time series of surface elevations $\eta(t)$ measured at gauges $g1 - g4$ are provided as data files for each experimental case in Table 1. Because raw measurements of slide kinematics were significantly processed in order to curve-fit the hydrodynamic coefficients of Table 1 corresponding to each experiment (i.e., average of 2 replicates), raw kinematics data is not provided here, but instead the curve-fitted coefficients that allow to recreate it in a numerical model, based on slide geometry and Eqs. (1) - (2) for Benchmark 1, are given in Table 1, as well as data file with the average slide kinematics (t, $S(t)$).

3.2.1 Provided data

Seven data files are provided (in both .txt and .xls format) in file *benchmark2/BENCH2.zip* which contain, for each of the 7 initial submergence depths (d = 61, 80, 100, 120, 140, 149, 189 mm), the time series of surface elevation (in mm) measured at up to 4 gages identified as $g1, g2, g3$ and $g4$. In each file, when available, results are provided for each of two experimental replicates (or runs, marked as *r1* or *r2*), done for the same initial slide parameters, and for their average (marked as *ave*). In some of these tests, some data was missing for one of the runs and/or for one of the gages. In the latter case, this is identified in the name tag given each file. For instance, *d61g1234* (*.txt* or *.xls*), indicates that these are results for depth d = 61 mm and gages $g1, g2, g3$, and $g4$. Finally, data files are all

provided as tab-delimited text files (with one line of title to skip) and excel spreadsheets. Fig. 11 shows all surface elevations available at gauges for each experiment. Solid curves are plotted for the average of 2 replicates and symbols denote partial raw data for each replicate.

Then, for each experimental case, we provide data files (*benchmark2/kinematics.txt* or *benchmark2/kinematics.xls*) containing the average kinematics $t, S(t)$ (recalculated for each average experiment using Eqs. (1) - (2) for Benchmark 1) and the values of S_0 and t_0 listed in Table 1, calculated using Eq. (6) and the other data in the table. As indicated before, Figure 10 shows a plot of the same data as given in these files; we see that the average kinematics is nearly identical for all the tests, up to 1.2 s or so. For later times, small differences in kinematics arise due to the experimental variability of the slide motion down the slope.

3.2.2 Benchmark problem

The benchmark problem consisted of using the above information on slide shape, density, submergence and kinematics (Table 1 and Figure 10), together with reproducing the experimental set-up to simulate surface elevations measured at the 4 wave gages (average of 2 replicates of experiments), such as shown in Figure 11, and present comparisons of model with experimental results, similar to Figure 12. Participants were requested to provide results for the cases with initial depth of submergence $d = 61$mm and $d = 120$mm.

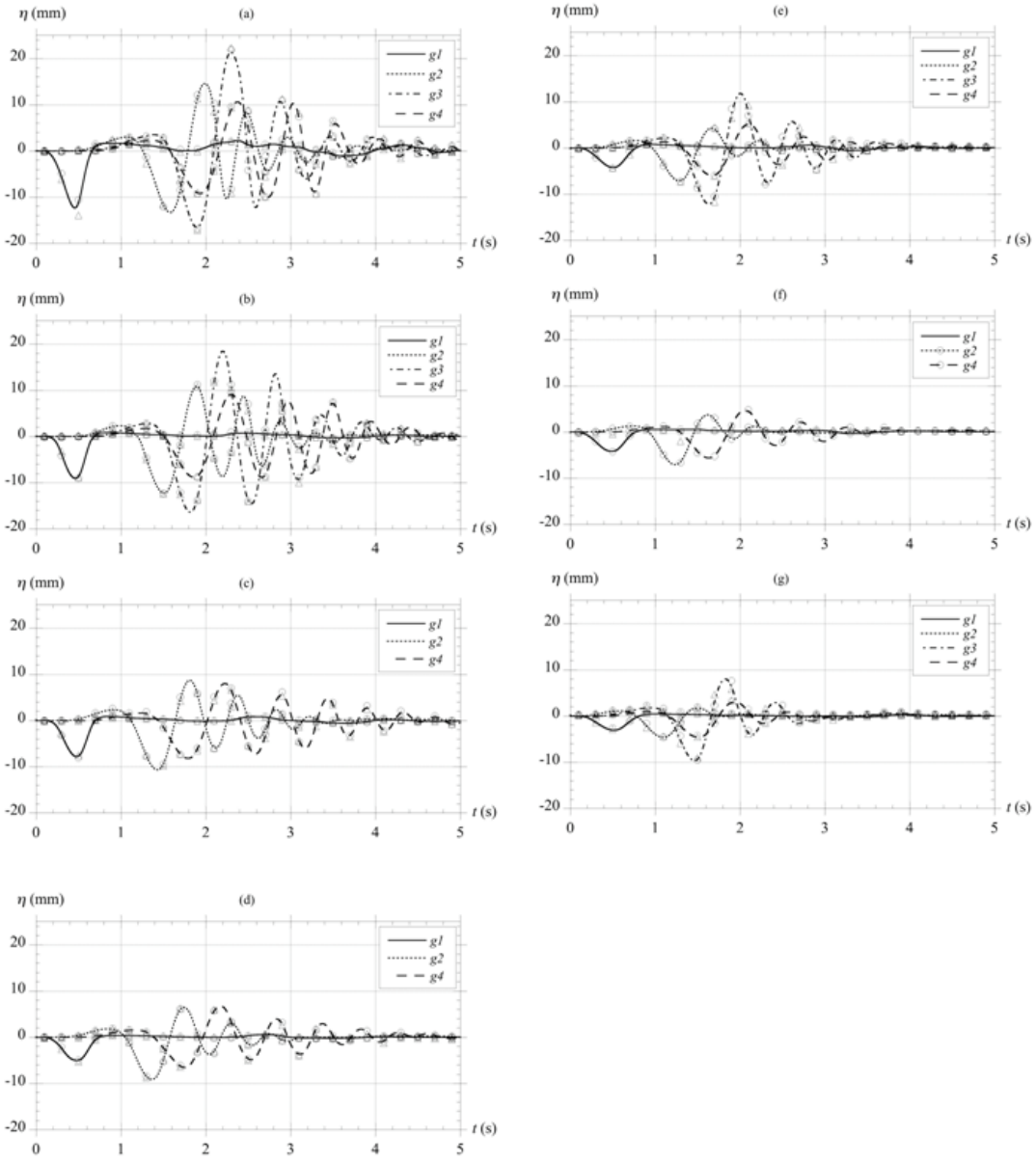

Figure 11: Surface elevation measured at gauges $(g1, g2, g3, g4)$ in 3D submarine slide experiments. Symbols (o) and (Δ) denote experimental runs *r1* and *r2*, respectively (only 1% of data points are shown), and lines denote their average. Initial slide submergence is as listed in Table 1, d = (a) 61, (b) 80, (c) 100, (d) 120, (e) 140, (f) 149, (g) 189 mm (see Figure 6)

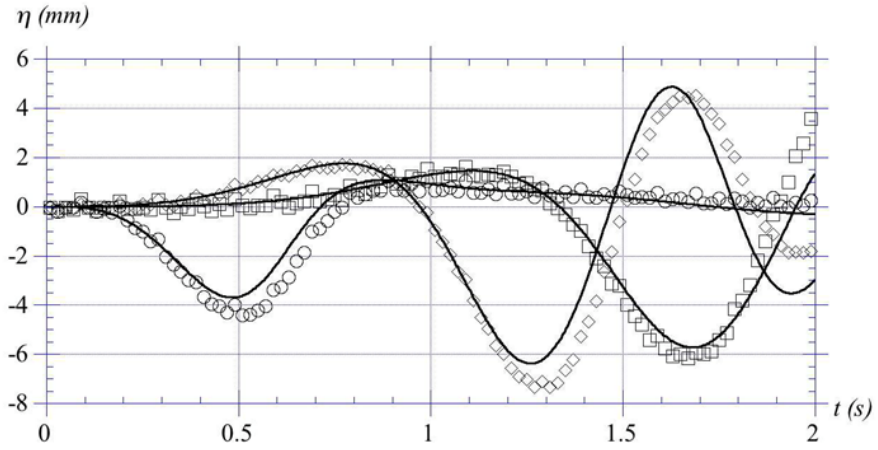

Figure 12: Comparison of FNPF model results (solid line) with 3D submarine slide experiments of *Enet and Grilli* (2007) (symbols) for $d = 0.140$ m, at gauge g1 ($\diamond$) and g2 ($\square$). Only 10% of experimental data points are shown (*Grilli et al.*, 2010).

d (mm)	61	80	100	120	140	149	189
x_g (mm) (measured)	551	617	696	763	846	877	1017
x_g (mm) (theoretical)	560	630	705	780	854	888	1037
η_0 (mm)	13.0	9.2	7.8	5.1	4.4	4.2	3.1
R_u (mm)	6.2	5.7	4.4	3.4	2.3	2.7	2.0
C_m	0.601	0.576	0.627	0.679	0.761	0.601	0.576
C_d	0.473	0.509	0.367	0.332	0.302	0.364	0.353
a_0 (m/s)	1.20	1.21	1.19	1.17	1.14	1.20	1.21
u_t (m/s)	1.70	1.64	1.93	2.03	2.13	1.94	1.97
t_0 (s)	1.42	1.36	1.62	1.74	1.87	1.62	1.63
S_0 (m)	2.408	2.223	3.130	3.522	3.980	3.136	3.207

Table 1: Wave generation by underwater 3D slide. Measured and curve-fitted slide and wave parameters for various slide initial submergence depths (Figure 1)

$g1$	$g2$	$g3$	$g4$
(x_0,0)	(1469, 350)	(1929, 0)	(1929, 500)

Table 2: Wave gauge locations (x, y) in mm, as indicated in Figure 9.

3.3 Benchmark 3: Three-dimensional submarine/subaerial triangular solid block (http://www.udel.edu/kirby/landslide/problems/benchmark_3.html)

This benchmark problem is based on the 3D laboratory experiments of *Wu* (2004) and *Liu et al.* (2005), for a series of triangular blocks of various aspect ratios moving down a plane slope into water from a dry (subaerial) or wet (submarine) location. See Figure 13 for pictures and Figure 14 for a sketch of experiments.

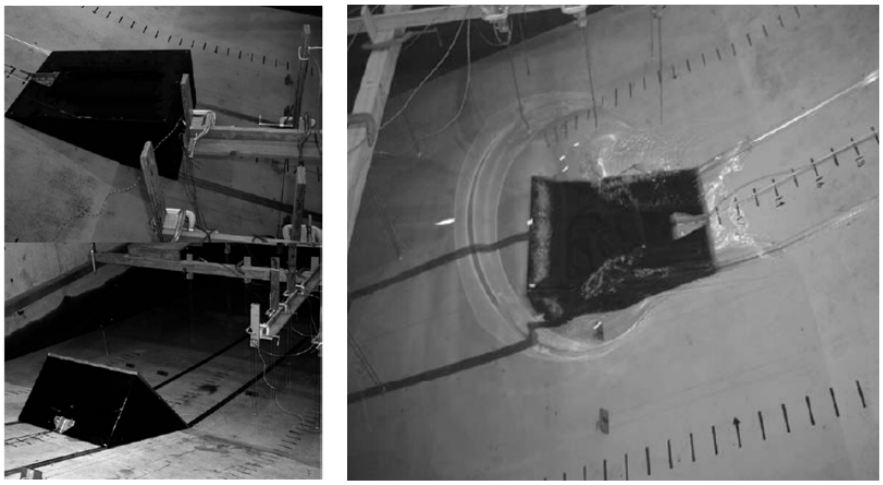

Figure 13: Pictures of experimental set-up for 3D experiments of subaerial slides represented by triangular solid blocks. (*Liu et al.*, 2005).

The experiments were conducted in a wave tank at Oregon State University (OSU), of length 104 m, width 3.7 m and depth 4.6 m. A plane slope 1:2 (Figure 14) with $\theta = 26.6^\circ$ was located near one end of the tank and a dissipating beach at the other end. In all the experiments, the water depth was $h_0 = 2.44$ m. While a few solid block shapes were tested, here, we only consider the experiments performed with a triangular block of length $b = 0.91$ m, width $w = 0.61$ m, (vertical) front face $a = b/2 = 0.455$ m (Figure 13, upper left and right; Figure 14), and mass $M_b = 190.96$ to 475.5 Kg. Hence slide volume is $V_b = 0.126285$ m^3 and density $\rho_b = 1,512$ to $3,765$ $\mathrm{Kg/m}^3$ (note, the specific weight indicated in Liu et al. for the largest mass is, $\gamma = \rho_b/\rho_w = 3.43$, implying a slightly lower maximum density). Upon release, the slide model rolled down the slope on low-friction V-shaped wheels, about 3 mm above the slope, with its motion being recorded. The Coulomb friction coefficient measured in experiments for this block was $C_n = 0.1577$ to 0.2182, depending on block mass (see Table 1 in *Liu et al.* (2005)).

In the experiments, besides slide motion, the free surface elevation was measured at

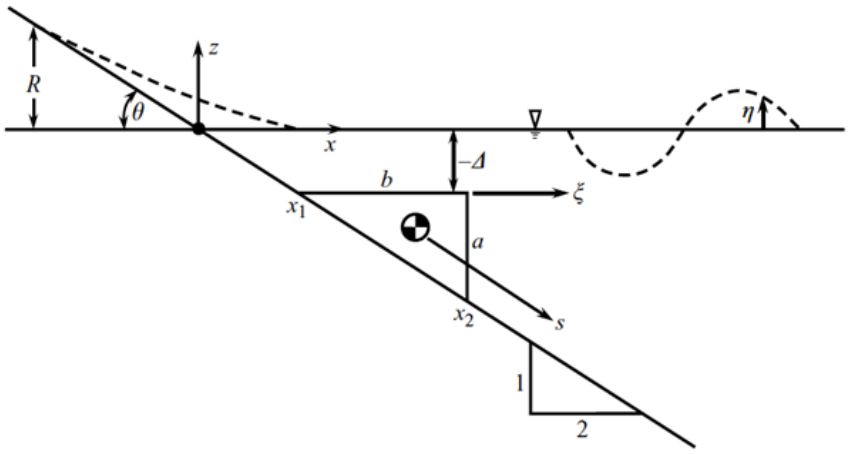

Figure 14: Definition sketch for 3D experiments of submerged/subaerial ($\Delta < / > 0$) slides modeled by triangular solid blocks moving down a plane 1:2 slope. (*Liu et al.*, 2005).

a few wave gauges and the runup/rundown recorded on the slope. Figure 15 shows time histories of free-surface elevations measured at 2 wave gages located at $x/b = 1.20$ and $y/b = 0$ or 0.28 (see legend), for three initial slide submergences Δ/b = -0.155, -0.328, -0.437. For such submarine slides, Liu et al. defined their solid block acceleration a_0 with an equation identical to Eq. (??) for Benchmark 2. For subaerial slides, however, the equation simplified to $a_0 = g \sin\theta(1 - \tan\psi/\tan\theta)$ This equation was used to compute the Coulomb friction coefficients listed in Table 3. Other similar results of experiments reported in Liu et al. are shown in Figures 16 and 17 for $\Delta = 0.454$ m (subaerial) and $\gamma = 3.24$ or 3.43.

Wu (2004) and *Liu et al.* (2005) performed 3D-LES simulations, using the PLIC-VOF method and compared numerical results to their experimental data; some of these results are shown in Figures 16 and 17. They prescribed the slide motion in the model, based on the measured slide displacement; see *Wu* (2004) for information on slide motions and details of numerical simulations. *Abadie et al.* (2010) simulated one of these subaerial slide case for $\Delta = 0.10$ m (subaerial) and $\gamma = 2.14$ (Figure 17). They used a multi-fluid Navier-Stokes (NS) model, in which the solid slide was modeled as a fluid of very large viscosity and thus slide motion was implicitly computed as part of the solution (see *Abadie et al.*, 2010, for results). Like Liu et al.'s simulations, *Abadie et al.*'s results for slide motion and surface elevations at gages ($x/b = 2.001$ and $y/b = 0$ and 0.694 (Figure 18) were in good agreement with experiments, here without forcing slide motion.

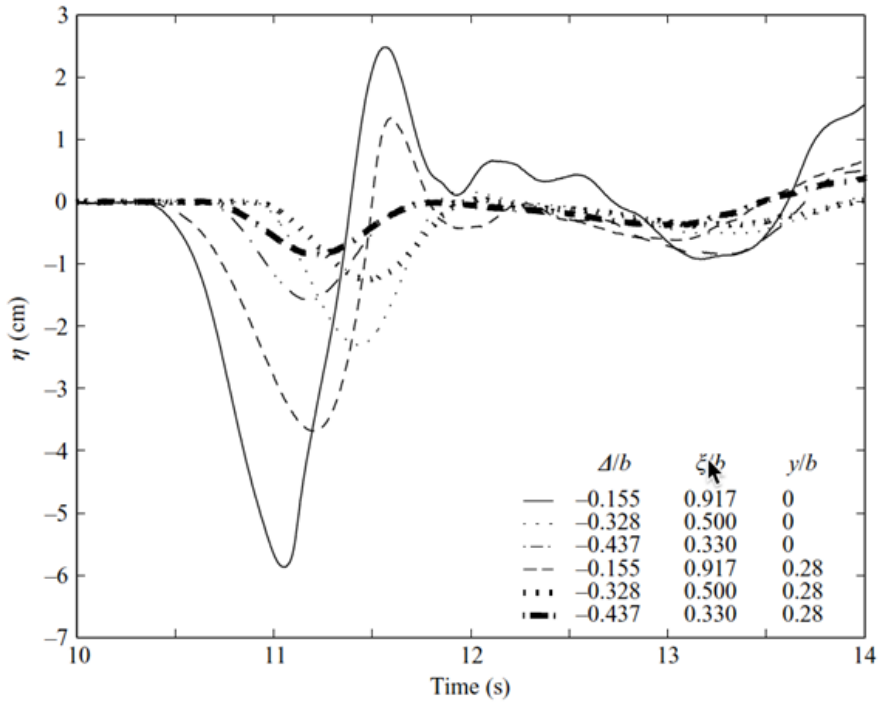

Figure 15: Time histories of free-surface elevations measured at gages located at $x/b = 1.20$ and y/b (legend), for three initial slide submergences Δ/b.(*Liu et al.*, 2005).

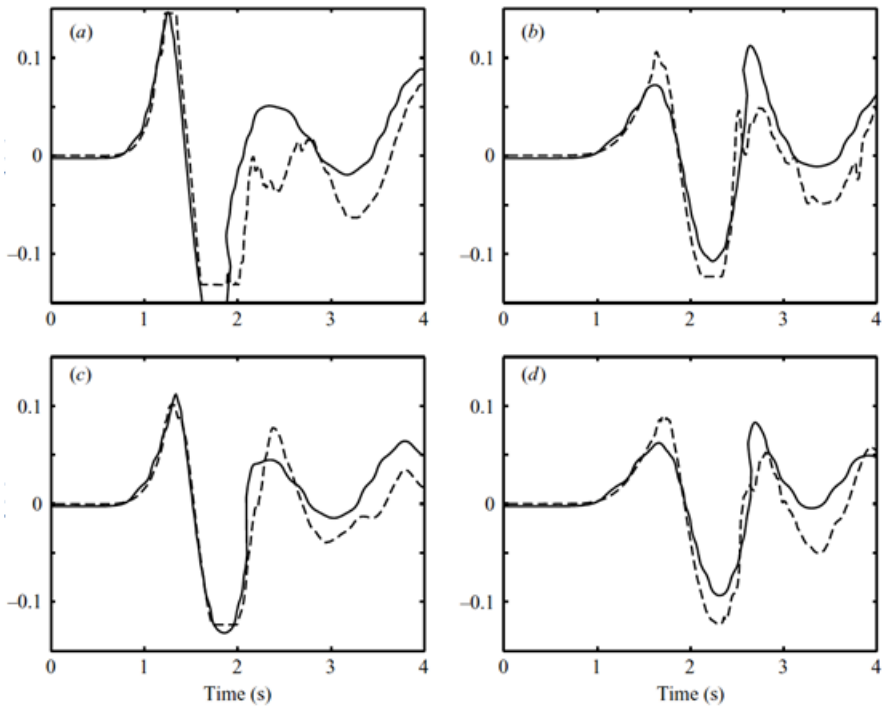

Figure 16: Solid triangular block experiments for $\Delta = 0.454$ m (subaerial) and $\gamma = 3.24$. Computed (-) and measured (- - -) surface elevations at wave gauges located at (x, y) in m: (a) 1.83, 0; (b) 2.74, 0; (c) 1.83, 0.635; (d) 2.74, 0.635. (*Liu et al.*, 2005).

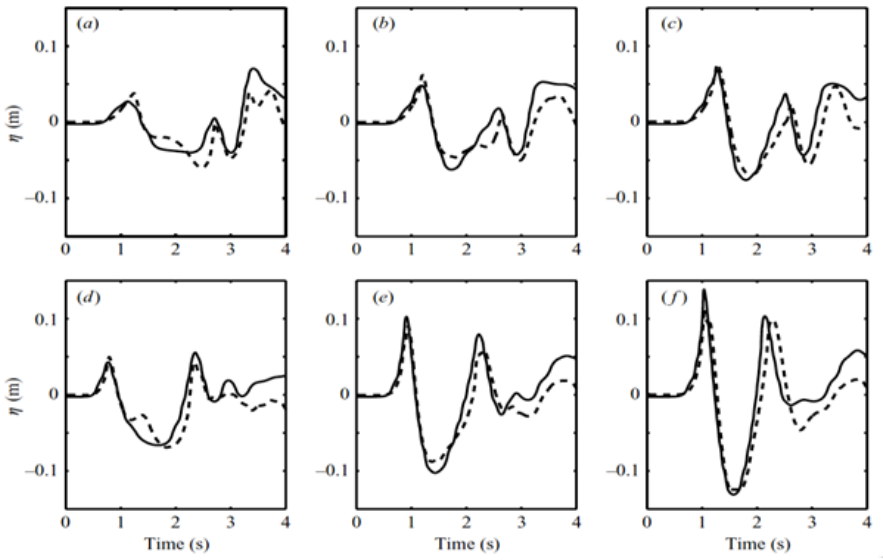

Figure 17: Solid triangular block experiments for $\Delta = 0.454$ m (subaerial) and $\gamma = 3.43$. Computed (-) and measured (- - -) surface elevations at wave gauges located at (x, y) in m: (a) 0.4826, 1.092; (b) 0.8636, 1.092; (c) 1.2446, 1.092; (d) 0.4826, 0.635; (e) 0.8636, 0.635; (f) 1.2446, 0.635 (*Liu et al.*, 2005).

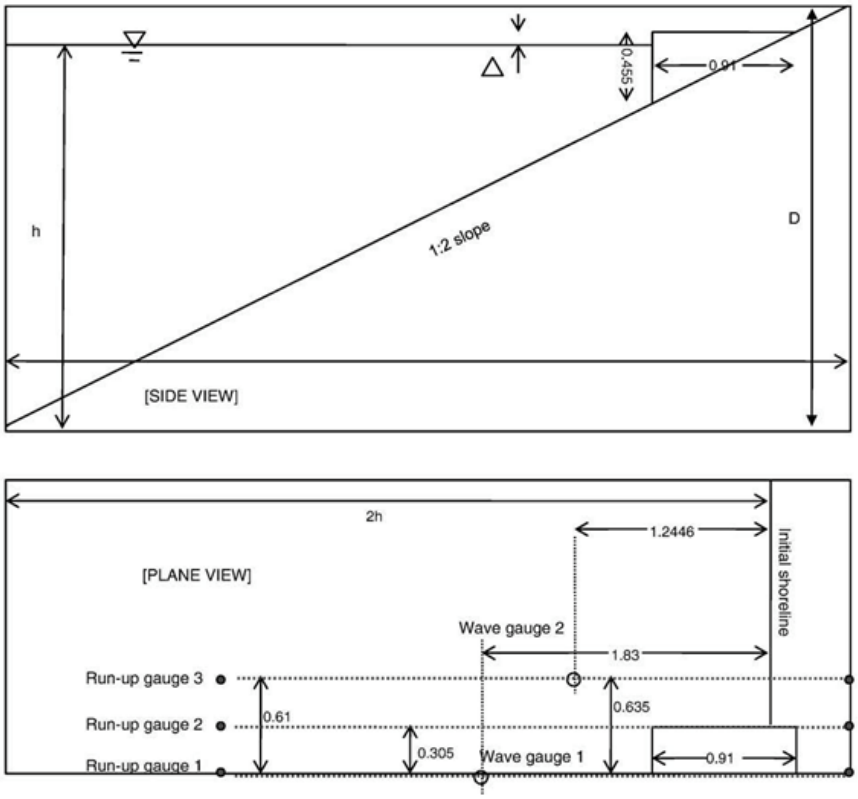

Figure 18: Sketch of numerical simulation by *Abadie et al.* (2010) of one of *Wu* (2004) and *Liu et al.* (2005) solid block experiments, with $\Delta = 0.10$ m (subaerial) and $\gamma = 2.14$.

Δ	a	b	c
0.10 m	–0.097588	0.759361	0.078776
-0.025 m	–0.085808	0.734798	–0.034346

Table 3: Polynomial coefficients defining slide motion.

3.3.1 Provided data

Data is provided in the file *benchmark3/BENCH3.zip* and includes recorded block motion, wave gauge and runup measurements for the two different initial elevations of the wedge on the beach. The recorded block motions were curve-fitted as a function of time t, giving the horizontal distance, $x_{0,t} = x_{0,t=0+(at^3+b^2+ct)} \cos\beta$, where $\beta = \arctan(1/2)$ and $x_{0,t=0} = -2\Delta$. The polynomial coefficients are given in Table 3.

For each case, measured free surface elevations are given for 2 wave gages placed at $(x, y) = (1.83, 0)$ m and $(x, y) = (1.2446, 0.635)$ m, where x is distance to the initial shoreline and y is distance to the central cross-section (Figure 18). Measured runup is given for each case at runup gages 2 and 3 (Figure 18), lying on the slope at distance 0.305m, and 0.61 m from the central cross-section.

Data is given in separate text files, in meter, as time versus elevation (t, η); files are named *benchmark3/benchGG02-X_wave_gage_Y.txt* and *benchmark3/benchGG02-X_runup_gage_Y.txt*, where X is the run number (30 for the first case and 32 for the second case), and Y is the gauge number (1 or 2 for the wave gauges and 2 or 3 for the runup gauges).

3.3.2 Benchmark problem

The benchmark here consists in using the above information for the solid wedge sliding down the 1:2 slope, and details in references, to reproduce the experimental set-up (see Figure 18) and simulate surface elevations measured at the wave gauges and runup/rundown measured on the beach for two initial locations of the block, with $\Delta = 0.1$ m (subaerial); and $\Delta = -0.025$ m (submerged). As a minimum results should be provided for the same experiment as in *Abadie et al.* (2010) with $\Delta = 0.1$ m.

3.4 Benchmark 4: Two-dimensional submarine granular slide (http://www.udel.edu/kirby/landslide/problems/benchmark_4.html)

This benchmark problem is based on 2D laboratory experiments of Kimmoun and Dupont (2015); see *Grilli et al.* (2017) for the main details of the experiment. The experiments were performed in the Ecole Centrale de Marseille's (IRPHE) precision tank (Marseille, France), for a series of triangular submarine cavities filled with glass beads, released by lifting a sluice gate and moving down a plane slope into water. See Figures 19 and 20 for pictures and sketches of the experimental set-up.

Fifty-eight experiments (numbered 13 to 72 in file *benchmark4/Tests_landslide_info.xlsx*) were performed (each with one replicate for the same parameters; hence for 29 independent sets of parameters) in a precision tank filled with fresh water, of useful length $l =$ 6.27 m, width $w = 0.25$ m, of water depth $h = 0.320$ to 0.370 m (Figure 19), glass beads of density $\rho_b = 2{,}500$ kg/m^3, diameter $d_b = 4$ or 10 mm, and with a total dry weight $W_b = 1.5$ to 2.5 kg. Upon release with a sluice gate, beads are moving down a slope $\theta = 35°$. In 20 experiments, a layer of glass beads was glue to the slope. The starting time of experiments $t = 0$ is defined when the gate has just withdrawn into its cavity (Figure 20).

During experiments, the deforming slide shape was recorded with a high-speed video camera (1,000 frames per second; see file *benchmark4/test17_video.mp4*) and time series of surface elevations were measured at 4 wave gages, WG1-WG4 (Figure 39). Figure 20 shows snapshots extracted from the video of test 17, which had parameters: h= 0.330 m; $d_b = 4$ mm, $W_b = 2$ kg, and no glued beads on the slope, up to t = 0.60 sec (note the starting time of each experiments, $t = 0$, is defined when the gate has just withdrawn into its cavity). We see that "onshore" moving waves are generated that cause runup on the slope together with "offshore" moving waves that reflect on the far end of the tank and propagate back towards the generation area. This behavior is also clearly observed in time series measured at wave gages WG1-WG4 (Figure 21). A detailed analysis of experimental results shows experiments are highly repeatable with almost unnoticeable differences between surface elevations for 2 replicates.

Grilli et al. (2017) simulated experiments for test 17, corresponding to the case of Figs. 18 and 19, with both the heavy Newtonian fluid-NHWAVE model of *Kirby et al.* (2016) and the granular slide-NHWAVE model of *Ma et al.* (2015). Figure 41 shows the comparison of free surface elevations simulated with the heavy fluid model, in which an equivalent fluid-like slide density $\rho_s = 1{,}951$ kg/m^3 was used, together with a viscosity $\mu_s =$ 0.01 kg/(m.s) and a Manning friction coefficient $n = 0.005$ contolling friction between the slide and underlying slope. The agreement observed in Figure 41 between simulations and experiments is quite good. The equivalent density results from a weighed average within the triangular cavity of the glass beads and interstitial water density (assuming a random packing); this also led to estimating the submergence depth for this case (not measured, to $d = 0.0422$ m). Regarding viscosity, the selected value was based on earlier work for the estimated viscosity of Newtonian granular flows. Finally, once the viscosity selected,

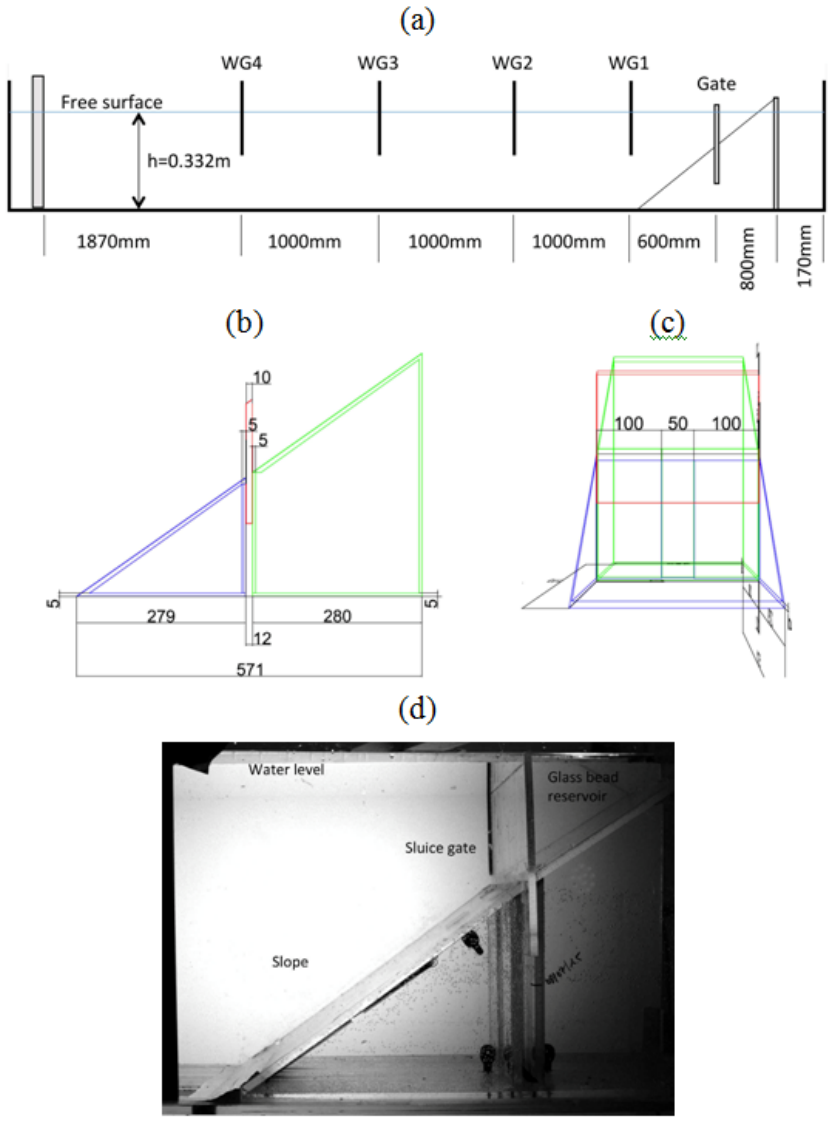

Figure 19: Set-up for laboratory experiments of tsunami generation by underwater slides made of glass beads performed in IRPHE's precision tank with useful length $l = 6.27$ m, width $w = 0.25$ m, and water depth $h = 0.330$ m. Upon release, beads are moving down a $\theta = 35°$ slope. (a) Longitudinal cross section with marked location of sluice gate and 4 wave gages (WG1, WG2, WG3, WG4). (b,c) Zoom-in on side- and cross-section views of slope and sluice gate (dimensions marked in mm). (d) Picture of experimental set-up around slope and sluice gate.

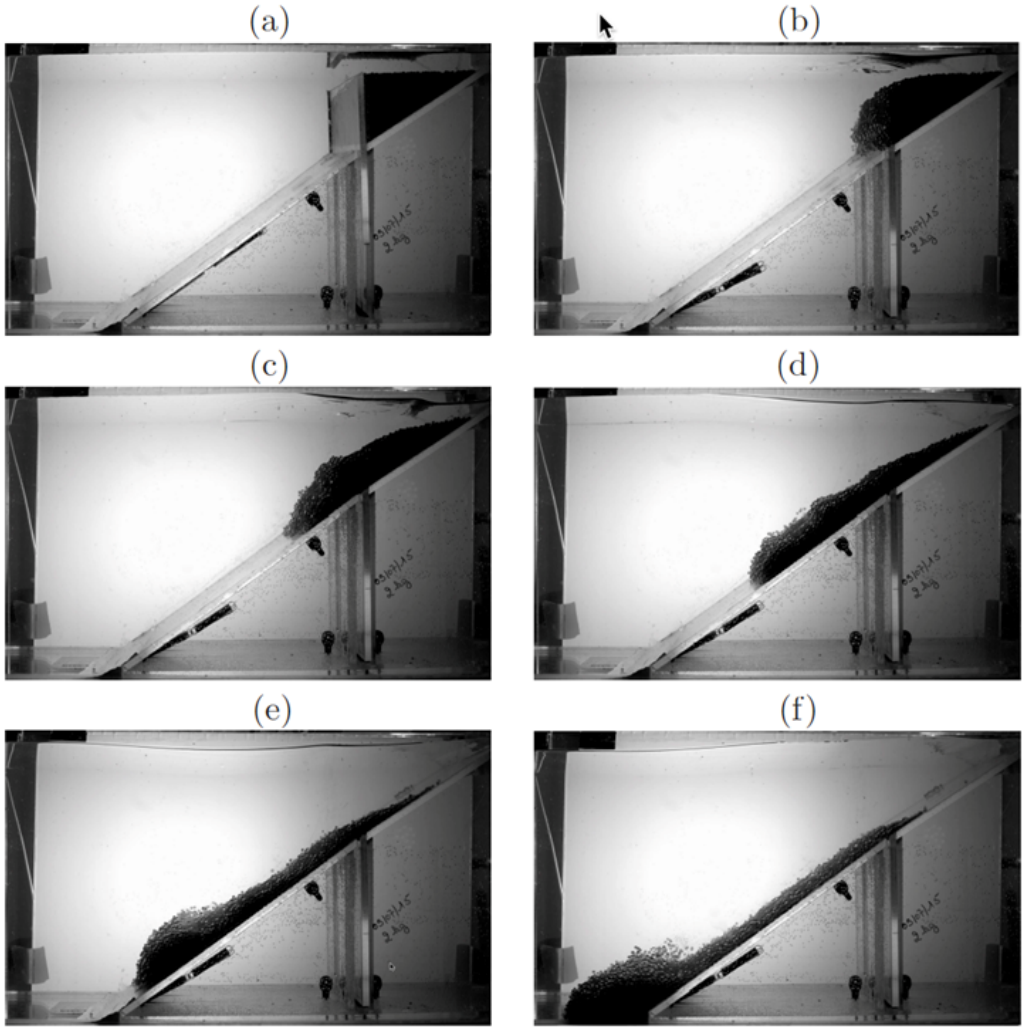

Figure 20: Snapshots of laboratory experiments of tsunami generation by underwater slide made of glass beads, for $h = 0.330$ m; $d_b = 4$ mm, $W_b = 2$ kg, at times $t =$ (a) -0.105; (b) 0.02; (c) 0.17; (d) 0.32; (e) 0.47; and (f) 0.62 s. Note, glass beads are initially stored within the glass bead reservoir with the sluice gate up; at later times, after the gate is withdrawn, the deforming slide moves down the 35° slope while the free surface is deformed. The slope is smooth, with no glued beads. The starting time of experiments $t = 0$ is defined when the gate has just withdrawn into its cavity.

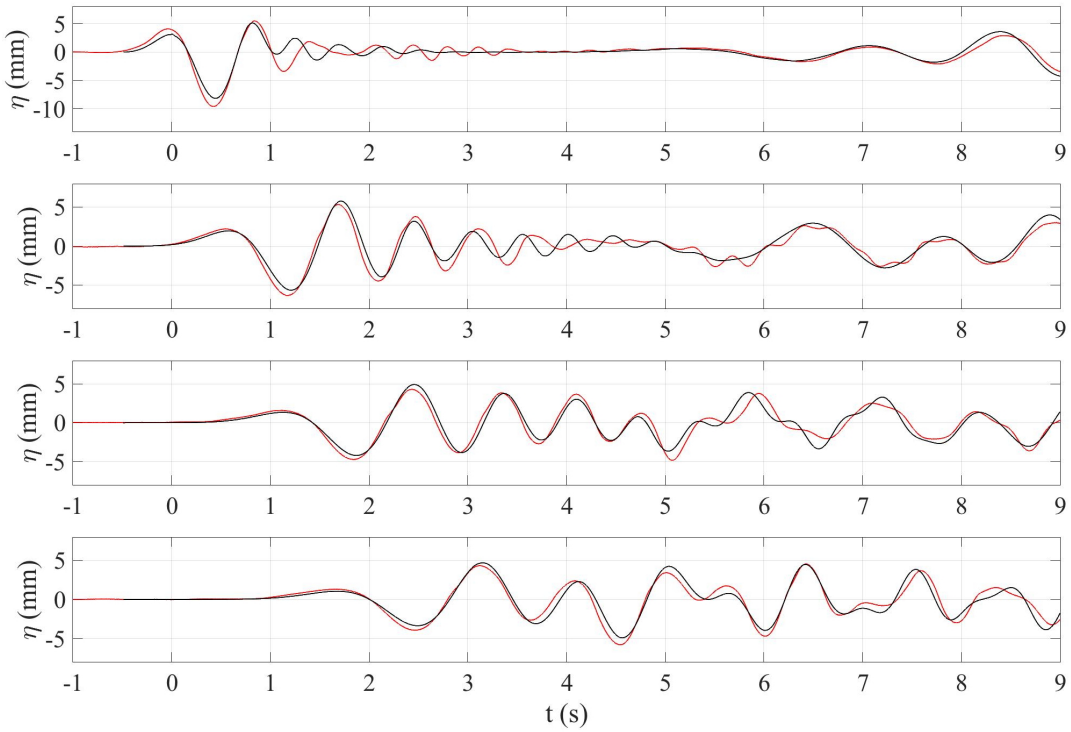

Figure 21: Comparison of observed (blue) time series of surface elevation at wave gages WG1 to WG4 (Fig. 3a), from top to bottom, to those computed (red) by *Grilli et al.* (2017) using the model NHWAVE (*Ma et al.*, 2012), with a dense Newtonian fluid layer underneath (*Kirby et al.*, 2016) with $\rho_s = 1,951$ kg/m^3, $\mu_s = 0.01$ kg/(m.s) and Manning's $n = 0.005$. The origin of the time axis corresponds to the arrival of the first elevation wave at gage WG1.

the Manning n coefficient value was calibrated for the deforming slide to reach the slide bottom in simulations at the same time as in experiments. A good agreement was also observed for the leading two waves, for the simulations with the granular slide model (not shown here), in which the granular medium was directly represented by glass beads.

3.4.1 Benchmark problem

The benchmark here consists in using the above information to simulate as a minimum the glass bead experiment of *test 17* discussed above, and compare the computed surface elevations to those measured at the 4 wave gages WG1-WG4 (as in Figure 41). The measured surface elevations for this test are provided as tab-delimited text file *benchmark4/test17.txt* or comma-separated text file *benchmark4/test17.csv* and the corresponding high speed video is given in file *benchmark4/test17_video.mp4*. The data is given in format (t(s), η_1 (cm), η_2 (cm), η_3 (cm), η_4 (cm)). The entire set of experimental results for the 58 experiments, however, is provided, with parameters for each test given in file *benchmark4/Tests_landslide_info.xlsx* and the surface elevations measured for each test given in file *benchmark4/gages.zip*, together with a Matlab code to extract and plot the data for each test case. This code also calculates the various dimensions of the slide itself, plus necessary parameters for computations.

3.5 Benchmark 5: Two-dimensional subaerial granular slide (http://www.udel.edu/kirby/landslide/problems/benchmark_5.html)

This benchmark problem is based on the 2D laboratory experiments of *Viroulet et al.* (2014) in a small tank at Ecole Centrale de Marseille's (IRPHE; Marseille, France), for a series of triangular subaerial cavities filled with dry glass beads of diameter D and density $\rho_s = 2{,}500$ kg/m^3, released by lifting a sluice gate and moving down a plane 45° slope into water. See Figure 22 for a sketch of the experimental set-up.

The experimental set-up used by *Viroulet et al.* (2014) is shown in Figure 22. It consists of a wave tank, 2.2 m long, 0.4 m high, and 0.2 m wide. A granular slide is initially retained by a vertical gate on the dry slope. At the beginning of the experiment, the gate is suddenly lowered. In the numerical model, it should be assumed that the gate release velocity is large enough to neglect the time it takes the gate to withdraw. The initial slide shape will be assumed to have a triangular cross-section over the width of the tank, with down-tank length L, and front face height $B = L$ as the slope angle is 45°. In all cases, the front face of the granular slide touches the free surface at $t = 0$.

Two test cases are considered in this benchmark, which are referred to as Case 1 and Case 2 in the result files names. The initial conditions for each case are, respectively:

Case 1 : $D = 1.5$ mm, $H = 14.8$ cm, $L = 11$ cm

Case 2 : $D = 10$ mm, $H = 15$ cm, $L = 13.5$ cm

The volume fraction of the granular media for the 2 cases was estimated to be 0.6 and 0.05.

Viroulet et al. (2014) performed numerical simulations where they tested two different fluid rheology, a Newtonian fluid and a Bingham fluid with a density 0.6 times that of the dry beads, $\rho_s = 1{,}500$ kg/m^3. For Case 1, best results were obtained with a viscosity of 5 Pa.s for the Newtonian fluid and with a viscosity of 5 Pa.s and a shear stress of 100 Pa for the Bingham fluid.

3.5.1 Provided data

Experimental results are provided for the measured surface elevations for these 2 tests are provided as text files, either tab delimited (*benchmark5/test_1mm5.txt, benchmark5/test_10mm.txt*) or comma delimited (*benchmark5/test1mm5.csv, benchmark5/test10mm.csv*). The data is given in format (t(s), η_1 (cm), η_2(cm), η_3(cm), η_4(cm)).

3.5.2 Benchmark problem

The benchmark here will consist in simulating the time series of free surface elevations at the 4 wave gages WG1-WG4 for the 2 test cases listed above.

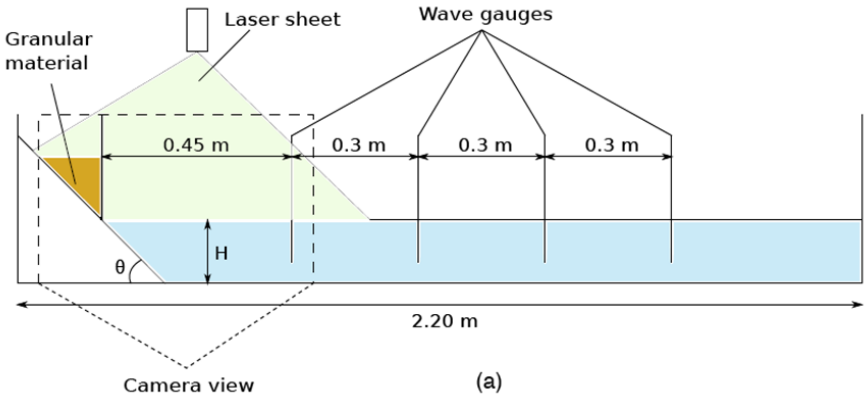

Figure 22: Set-up for laboratory experiments of tsunami generation by subaerial slides made of glass beads performed in IRPHE's precision tank of (useful) length $l = 2.20$ m, width $w = 0.2$ m, and water depth $H = 0.150$ m. Upon release, beads are moving down a slope of $\theta = 45°$. The slide shape and water motion are recorded with high speed video camera and laser PIV, respectively. Surface elevations are recorded at 4 wave gages (WG1, WG2, WG3, WG4) marked on the figure. Picture of measured experimental slides, water elevations, and water velocities are given in Figures 23 - 25.

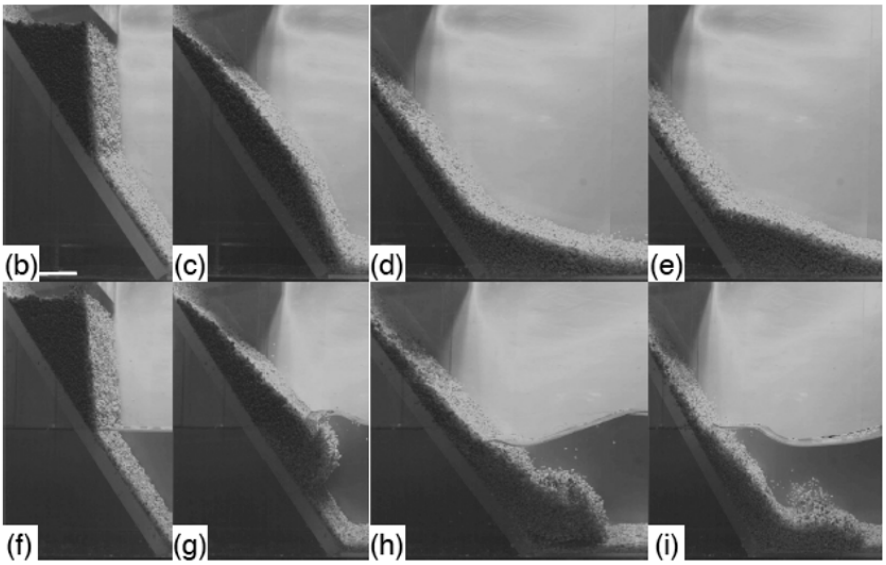

Figure 23: Shape of glass bead slide recorded with a video camera every 0.2 s (white bar in (b) is 5 cm long).

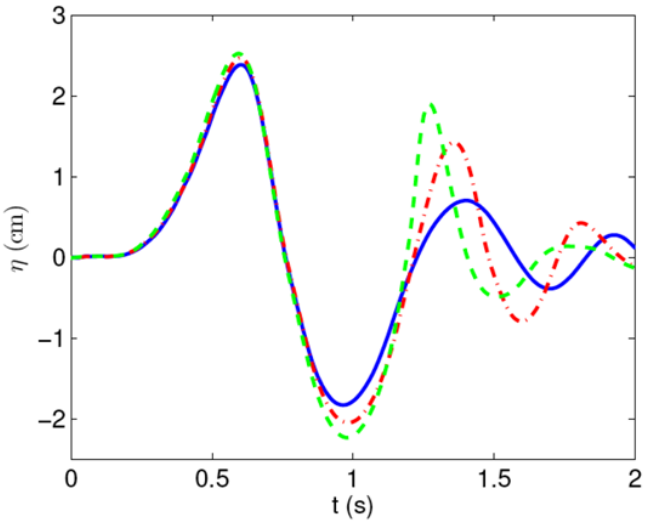

Figure 24: Example of surface elevations measured at wave gages WG1 for 3 different slides.

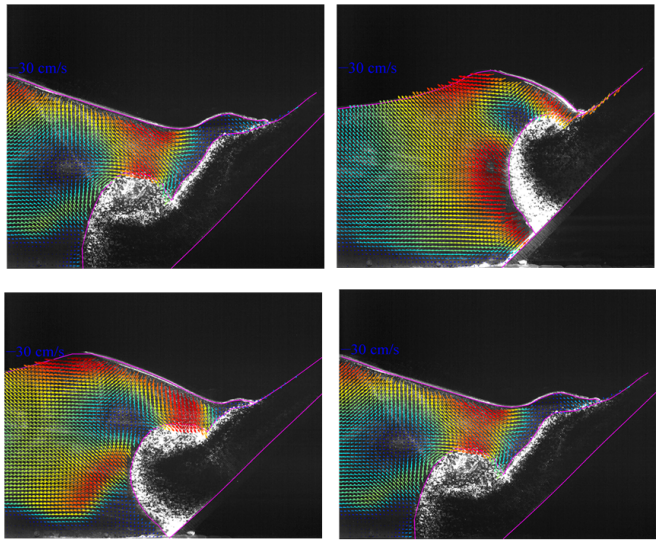

Figure 25: Slide shape, surface elevation and water velocities measured with PIV for one case.

3.6 Benchmark 6: Three-dimensional subaerial granular slide (http://www.udel.edu/kirby/landslide/problems/benchmark_6.html)

Benchmark 6 is for the case of the rapid entry of a narrow slide into an unconstrained, 3D water body, reported by *Mohammed and Fritz* (2012). The landslide tsunami experiments were conducted in the tsunami wave basin at Oregon State University in Corvallis. The landslides are deployed off a plane slope built on one end of the wave basin as shown in Figure 26. The landslide material is deployed in a box measuring 2.1m × 1.2m × 0.3m, with a volume of 0.756 m^3 and weight of approximately 1360 kg.

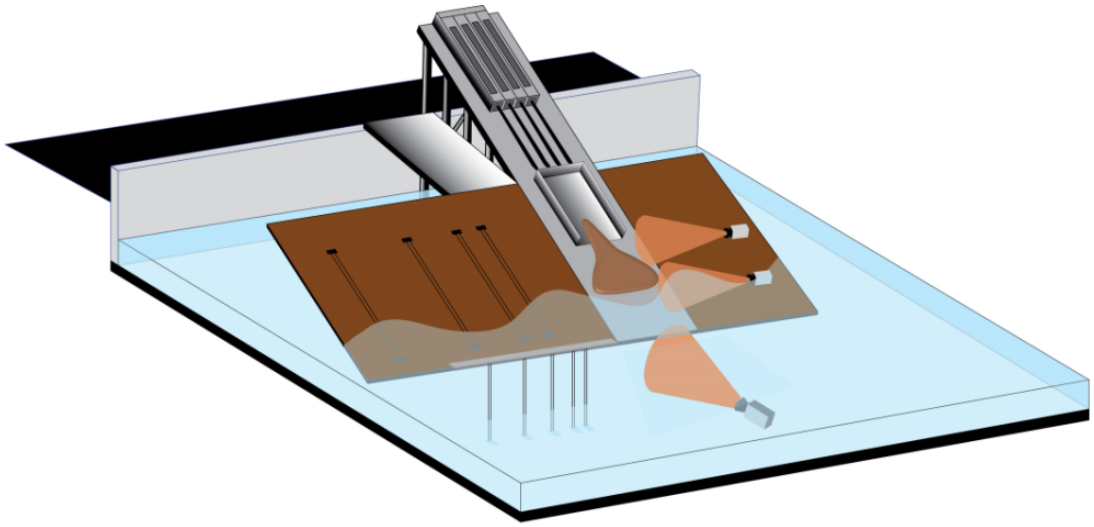

Figure 26: Landslide tsunami generator setup

The plane slope has a slope angle of $\alpha = 27.1^\circ$ corresponding to a slope of 1 vertical to 2 horizontal. Two coordinate systems are defined to characterize the slide motion and wave propagation independently. The slope coordinate system x^s and the wave gauge coordinate system x is shown in Figure 27 for a reference water depth of $h = 0.6$ m. Both the coordinate systems can be unified through the location of the shoreline, which is dependent on the water depth. The toe and the shoreline can be related to each other knowing the slope angle of the hill slope, as shown in Figure 27. Similarly, the shoreline location with reference to the slope coordinate system can be related to the water depth.

The wave gauge locations in the basin are described with reference to the toe of the slope, and are shown in Figure 28. The wave gauges numbered by indices 1-25 in the wave basin are located at (x, y) locations in the tsunami wave basin with reference to the hill slope toe and the wave basin coordinate system as shown in Table 4.

The location of the wave gauges with reference to the shoreline varies with the water depth. Considering the slope planar hill (1:2), the increments shown in Table 5 are added

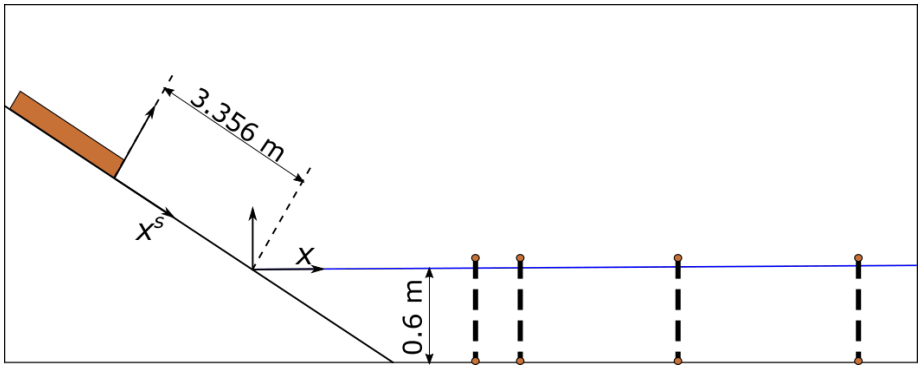

Figure 27: Two coordinate systems x_s and x shown for the slide and wave measurements. The y-direction is considered to be perpendicular outside the image.

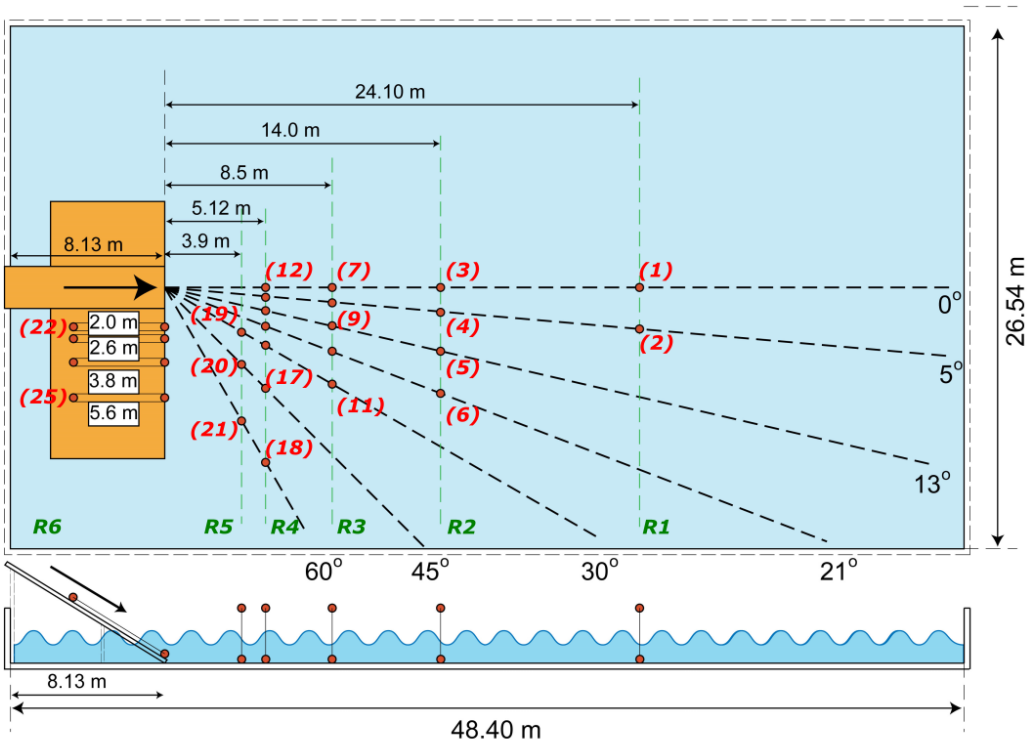

Figure 28: Wave gauge location in the wave basin relative to the wave basin.

$WG\#$	x (m)	y (m)
1	24.1	0
2	24.1	2.108
3	14.0	0.0
4	14.0	1.225
5	14.0	3.232
6	14.0	5.374
7	8.5	0.0
8	8.5	0.744
9	8.5	1.962
10	8.5	3.236
11	8.5	4.907
12	5.12	0.0
13	5.12	0.448
14	5.12	1.182
15	5.12	1.965
16	5.12	2.956
17	5.12	5.12
18	5.12	8.868
19	3.9	2.252
20	3.9	3.9
21	3.9	6.755
	Runup Wave Gauges	
22	0	2.0
23	0	2.6
24	0	3.8
25	0	5.6

Table 4: Wave gauge location with reference to the toe.

h (m)	x (m)
0.3	0.6
0.6	1.2
1.2	2.4

Table 5: Increment added to the wave gauge map for appropriate water depth.

	h(cm)	x^s(m)	t_0
P145	30	2.663	0.44
	60	3.356	0.37
	120	2.014	0.3
P116	30	2.663	0.47
	60	3.356	0.39
	120	2.014	0.33
P087	30	2.663	0.49
	60	3.356	0.4
	120	2.014	0.37
P058	30	2.663	0.52
	60	3.356	0.44
	120	2.014	0.4

Table 6: 3D granular slide: Experimental cases

to the x coordinate system to account for the water depths.

A total of twelve experimental trials were provided for possible benchmark testing. Test cases are labeled according to pneumatic piston pressure P and water depth h in centimeters. Test pressures included $P = X$ psi with X=145,116,87 and 58. For each water depth and P combination, the location of the slide impact with the shoreline in the slope coordinate system changes. The corresponding shoreline location in the slope coordinate system at impact for all the cases is shown in Table 6. The corresponding slide front velocity can be extracted from the data on slide front velocity as a function of distance x_s as shown in Figure 29. The time of impact of the slide front with the shoreline is also shown in Table 3. Since the time coordinate of the wave gauges are initialized to the slide motion initiation, the t_0 time allows to fix the moment of slide impact with the water body.

3.6.1 Summary of coordinate systems

Wave gauges

Spatial: Distances of the wave gauges are with reference to the toe of the hill slope. Incremental distances, ΔX shown in Table 2, are added to the X coordinate system for the appropriate water depth to obtain the wave gauge locations with reference to the shoreline.

Temporal: The time coordinate in the wave gauge history is with the reference to the initiation of the slide motion. In order to adjust the time coordinate to the moment of slide impact, the time of impact is specified in Table 3.

Slide velocity, slide thickness and slide width

Spatial: The slide velocity, thickness and slide width are with reference to the slope coordinate system. In this system, the origin is at the initial location of the slide box along the slide center. The location of impact with the shoreline changes based on the slide location, motion and case as shown in Table 3.

Temporal: The time history of the slide thickness is with reference to the moment of impact of the slide front with the shoreline location. $t = 0$ corresponds to the moment of the slide impact with the shoreline.

Slide deposit

Spatial: The slide deposit data is with reference to the slope toe and the wave basin bottom. The location $x = 0$ corresponds to the location of the toe while $z = 0$ corresponds to the bottom of the wave basin and the hill slope. Slide deposit information is not available for a water depth o$h = 0.3$ m.

3.6.2 Data files

Data files are collected in a zip file
http://www.udel.edu/kirby/landslide/problems/benchmark_6.html/LTG_Experiment_Data.zip.
Descriptions of individual files follows.

Wave gauges

File Name: wg_h_30.mat, wg_h_60.mat, wg_h_120.mat

File Description: Time history of water surface elevation at an array of wave gauges in the wave basin.

File Variables: wg

Variable Description: The wave gauge data is in units of cm. The wave gauge data are with reference to the wave basin [spatial] and slide initiation [temporal]. Wave gauges 22-25 are measured along the slope since the wave gauges are inclined along the slope.

Variable Dimension: $n_p \times n_t \times n_w$

Dimension Values:

n_p	number of LTG cases corresponding to the 4 P cases shown in Table 3	4
n_t	Time Array with $dt = 200$hz	5000
$n_w b$	Wave gauge numbers as shown in Figure 28	25

The (x, y) locations of the wave gauges relative to the toe of the slope in the wave basin are shown in Table 4. The actual distances x of the wave gauges from the shoreline can be calculated based on the water depth and hence the shoreline location from the toe. For example, for a water depth of 60 cm, the shoreline is located at 1.2 m from the toe. Hence, adding 1.2 m to x in Table 4 gives the actual locations of the offshore wave gauges.

Slide velocity

File Name: slide_velocity.mat

File Description: Evolution of slide front velocity with slide front location along the slope in the slope coordinate system.

File Variables: $v58$, $v58\_h$, $v87$, $v87\_h$, $v116$, $v116\_h$, $v145$, $v145\_h$

Variable Description: The velocity data is presented as slide velocity (m/s) versus the slide front (m). The slide velocity is presented in the slope following coordinate system. There is no time reference here. The velocity of the LTG slide box and the released granular landslide is included in this data.

Variable Dimension: $n \times n_x$

Dimension Values:

n	Rows indicate 1: slide front location 2: slide front velocity	2
n_x	number of points in the evolution data	variable

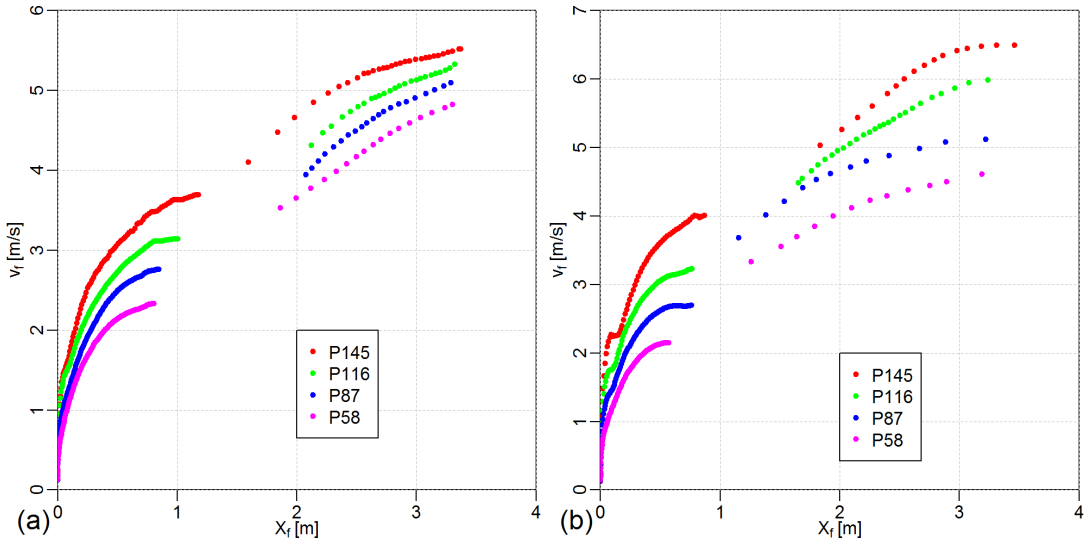

Figure 29: Slide front velocity along the slope with the slide front location.

$vXXX$ contains the slide front velocity along the slide front location for the case corresponding to $XXX = P145, P116, P87, P58$. $vXXX$ contains the velocity information corresponding to slide volume of 0.756 m^3. $vXXX\_h$ contains the velocity information corresponding to slide volume of 0.378 m^3. The information in the variables $vXXX$ and $vXXX\_h$ is shown in Figure 29.

Slide Thickness

File Name: Slide_Thick_F.mat

File Description: Maximum slide thickness along the slide center along the slide propagation on the slope for slide volume of 0.756 m^3.

File Variables: $XFM\_P145, YFM\_P145, XFM\_P116, YFM\_P116, XFM\_P87, YFM\_P87, XFM\_P58, YFM\_P58$

Variables Description: X represents the location on the slope [m] and Y represents the maximum slide thickness at the X location (m). The X is in the slope coordinate system. There is no time reference.

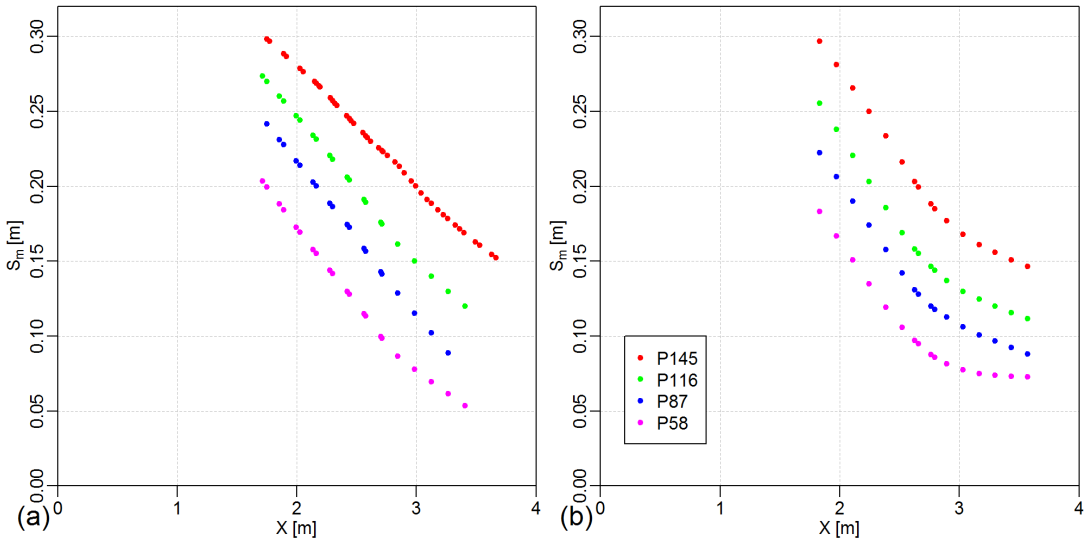

Figure 30: Maximum slide thickness along the slide slope location for slide volumes of 0.786m^3 and 0.378 m^3.

File Name: Slide_Thick_h.mat

File Description: Maximum slide thickness along the slide center along the slide propagation on the slope for slide volume of 0.378m^3.

File Variables: $XHM\_P145, YHM\_P145, XHM\_P116, YHM\_P116, XHM\_P87, YHM\_P87, XHM\_P58, YHM\_P58$

Variables Description: X represents the location on the slope (m) and Y represents the maximum slide thickness (m) at the X location. The X is in the slope coordinate system. There is no time reference.

The maximum slide thickness along the slope in the slope following coordinate is shown in Figure 30.

File Name: hick_PX_FM.mat [4 files with varying values of X]

File Description: Time history of slide thickness along the slide center for the 4 cases

corresponding to $X = P145, P116, P87, P58$ for slide volume of 0.786 m^3.
File Variables: x, t, S

Variables Description:

x : slide propagation along the slope (m)
t : time of measurement adjusted to time of impact (t=0) (s)
S : slide thickness with dimensions $n_x \times n_t$ (i.e length of x times length of t) (m)

The x coordinate is in the slope coordinate system. The time is with reference to the moment of impact ($t = 0$ is the moment of slide impact with the shoreline)

File Name: Thick_PX_HM.mat [4 files with varying values of X]

File Description: Time history of slide thickness along the slide center for the 4 cases corresponding to $X = P145, P116, P87, P58$ for slide volume of 0.378 m^3.

File Variables: x, t, S

Variables Description:

x : slide propagation along the slope (m)
t : time of measurement adjusted to time of impact ($t = 0$) (s)
S : slide thickness with dimensions $n_x \times n_t$ (i.e length of x times length of t) (m)

The x coordinate is in the slope coordinate system. The time is with reference to the moment of impact ($t = 0$ is the moment of slide impact with the shoreline)

Slide Width

File Name: Slide_Width.mat [1 file]

File Description: Edge of maximum slide spread along the slope in the lateral direction. The maximum spread is the same for all the P cases and volumes.

File Variables: X, Y

Variables Description:

X : slide propagation along the slope in slope coordinate system (m)
Y : Lateral extent of the slide on the slope (m)

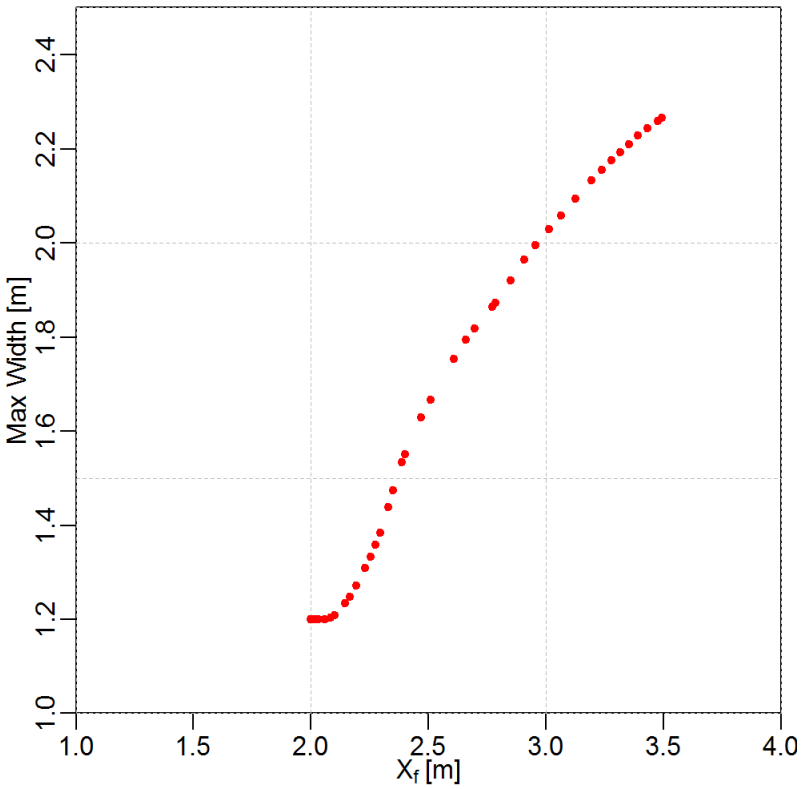

Figure 31: Extent of the maximum slide width on the slope in the lateral direction

The slide motion is with reference to the slope coordinate system [spatial]. The slide width is shown in Figure 31.

Underwater Slide Deposit

File Name: Deps_PX_h60_FM.mat [4 files with varying values of X]

File Description: Measured underwater slide deposit for the 4 cases corresponding to $X = P145, P116, P87, P58$ for slide volume of 0.786 m^3 at a water depth of 0.6 m

File Variables: X, Y, Z

Variables Description:
X : horizontal coordinate with reference to the toe [0 value is the toe of the slope] (m)
Y : lateral coordinate along the slope [0 value is the center of the slide] (m)
Z : two-dimensional array with values of the slide deposits above the basin and slope bottom (m)

The data is with reference to the toe of the slope. There is no temporal reference.

File Name: Deps_PX_h120_FM.mat [4 files with varying values of X]

File Description: Measured underwater slide deposit for the 4 cases corresponding to $X = P145, P116, P87, P58$ for slide volume of 0.786 m^3 at a water depth of 1.2 m.

File Variables: X, Y, Z

Variables Description:

X : horizontal coordinate with reference to the toe [0 value is the toe of the slope] (m)
Y : lateral coordinate along the slope [0 value is the center of the slide] (m)
Z : two-dimensional array with values of the slide deposits above the basin and slope bottom (m)

The data is with reference to the toe of the slope. There is no temporal reference.

3.7 Benchmark 7: Slide at Port Valdez, AK during 1964 Alaska Earthquake (http://www.udel.edu/kirby/landslide/problems/benchmark_7.html)

This benchmark problem is based on the historical event which occurred at Port Valdez, AK during the Alaska Earthquake of March 27, 1964, see Figure 32. The event has recently been studied by *Nicolsky et al.* (2013) and *Parsons et al.* (2014). The first document provides an overview of the historical background and geology for the site, and is the principal source for the problem described below. Other background documents include *Coulter and Migliaccio* (1966), *Plafker et al.* (1969) and *Wilson and Torum* (1972).

3.7.1 Landslide at the head of the bay

The great disaster during the M_w9.2 Alaska Earthquake happened in the dock and harbor area, where a massive submarine landslide generated a tsunami, inundating the waterfront up to two blocks inland. The pre- and post-earthquake bathymetry profiles near the site are shown in *Coulter and Migliaccio* (1966). To the south of Valdez, depth changes exceeding 90 m occurred, which exceeds the depth change off Valdez itself. Thus the major part of the slide took place off the Lowe River delta. It is estimated that approximately 75 million m^3 of unconsolidated deposits were transferred from the waterfront into the bay (*Coulter and Migliaccio*, 1966). A sequence of the waves following the landslide are reconstructed from eyewitness reports and observations. There are inherent uncertainties in the following estimates of wave time arrivals and wave heights.

The following account of the earthquake is taken from *Wilson and Torum* (1972) unless otherwise noted. On the evening on March 27, 1964, the 10,815-ton M/V *Chena* was unloading freight at the Valdez dock (Position a in Figure 33). The ship initially went astern (Position b) with the water withdrawal that accompanied the initial subsidence of the docks and then the *Chena* heeled to port and rose by 6-9 m on an incoming wave and bottomed at the previous location of the docks (Position c). She then came upright, took another roll to the port and was carried to the small boat harbor (Positions d-e). The *Chena* was momentarily aground with her stern in the wreckage of pilings. Consequently, the *Chena* took a violent roll to the starboard before the boat harbor began to fill with water pouring from the shore. A flux of water from the south filled the boat harbor and carried boats and buildings, dislodged by the first wave, toward the Valdez Hotel. It also lifted the *Chena* and enabled her to float free (Positions e-f). The water began to drain from the boat harbor and the ship came under the influence of a strong southerly current, which carried her close alongshore as in a jet stream (Position f). As the *Chena* was moving south, water was seen cascading over the slide scarp.

The extent of inundation by waves which lifted the *Chena* is hard to constrain:

- Some eyewitnesses, in attempt to reach higher ground, drove up Alaska Avenue (Figure 35) to the corner of McKinley Street, but a large volume of water flowing

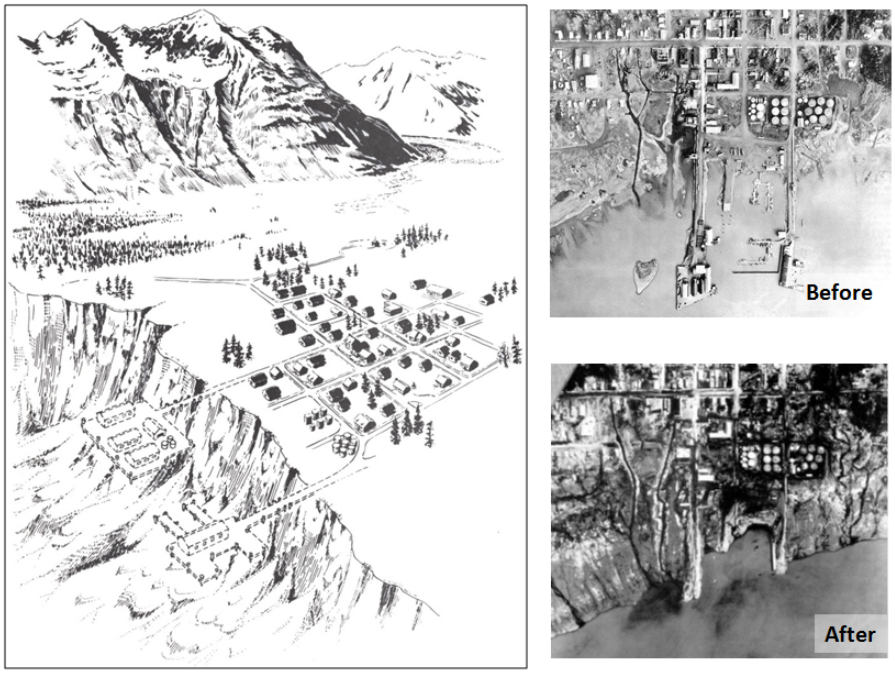

Figure 32: Submerged slide area at Valdez. Dashed lines indicate dock area destroyed in earthquake. Sketch by David Laneville (*Coulter and Migliaccio*, 1966, from).

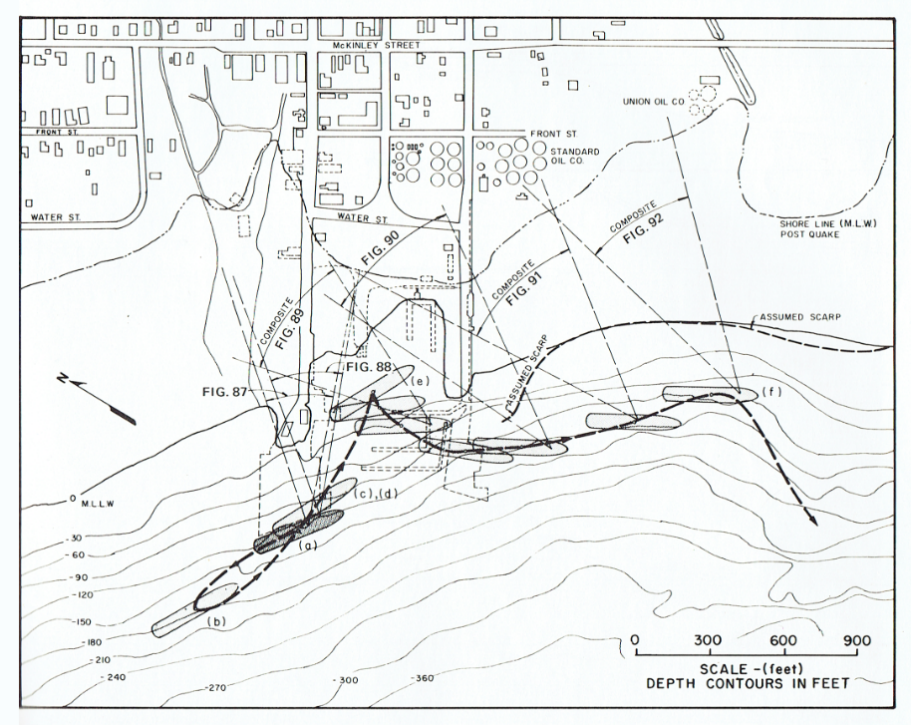

Figure 33: Inferred path of the *Chena* from its initial position at the dock during the earthquake.

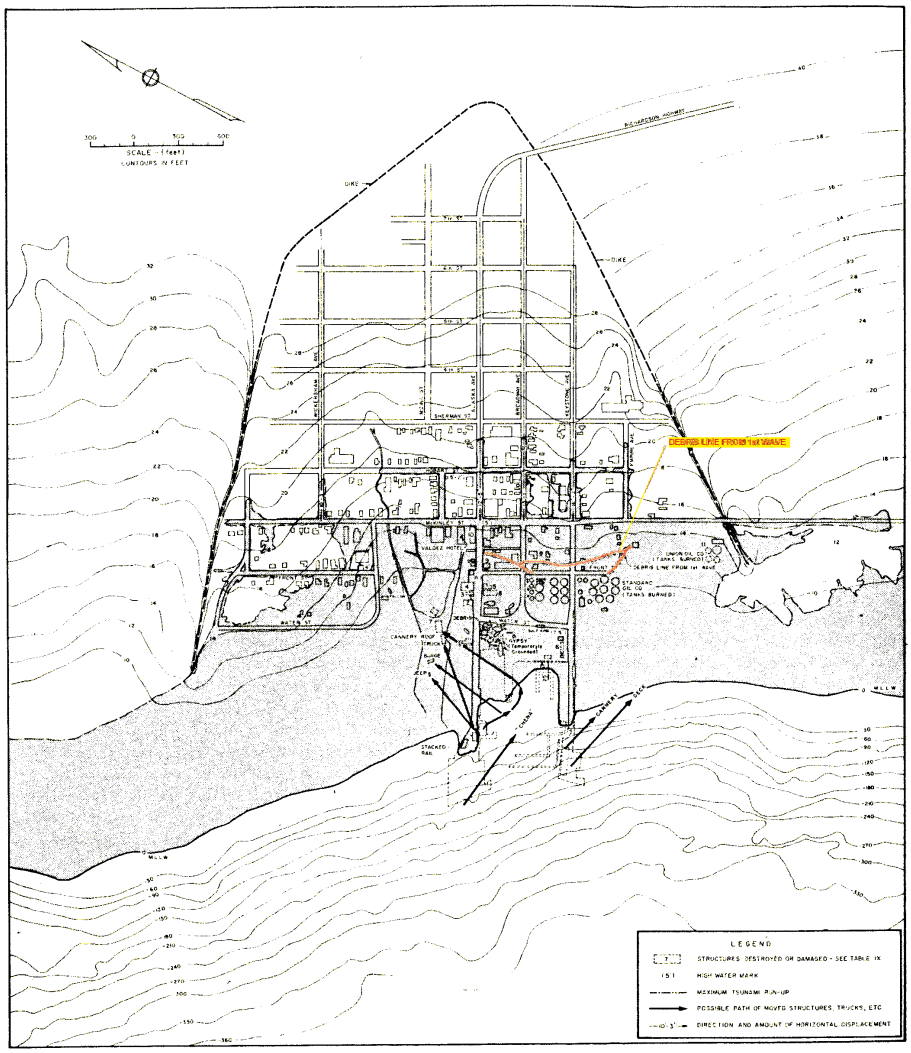

Figure 34: Plan of the old town after the 1964 earthquake, showing the 1964 tsunami inundation (landslide-generated and tectonic) and post-earthquake bathymetry profiles in the MLLW datum (*Wilson and Torum*, 1972). The debris from the first wave is shown by the red line.

down Alaska Avenue made it impossible to proceed further. They turned right and went to the vicinity of the Standard Oil Company plant. From the vicinity of the Standard Oil Company plant, they turned up Broadway Avenue and proceeded on foot in 0.45 m deep water.

- Another eyewitness reported that a wave washed onto the main street (McKinley) on the northeast side of town within 5 minutes after the first shock, and reached two blocks inland.

It is thus reasonable to assume that at least two waves flooded the Valdez waterfront and destroyed what was left within two blocks of shore. The runup reached beyond McKinley Street, or about 300 m from the pre-earthquake shoreline at several points.

The second wave crossed the waterfront 10-15 minutes after the first wave, carrying a large amount of the debris. It has been described as a violent surging wave only slightly smaller than the first. Water from the second wave reached a depth of 0.46 m in the Valdez Hotel on McKinley Street (*Wilson and Torum*, 1972). Location of the hotel is shown in Figure 35 by the red triangle. It is believed that the second wave which flooded the waterfront originated at the other side of the Port Valdez near the Shoup Bay moraine.

3.7.2 Landslide at the Shoup Bay moraine

There were no eyewitnesses to waves that struck the shore at other locations along Port Valdez. However, the inundation line was evident from scattered debris and marks on fresh snow. Figure 36 shows the observed runup around Port Valdez. The highest location obliterated by waves was near the large, abandoned Cliff Mine. According to *Plafker et al.* (1969), the waves deposited driftwood at points 52 m (170 ft) above sea level and splashed silt and sand up to an elevation of 67 m (220 ft). Directly across from the Cliff Mine in Anderson Bay at the south shore of Port Valdez, the waves ran up to 24 m (78 ft) above the water level and destroyed a small fishing camp. All structures of the camp were swept away, leaving only the driven piling foundations. Its sole inhabitant, Harry Henderson, was missing and presumably drowned in the violent local waves that struck Anderson Bay. ¡p¿

The abandoned Dayville cannery at Jackson Point, 8 km (5 mi) east of Anderson Bay, was also extensively damaged by waves that reached as high as 9.5 m (31 ft). Elsewhere along the shore, violent waves broke spruce trees with a diameter of 0.6 m (2 ft) at elevations as high as 31 m (101 ft) and deposited barnacle-covered boulders estimated to weigh 760 kg (1,700 lb) at points 27 m (88 ft) above the shoreline. The waves that moved westward from Port Valdez overtopped and destroyed the Valdez Narrows navigation light (shown in Figure 36 by the red triangle) situated on top of a reinforced concrete pedestal 11 m (36 ft) above the lower low water level.

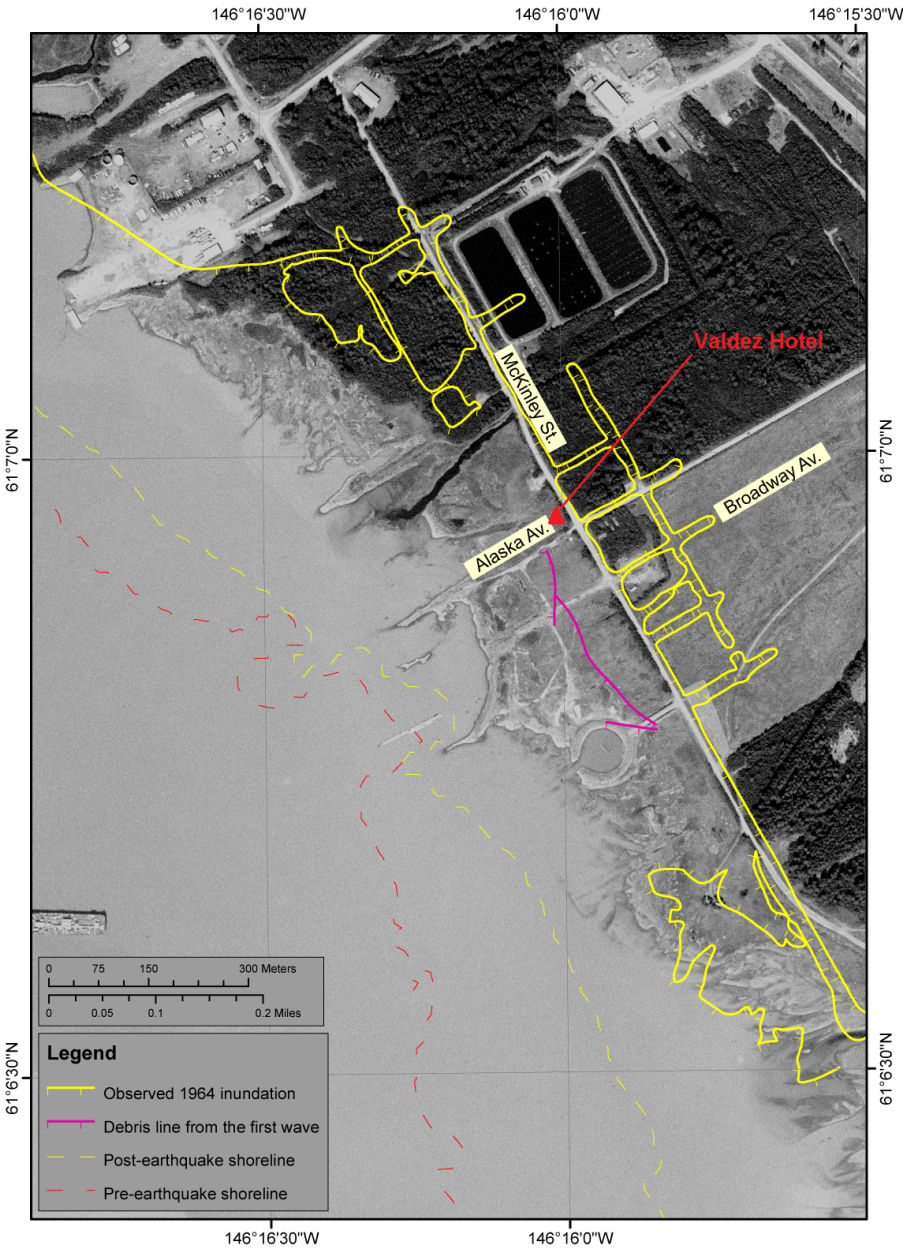

Figure 35: The yellow line represents observed inundation in 1964 caused by both the landslide- and tectonically-generated tsunamis. Hachures indicate the water side of the inundation lines.

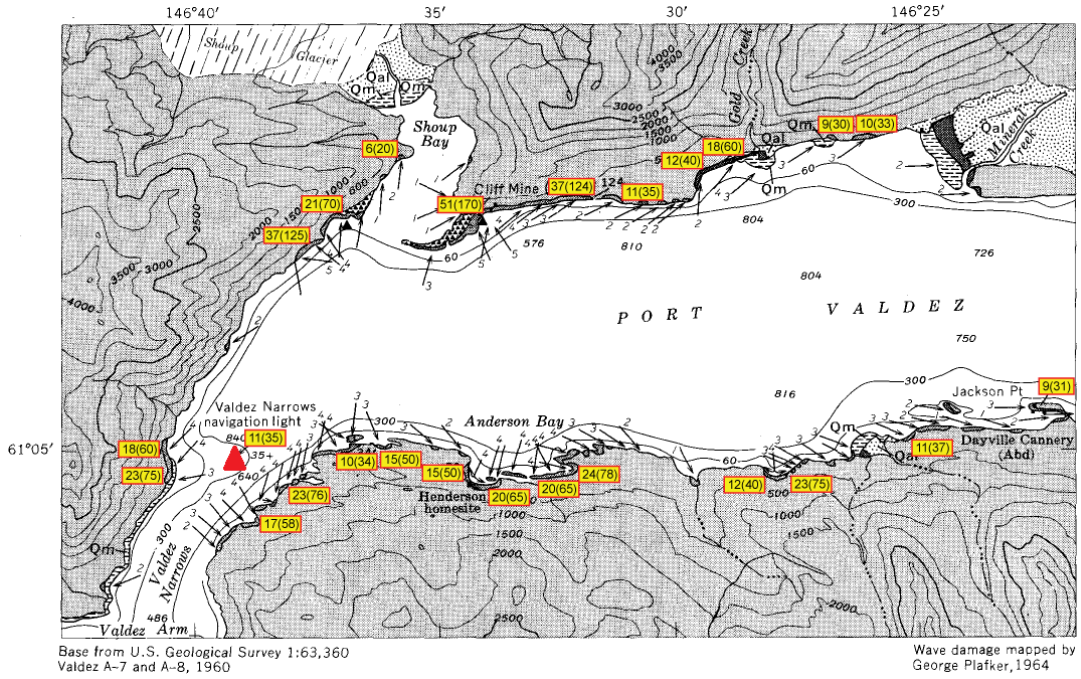

Figure 36: Distribution and intensity of wave damage in Port Valdez after the 1964 earthquake, mapped by L. Mayo and G. Plafker. Inferred direction of the wave arrival is shown by arrows. Relative magnitude of damage is indicated by a numeral at the base of an arrow, based on the scale: 1-runup about 1-2 m (0-6 ft); 2-runup 8 m (25 ft) on steep shores; 3-maximum runup 17 m (55 ft); 4-maximum runup 21 m (70 ft); 5-maximum runup 52 m (170 ft). Yellow boxed numerals onshore next to shaded areas at edge of water provide runup height in meters (and feet) above sea level at time of the earthquake. The base map and description of the damage are from *Plafker et al.* (1969).

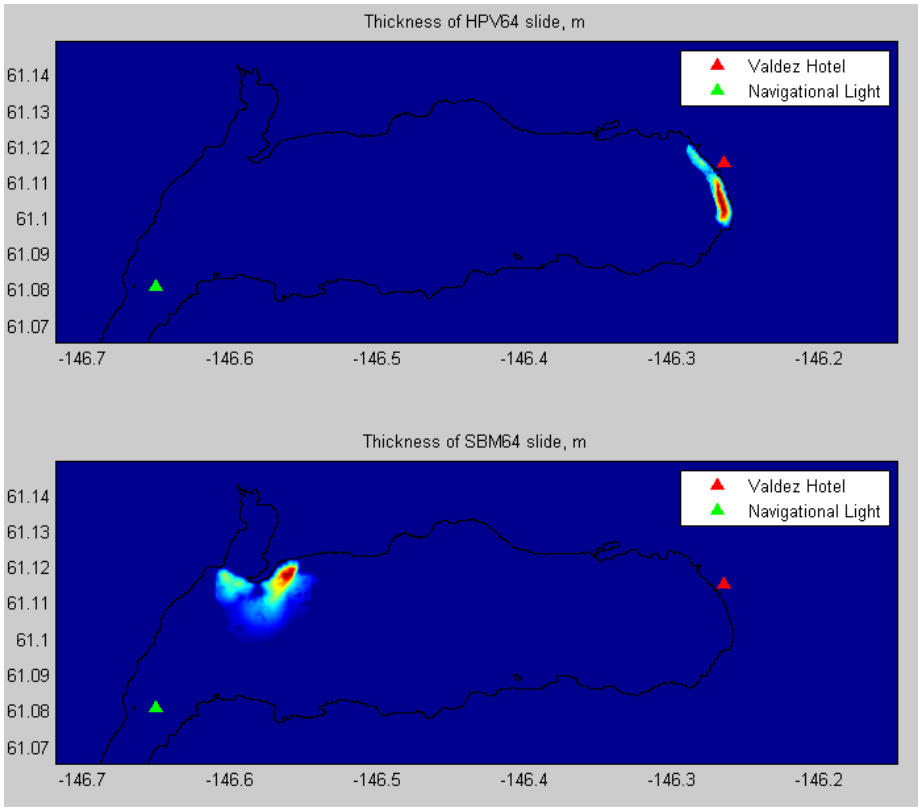

Figure 37: Top: The reconstructed initial thickness of the old town (HPV64) slide during the 1964 earthquake. Bottom: The reconstructed initial thickness of the Shoup Bay (SBM64) slide during the 1964 earthquake.

3.7.3 Provided data

The post-earthquake bathymetry together with the slide thicknesses, shown in Figure 37, can be downloaded as a single zip file *benchmark7/benchmark_7_data.zip*. The archive also contains shape files delineating an extent of the observed inundation at the head of Port Valdez and location of the debris from the first wave. The Matlab script *benchmark7/readData.m* reads all available data and plots contours of the slide thicknesses (Figure 37) as well as the extent of inundation near the head of Port Valdez (Figure 38).

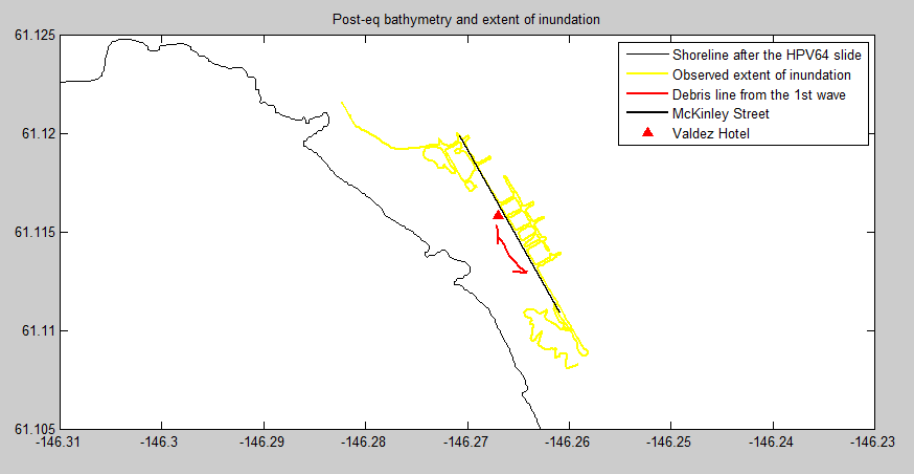

Figure 38: Digitized extent of inundation, location of the debris and location of McKinley Street.

3.7.4 Benchmark problem

The benchmark here will consist in simulating the extent of inundation for two slide events (at the head of the bay and at the Shoup Bay moraine), based on before and after bathymetry data, eye-witness observations of the event, and observed runup distribution.

For the slide at the head of Port Valdez (HPV64), it was recommended to

1. reproduce two waves that struck the Valdez waterfront
2. simulate an extent of inundation reaching at least to McKinley Street

For the slide at the Shoup Bay moraine (SBM64), it was recommended to

1. simulate an extent of inundation around Port Valdez and reproduce 20+ m runup at the Anderson Bay
2. simulate 10+ m wave inundating the navigation light, shown in Figure 36 by the red triangle, in Valdez Narrows
3. simulate 0.5m wave in the Valdez Hotel, shown in Figure 35 by the red triangle, located in the head of Port Valdez

4 Methodology for evaluating model performance

The observed data sets for the laboratory cases studied here are all in the form of slightly chirped, modulated packets representing time series of surface elevations at gauge locations. Observed results for Benchmark 2, $d = 61$ mm and $d = 120$ mm and for Benchmark 4 are shown in Figures 39-41. Time series of surface displacements in units of mm are shown in the upper plots, with gauge 1 at bottom and each time series offset by 20 mm. The lower plots in each figure show power spectra density $P_{\eta\eta}(f)$, with frequency f in units of Hz and power spectra in units of mm^2-s. Each gauge is offset by a power of 10 on the y-axis.

In the following subsections, we first describe several integral statistical measures used to evaluate model performance in Section 6. We then provide an overview of the wavelet transform and it's application to the evaluation of model performance, with results for individual models provide in Section 6.

4.1 Statistical measures of model performance

The first set of error measures are based on statistics obtained by integration in time over the entire signal.

4.1.1 RMS error measures

RMS error measures compare the structure of observations and simulations at each time, integrated over time. In order to apply these measures, it is necessary to interpolate data and model results onto similar discrete time axes. This operation is performed here by interpolating simulation results onto the time axis for observations. The comparison is carried out for each case over a time range corresponding to the existence of useful observational data. Since RMS error estimates for oscillatory signals are also highly sensitive to phase mismatches, the results obtained here are based on shifting simulation results in time in order to obtain a specific synchronization at one of the gauges. The details of the shifts are given separately for Benchmarks 2 and in Section 6.

The first error measure represents the square root of the mean square error between observation and simulation results, normalized by the difference between the largest maximum and minimum value of η. This measure is denoted by ϵ^g and is given by

$$\epsilon_j^g = \frac{\sqrt{\sum_i^N (\eta_m(i,j) - \eta_o(i,j))^2}}{\max_i(\eta_o(i,j)) - \min_i(\eta_o(i,j))}; \quad j = 1 : N_j \tag{8}$$

where N_j is the number of gauges in each experiment and N is the number of points in the time series. A second, alternate RMS error denoted ϵ^k is given by

$$\epsilon_j^k = \frac{\sqrt{\sum_i^N (\eta_m(i,j) - \eta_o(i,j))^2}}{\sqrt{\sum_i^N \eta_o(i,j)^2}}; \quad j = 1 : N_j \tag{9}$$

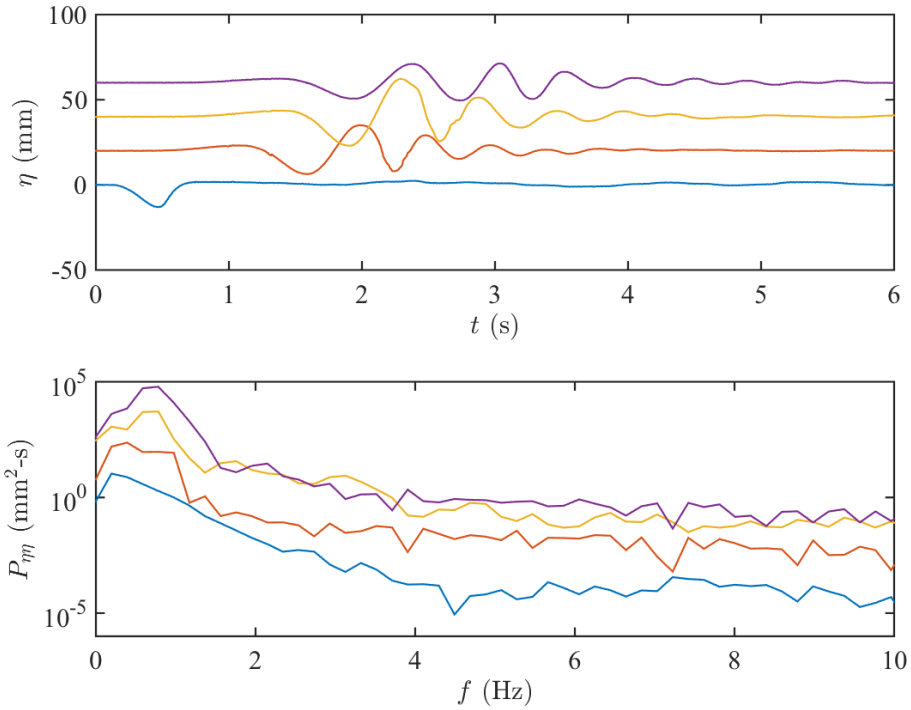

Figure 39: Benchmark 2, $d = 61$ mm: (top) Time series of surface elevation $\eta(t)$ for gauges 1-4 (bottom to top), and (bottom) Power spectral density $P_{\eta\eta}(f)$ for gauges 1-4 (bottom to top).

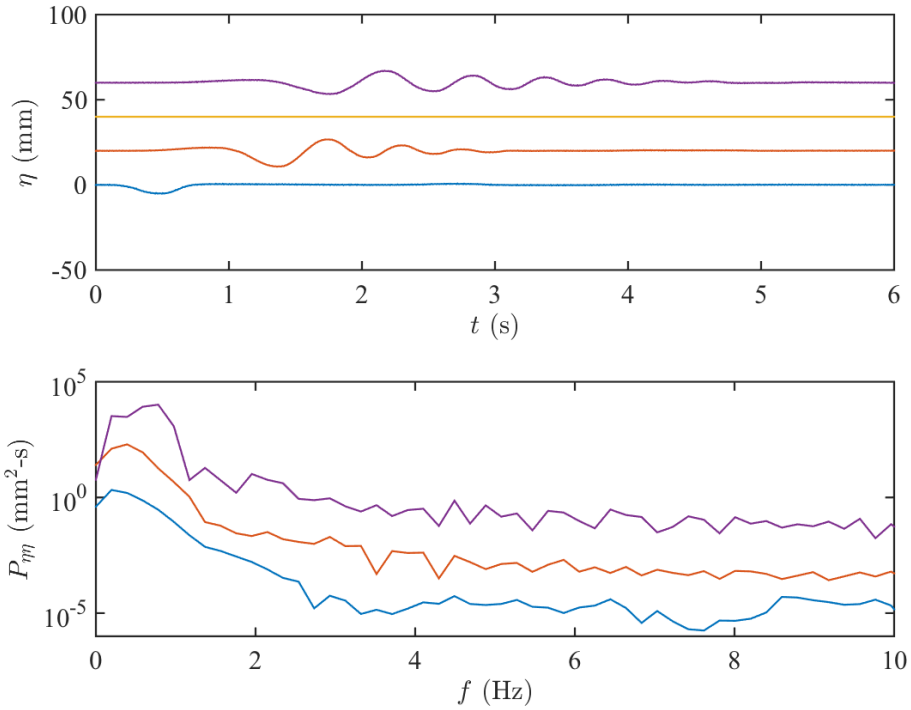

Figure 40: Benchmark 2, $d = 120$ mm: (top) Time series of surface elevation $\eta(t)$ for gauges 1-4 (bottom to top), and (bottom) Power spectral density $P_{\eta\eta}(f)$ for gauges 1-4 (bottom to top).

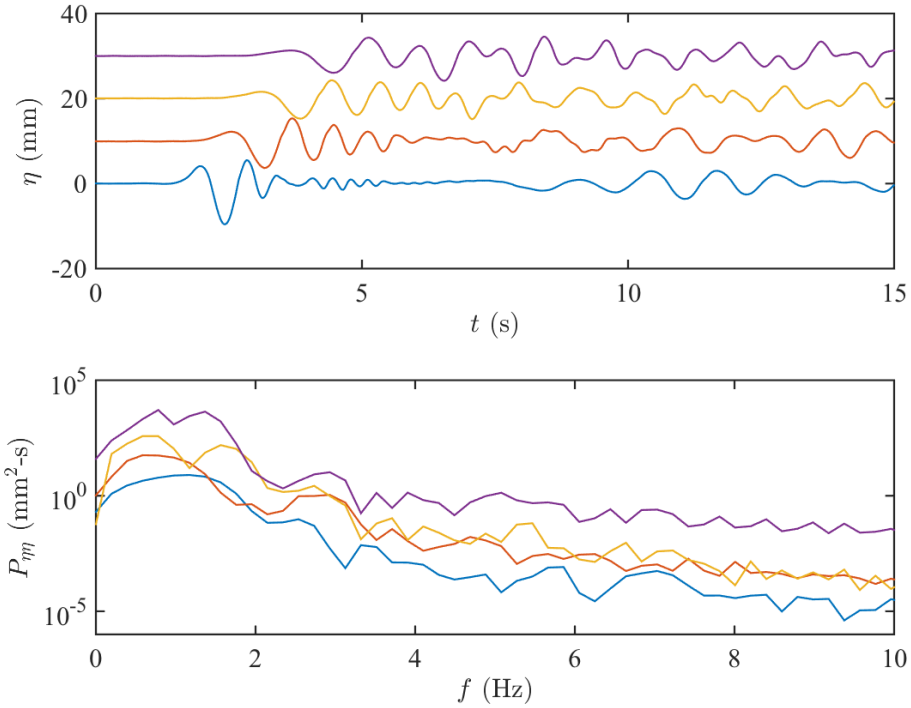

Figure 41: Benchmark 4: (top) Time series of surface elevation $\eta(t)$ for gauges 1-4 (bottom to top), and (bottom) Power spectral density $P_{\eta\eta}(f)$ for gauges 1-4 (bottom to top).

where the normalization is with respect to the standard deviation of the observations, again for each gauge. Results in Section 6 are shown for the first measure (8). Results based on (9) are numerically different but qualitatively similar in pattern, and are omitted.

4.1.2 Statistics of surface displacements

Additional measure were developed to quantify model reproduction of surface elevation maxima, surface elevation minima, maximum surface wave height, and wave packet variance:

- Maximum surface displacement for a single gauge, normalized by observed values

$$\epsilon_j^{(1)} = \mathrm{Max}_i(\eta_m(i,j))/\mathrm{Max_i}(\eta_o(i,j)); \quad j = 1 : N_j \tag{10}$$

- Minimum surface displacement for a single gauge, normalized by observed values

$$\epsilon_j^{(2)} = -\mathrm{Min}_i(\eta_m(i,j))/\mathrm{Min_i}(\eta_o(i,j)); \quad j = 1 : N_j \tag{11}$$

- Total surface excursion for each gauge, normalized

$$\epsilon_j^{(3)} = [\mathrm{Max}_i(\eta_m(i,j)) - \mathrm{Min_i}(\eta_m(i,j)]/[\mathrm{Max}(\eta_j^{obs}(t)) - \mathrm{Min}(\eta_j^{obs}(t)]; \quad j = 1 : N_j \tag{12}$$

- Total variance for each gauge, normalized by observed variance for each gauge

$$\epsilon_j^{(4)} = [\sum_{i=1}^{N} \eta_m(i,j)^2]/[\sum_{i=1}^{N} \eta_o(i,j)^2]; \quad j = 1 : N_j \tag{13}$$

4.2 Wavelet analysis of transient wave train behavior

Tsunami events typically consist of finite-length packets of waves with rapidly varying frequency and amplitude. An analysis of the distribution of amplitude and frequency in space and time can be revealing of the underlying fluid mechanics governing the propagation of the waves. In particular, we can examine the effects of frequency dispersion, or non-hydrostatic behavior, on the advancing wave. This analysis needs to be carried out using a framework that is appropriate for describing non-stationary behavior of the analyzed signal.

In this report, we perform this analysis using the Continuous Wavelet Transform (CWT) (see *Addison*, 2018, for a recent overview). To construct a picture of what is being done, consider 'sampling' some function $f(t)$ using a window $w(t-\tau)$, where the lag τ centers the observing window on the time axis. The resulting sample is a function both of time and the location of the sample window,

$$g(t,\tau) = f(t)w(t-\tau) \tag{14}$$

This operation provides localization in time for the sample. This function may then be Fourier transformed to obtain

$$\hat{g}(\omega,\tau) = \frac{1}{2\pi}\int_{-\infty}^{\infty} g(t,\tau)\mathrm{e}^{-i\omega t}dt = \frac{1}{2\pi}\int_{-\infty}^{\infty} f(t)w(t-\tau)\mathrm{e}^{-i\omega t}dt \tag{15}$$

The resulting transform $\hat{g}$ then provides information about the signal that is localized in frequency as well as time. Consider the typical case of sampling the signal with a unit amplitude window of length T, or

$$w(t-\tau) = \begin{cases} 0 & \mid t-\tau \mid > T/2 \\ 1 & \mid t-\tau \mid \leq T/2 \end{cases} \tag{16}$$

This leads to the result

$$\hat{g}_T(\omega,\tau) = \frac{1}{2\pi}\int_{\tau-T/2}^{\tau+T/2} f(t)\mathrm{e}^{-i\omega t}dt \tag{17}$$

the usual windowed Fourier Transform. For relatively small T's, This process may be thought of as a means of localizing transform information in time, but the general result has some undesirable properties. First, frequency resolution $\Delta\omega$ is controlled by the sample length T, and the only means for improving frequency resolution is to increase T and thus lose temporal localization. The converse is true, and the result is that the product $T\Delta\omega$ is a constant, with T and $\Delta\omega$ individually constant over the entire transform space (ω,τ).

The constancy of the product is a consequence of a result analogous to the Heisenberg Uncertainty Principle limiting the combined uncertainty of knowledge of a particle's position and speed in quantum mechanics. This result cannot be circumvented in a given sampling procedure. However, steps can be taken to adaptively change frequency or temporal resolution in a manner that sacrifices frequency resolution at high frequencies (where the signal varies rapidly) in order to obtain better time localization, or to sacrifice time localization in slowly varying portions of the signal in order to improve frequency discrimination. The CWT is a popular tool for carrying this out. The CWT is usually defined as a function of lag τ and a scale a, where a may be roughly thought of as being the inverse of a frequency. We define the transform here as

$$T(\tau,a) = \frac{1}{\sqrt{a}}\int_{-\infty}^{\infty} w^*\left(\frac{t-\tau}{a}\right)dt \tag{18}$$

where $w((t-\tau)/a)$ is referred to as the 'analyzing wavelet', and varies in duration as a function of the scale a being analyzed. A relation between scale and frequency may be

established by examining the Fourier transform pair

$$\begin{aligned} \hat{f}(\omega) = F(f(t)) &= \frac{1}{2\pi} \int_{-\infty}^{\infty} f(t) \mathrm{e}^{-i\omega t} dt \\ f(t) = F^{-1}(\hat{f}(\omega) &= \int_{-\infty}^{\infty} \hat{f}(\omega) \mathrm{e}^{i\omega t} \end{aligned} \tag{19}$$

The transform of $f(t/a)$ then works out directly to

$$F(f(t/a)) = a\hat{f}(\omega a) \tag{20}$$

so that compressing time by a factor a amounts to multiplying frequency by that factor.

Here, we use a common choice for the analyzing wavelet given by the Morlet wavelet

$$w(t/a) = \mathrm{e}^{i(t/a)-(t/a)^2/2} = \mathrm{e}^{i\omega_0 t-(\omega_0 t)^2/2} \tag{21}$$

where $\omega_0 = 1/a$ is a chosen reference frequency which essentially determines the number of oscillations occuring within the wavelet's Gaussian envelope. The Fourier Transform of $w(t/a)$ is then given to a very good approximation by

$$\hat{w}(\omega a) = \mathrm{e}^{-(\omega a-\omega_0)^2} \tag{22}$$

and the transform is usually computed conveniently in Fourier space, rather than calculating the convolution integral in the time domain. An overview of the basic computational approach may be found in *Torrence and Campo* (1998)

To illustrate the application of the CWT to a tsunami signal, we show the measured time series $\eta(t)$ and the modulus of the wavelet transform $|T|$ as a function of frequency and time for Benchmark 2 data in Figure 42. In the lower panel in each plot, the magnitude of the wavelet transform $|T(t, f)|$ is shown, and a solid red curve shows the locus of times at which the maximum of $|T|$ occurs at each frequency f. The panel for Gauge 3 also shows two additional curves. For Benchmark 2, Gauge 3 is located downslope in the direction of landslide travel. A wave with frequency f traveling in this direction from locations x_1 to x_3 would traverse this distance in a time interval

$$t_3 - t_1 = \int_{x_1}^{x_3} dx/c^*(h(x), f) \tag{23}$$

where depth h varies in x and where the local speed of propagation $c^*(h, f)$ depends on h and, in the case of dispersive motion, frequency f. Two relevant speeds based on linear

wave theory are the phase speed c and the group velocity c_g, given in terms of wavenumber $k = 2\pi/L$ (where L is wavelength) by

$$c^2 = \frac{g}{k}\tanh kh; \qquad c_g = \frac{c}{2}\left(1 + \frac{2kh}{\sinh 2kh}\right) \tag{24}$$

with $g = 9.806$ being gravitational acceleration. In the limit of long waves ($kh \to 0$), both c and c_g are asymptotic to $\sqrt{gh}$, and dependence on frequency is lost. In this limit, all wave components in a multi-component wave train would travel at the same speed. This is the non-dispersive limit, characterized by either linear or nonlinear shallow water equations.

In Figure 42, the vertical red line represents the location of the initial packet during the drawdown process. For Gauge 3, the red dashed line represents replacing $c*$ in (23) by group velocity c_g, while the dotted red line represents replacing c^* by phase speed c. Intrinsically, we would expect the propagation of the energy content at each frequency to be governed by the group velocity, so that the solid red line and dashed red line would coincide. Several factors keep this from being apparent in this case. First, the slide is present in the domain during the propagation process, and thus phase speed or group velocity are affected by a time-varying bottom and are not straightforward to interpret. More important, however, is a processing artifact which reduces the apparent arrival time when the wavelet width is adjusted to improve time localization. Relaxation of this constraint in favor of improving frequency localization leads to better estimates of arrival time, since the estimate at each frequency is less contaminated by neighboring frequencies in the strongly dispersive cases considered. The effect is illustrated in Figure 43, where results for Benchmark 4, Gauge 3 are shown for scaled center frequencies $\omega_0 = 5$ (left) and 15 (right). The improvement in agreement with linear theory and propagation at the group velocity is apparent. Since this result is expected and should be intrinsic to all the cases considered, we show all results in Section 6 in terms of wavelets with higher temporal resolution. We utilize arrival times at each gauge and frequency in model/data comparisons, in order to assess the accuracy of models to represent propagation at each component frequency.

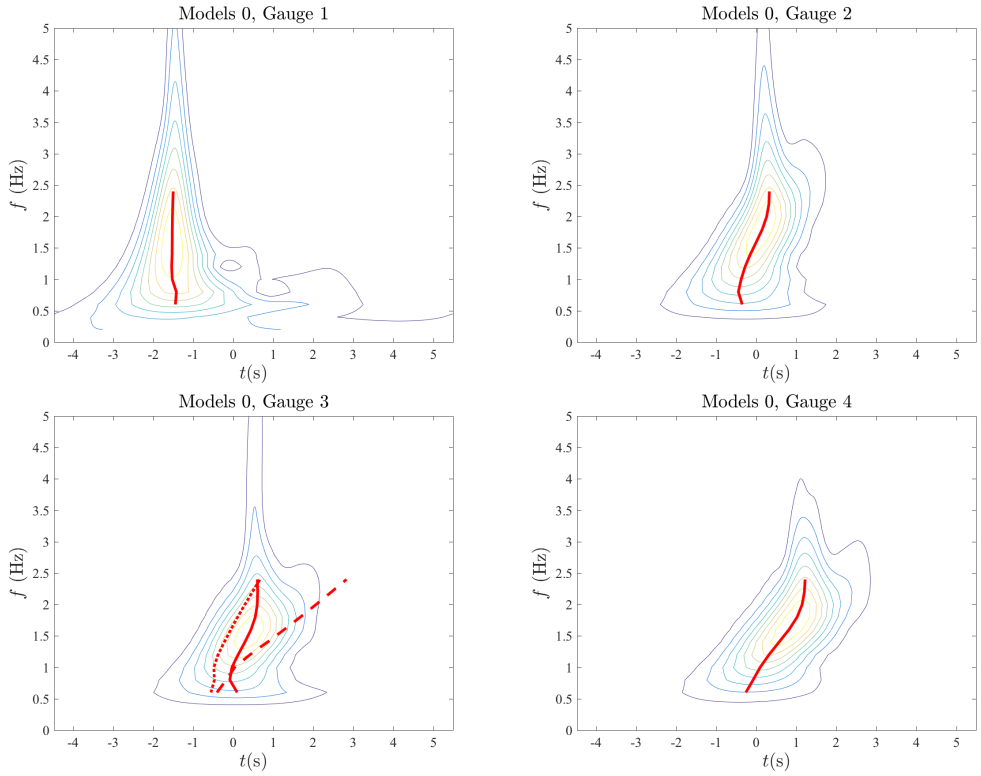

Figure 42: Benchmark 2, $d = 61$ mm: Modulus of wavelet transform $|T|$ of measured surface displacements at gauges 1-4

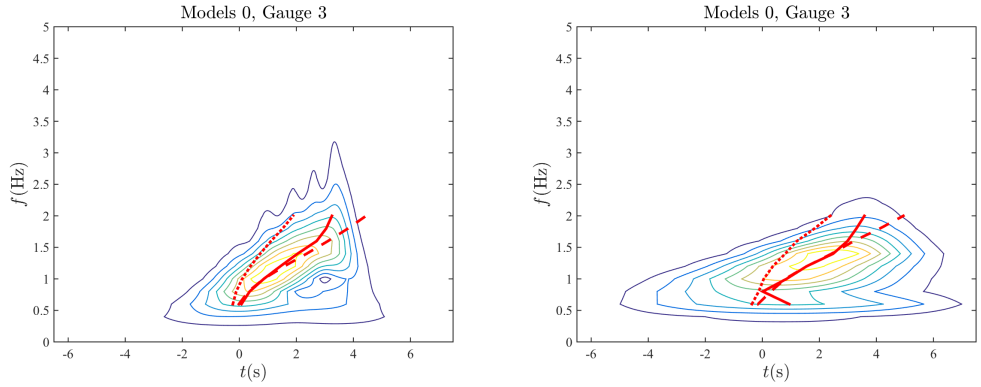

Figure 43: Benchmark 4: Wavelet transforms and arrival times at Gauge 3 for (left) $\omega_0 = 5$ and (right) $\omega_0 = 15$.

5 Models submitted for benchmarking

Participants from nine different institutions or groups of institutions submitted models for testing. The submissions are indicated in Table 7. The groups included

1. University of Delaware/Old Dominion University/University of Rhode Island: NHWAVE
2. University of Oslo: GloBouss and BoussCLAW
3. Texas A& M University at Galveston: TSUNAMI3D
4. University de Pau: THETIS
5. Sharif University: LS3D and 2LCMFlow
6. University of Alaska, Fairbanks: Alaska GI-L
7. University of Malaga: Landslide-HYSEA
8. Institute of Ocean Sciences (Sydney): FBSlide
9. University of Southern California: models based on NLSW and MS equations (referred to as LYNETT models).

Table 7 lists a total of 20 different model configurations tested. This multiplicity occurs because several of the models can be run in a variety of configurations. For example, the UD/ODU/URI model NHWAVE may be configured to run with a moving bottom (representing a solid slide or slump mass), a slide layer with viscous fluid rheology, a slide layer with granular flow rheology, or a fully 3D model with dispersed slide mass. Additionally, the model may be run in either a hydrostatic or non-hydrostatic configuration, leading in all to 6 out of the 20 model configurations tested.

For the purposes of comparison, the models have been grouped into four hydrodynamic configurations, including

1. Hydrostatic models with no frequency dispersion (indicated in charts by circles)
2. Boussinesq or one-layer, weakly dispersive models (indicated by 5-pointed stars)
3. Multi-layer or nonhydrostatic models (indicated by 6-pointed stars)
4. Fully-3D Navier-Stokes solvers with surface reconstruction (indicated by asterisks)

Additionally, modeled slide behavior is grouped into four categories including

1. Solid slides (usually as imposed bottom deformation in time; indicated by red symbols)

2. Viscous slides (indicated by green symbols)

3. Granular slides (indicated by blue symbols)

4. 3D, continuously varying phase or multiphase (indicated by black symbols).

A brief introduction to each hydrodynamic type and slide type is provided in the following two sections. A more complete introduction to each model and to its range of configurations in the present tests may be found in the individual model write-ups, posted on the workshop website at http://www1.udel.edu/kirby/landslide/reporting.html

Model name	**Model #**	**Hydro Type**	**Slide Type**	**Numerical**	BM1	BM2-d61	BM2-d120	BM3-case30	BM3-case32	BM4-test17	BM5 Case 1	BM5 Case 2	BM6	BM7	submitted by
data	0				y	y	y	y	y	y	y	y	y	y	
nhwave-s	1	3	1	2	y	y	y	y	y						UD/ODU/URI
nhwave-v	2	3	2	2						y				y	UD/ODU/URI
nhwave-g	3	3	3	2						y	y	y			UD/ODU/URI
globouss-l	4	2	1			y	y								Nor. Geotech. Inst.
globous-nl	5	2	1			y	y								Nor. Geotech. Inst.
boussclaw-0	6	2	1			y	y								Nor. Geotech. Inst.
boussclaw-15	7	2	1			y	y								Nor. Geotech. Inst.
tsunami3d	8	4	4			y	y			y				y	TAMUG
thetis-newt	9	4	4					y		y	y				U. de Pau
nhwave-3d	10	3	4	2						y					UD/ODU/URI
thetis-mui	11	4	4								y				U. de Pau
ls3d	12	2	1			y	y							y	Sharif U.
2lcmflow	13	1	3	2						y	y				Sharif U.
Alaska GI-L	14	1	2			y	y			y				y	U. Alaska
nhwave-s-hydrostatic	15	1	1	2		y	y								UD/ODU/URI
nhwave-g-hydrostatic	16	1	3	2						y					UD/ODU/URI
landslide-hysea	17	3*	3			y	y			y				y	U. Malaga
fbslide	18	1	1			y	y								IOS
Lynett-nlsw	19	1	1			y	y								USC
Lynett-MSE	21	3	1			y	y								USC
*benchmark 7 was carried out using a hydrostatic version of the hydrodynamic model in Landslide-hysea															
Hydro Types		**Slide Types**													
0 - data		1 - moving boundary													
1 - non-dispersive		2 - viscous layer													
2 - weakly dispersive, one layer		3 - granular layer													
3 - nonhydrostatic		4 - 3D multiphase													
4- Navier Stokes															

Table 7: Models with results submitted for comparison to data.

5.1 Treatment of hydrodynamics in models

The models considered in this exercise fall into the four categories describe below. Details of the formulation of each model are left to the writeups provided by each modeling group, which may be found at http://www1.udel.edu/kirby/landslide/models.html.

5.1.1 Non-dispersive models

Models in the non-dispersive category generally solve the Nonlinear Shallow Water Equations (NLSWE). In this class of model, the pressure field is assumed to be hydrostatic with respect to the local water surface, or

$$p = \rho g(\eta - z) \tag{25}$$

where ρ is water density, η is the water surface displacement away from rest, and $\eta - z$ represents the distance below the surface. As a result of this simplification, horizontal pressure gradients are depth-uniform, and hence horizontal velocities are uniform over depth if the effects of turbulence and bottom drag are neglected. Models of this type are historically known to be good simulators of runup and inundation, but they can accumulate significant errors when used to propagate waves over long distances or over depths which are not small compared to horizontal wavelengths. In the linear limit, waves in this category have the frequency-independent phase speed $c_0 = \sqrt{gh}$, where h is still water depth.

5.1.2 Weakly dispersive, Boussinesq-type models

On the surface of finite-depth water linear waves have a phase speed c given by

$$c = c_0 \left(\frac{\tanh kh}{kh} \right)^{1/2} \tag{26}$$

where $k = 2\pi/L$ is the wavenumber and L is the corresponding wave length. For most cases of tsunami generation, propagation and inundation, the dimensionless number kh (or, essentially, the ratio of water depth to wavelength) is relatively small. The limit of $kh \to 0$ recovers the non-dispersive model. The class of weakly-dispersive models (including Boussinesq, Serre and Greene-Naghdi models) retains additional information about c for finite but small values of kh. This information is usually related to an asymptotic form of the Taylor series for the added factor in (26); for example,

$$\frac{\tanh kh}{kh} = 1 - \frac{1}{3}(kh)^2 + O((kh)^4) \tag{27}$$

The corresponding corrections to the water velocity are usually obtained in the form of a power series in z, and various models may retain higher-order information in powers of kh, or may use series manipulation to obtain rational polynomial forms of (27) which

are more accurate or better behaved for large kh. Models in the following category of dispersive models may be reduced to this form if lowest-order treatments of the model's vertical structure are employed, such as restricting the model to a single vertical layer. See *Kirby* (2016) for a recent overview.

5.1.3 Dispersive models

Models in this category are essentially solutions of the full hydrodynamic problem under a restrictive set of simplifying assumptions. In particular, the water surface being solved for is assumed to be a single-valued function of horizontal position and time. This assumption eliminates the potential for directly describing phenomena such as wave crest overturning during breaking. However, as a result, models in this class do not require the elaborate reconstruction of arbitrary surface geometries employed in more complete Navier-Stokes solvers. The models also typically employ a reduction of the vertical structure of problem to a finite number of coupled layers, using either low-order approximations of the dynamics in each layer (*Stelling and Zijlema*, 2003; *Bai and Cheung*, 2013), or simply using differencing stencils applied to the relatively low resolution vertical structure (*Ma et al.*, 2012). These models essentially reduce to Boussinesq models by reducing the number of vertical layers to one, or they may approach a full solution of the surface wave problem by allowing the number of vertical layers to be as large as needed. Models for perfect fluid hydrodynamics for surface waves with lengths of kh values appropriate to tsunamis are often adequately described using three vertical layers.

5.1.4 Models based on Navier-Stokes solvers

Models in this final category typically solve the full set of Navier Stokes equations together with boundary conditions applied at an arbitrary, unknown surface. Accurate reproduction of surface geometry requires a great deal of spatial and temporal resolution in the calculation, and hence models of this type typically are expensive to run in terms of time and computer resources. (Techniques such as Adaptive Mesh Refinement may make it possible in the future to greatly reduce the cost of such simulations by allowing for spatial and time-varying model resolution; see, for example, *Popinet* (2003)).

5.2 Treatment of slide rheology and motion in models

5.2.1 Solid slides

In this case, the slide motion and geometry are typically specified as a bottom boundary condition. For instance, single degree of freedom laws of motions have been developed for translational and rotational solid slide motions that have been used in models to this effect (e.g., *Grilli and Watts*, 1999; *Grilli et al.*, 2002; *Lynett and Liu*, 2003; *Grilli and Watts*, 2005; *Watts et al.*, 2003, 2005; *Day et al.*, 2005). Among the models featured in the

workshop, NHWAVE, GLOBOUS, BOUSCLAW, LS3D, FBSLIDE and LYNETT belonged to this class of models (see Table 7).

Note that with this approach, deforming slides with a specified geometry and deformation can also be specified as a bottom boundary condition (*Lynett and Liu*, 2003; *Grilli and Watts*, 2005), but as for solid cases, there is no coupling between the slide and water motions, with the latter only affecting the slide motion through simple coefficients (e.g., drag and added mass coefficients) (*Salmanidou et al.*, 2017).

An exception to this lack of coupling is, for instance, the work of *Abadie et al.* (2010) who used the multi-material Navier-Stokes model THETIS to simulate both deforming and rigid slides, with the latter represented by a fluid of very large viscosity. With this model, they accurately simulated the solid block experiments of *Liu et al.* (2005) (for both subaerial and submarine cases), without specifying the block law of motion, which was implicitly found in the model through an internal balance of forces.

5.2.2 Slides simulated as dense viscous fluids

Many early models (e.g., *Heinrich*, 1992; *Harbitz et al.*, 1993; *Assier-Rzadkiewicz et al.*, 1997; *Fine et al.*, 1998) and some recent models (e.g., *Løvholt et al.*, 2017) have simulated tsunami generation by deformable slides modeled in a bottom layer as a dense viscous fluid (Newtonian or non-Newtonian) (e.g., see recent review by *Yavari-Ramshe and Ataie-Ashtiani*, 2016). Water motion was either modeled in a single depth-integrated upper layer (two-layer models, e.g., *Heinrich*, 1992; *Harbitz et al.*, 1993; *Assier-Rzadkiewicz et al.*, 1997; *Fine et al.*, 1998) or in multiple layers (e.g., *Kirby et al.*, 2016; *Grilli et al.*, 2017, and see reviews herein). This motion was coupled to the motion of the bottom layer/slide through dynamic and kinematic equations at the slide-water interface. Depending on model type, water motion was based on solving various sets of equations with different featured physics, from hydrostatic, to non-hydrostatic/dispersive (for example, the two-layer models of *Kirby et al.*, 2016, in which the upper water layer is modeled with the non-hydrostatic σ-coordinate 3D model NHWAVE (*Ma et al.*, 2012)), or full Navier-Stokes (see,e.g., 2D or 3D Navier-Stokes equations to simulate subaerial or submarine slides modeled as dense Newtonian or non-Newtonian fluids by *Løvholt et al.*, 2008; *Ataie-Ashtiani and Shobeyri*, 2008; *Weiss et al.*, 2009; *Abadie et al.*, 2010, 2012; *Horrillo et al.*, 2013). Among the models featured in the workshop NHWAVE and ALASKAGIL belonged to this class of models; THETIS and TSUNAM3D also modeled slides as a dense viscous fluid layer but within a multi-material NS framework (see Table 7).

5.2.3 Slides simulated as saturated granular debris flows

A number of recent laboratory experiments have modeled tsunamis generated by subaerial landslides made of gravel (*Fritz et al.*, 2004; *Ataie-Ashtiani and Najafi-Jilani*, 2008; *Heller and Hager*, 2010; *Mohammed and Fritz*, 2012) or glass beads (*Viroulet et al.*, 2014). For

deforming underwater landslides and related tsunami generation, 2D experiments were performed by *Assier-Rzadkiewicz et al.* (1997), who used sand, *Ataie-Ashtiani and Najafi-Jilani* (2008), who used granular material, and *Grilli et al.* (2017) who used glass beads.

To simulate such experiments, models have been developed on the same principle as the dense fluid bottom layer, but for a bottom layer representing a granular medium or a debris flow (e.g., *George and Iverson*, 2011, 2014; *Ma et al.*, 2015; *Grilli et al.*, 2017). An other approach to simulate tsunami generation by granular slide or sediment motion has been to simulate flows induced by a varying sediment concentration (e.g., *Ma et al.*, 2013). Among the models featured in the workshop, NHWAVE, LANDSLIDE-HYSEA and 2LCMFLOW belonged to this class of model.

For a more comprehensive review of recent modeling work in these areas, see *Yavari-Ramshe and Ataie-Ashtiani* (2016).

5.2.4 Slides simulated as multiphase components in fully 3D settings

Here, Navier-Stokes equations are typically solved for multiple fluids/mediums, on of which is a deforming slide and the other water and air. An example is the multi-material model THETIS by *Abadie et al.* (2010), which was used to simulate deforming slides in a laboratory set-up or in the field (*Abadie et al.*, 2012). Other examples of this approach are described by *Ma et al.* (2013), *Horrillo et al.* (2013)a and *López-Venegas et al.* (2015). Among the models featured in the workshop, THETIS, TSUNAMI3D and one variant of NHWAVE belonged to this class of model.

6 Model/data and model/model intercomparisons

In this section, we evaluate submitted model results for Benchmarks 2 and 4 using the methods described in Section 4. We then provide a more qualitative analysis of results for Benchmark 7, where model results are subject both to the choice of model and the modeler's subjective treatment of information related to the provided input data.

Data needed to reconstruct the results shown here may be obtained from the workshop website at http://www1.udel.edu/kirby/landslide/reporting.html. In particular,

1. http://www1.udel.edu/kirby/landslide/report/formatted_results.zip provides data in a common format for the four conditions considered. Files in the unzipped folder are Matlab .mat files, each containing a single data array with dimension (N by 5). For Benchmarks 2 and 4, the array columns contain time (s) and surface displacements at gauges 1 -4 (mm). For Benchmark 7, the files are in a similar format, with columns 2-5 displaying elevations at the Navigation Light, Old Valdez Hotel, Point 37 and Point 38, all in meters (m).

   Each file name follows the following convention:

   bmX_mY_NOTE.mat

   where X denotes the benchmark number (2, 4 or 7) and Y denotes the model number as indicated in the following table. Possible NOTEs are "d061" or "d120" for the two depths of submergence in Benchmark 2, or "case1" for Benchmark 4, which indicates the data set Test17 and was the only case used. For each case in Benchmarks 2 and 4, model number X=0 indicates the observed data, reformatted into the same common format. (Observed time series data does not exist for Benchmark 7).

   Finally, we note that the folder contains submitted results for several of the models for Benchmarks 3 and 5. These results are provided for inspection but are not analyzed or otherwise represented in the final technical report.

2. http://www1.udel.edu/kirby/landslide/report/errors.zip provides a table of results for the individual model RMS errors (with models listed as indicated in Table 7) in the .mat file error_data.mat, and for the surface elevation errors (10) - (13) in the .mat file error_heights.mat.

3. http://www1.udel.edu/kirby/landslide/report/programs.zip contains the matlab scripts used to carry out data analysis and model/data comparisons. These scripts were written by J. T. Kirby (except for portions of the script for Benchmark 7, provided by D. Nicolsky) and are in the public domain. Please consult the readme file in the zipped programs folder to see a complete table of contents for the scripts used.

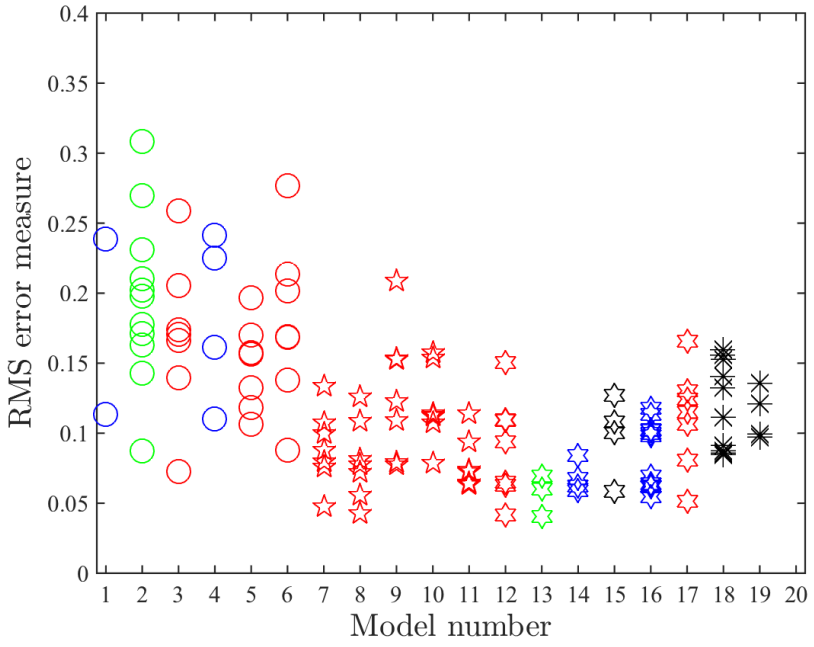

Figure 44: Distribution of RMS errors by model for all gauges.

6.1 RMS error estimates

We first consider the distribution of errors for each gauge as given by the error estimate ϵ^g defined in (8). In order to emphasize consistency between model types, we provide results here without regard to the performance of individual models. The reader may reconstruct these correspondences, if desired, by looking up individual error estimates in the files error_data.mat and stuff.mat, where the errors are listed with model numbers corresponding to entries in Table 7.

6.2 Wavelet analysis

Contrast results from the non-hydrostatic and hydrostatic versions of NHWAVE with a granular slide layer. These appear as Models 14 and 4 in Figures 44, 48 and 49, respectively. Figure 50, for the non-hydrostatic case, shows that models which reproduce dispersion properties accurately should correctly predict the arrival time of energy at distant gauges on a frequency by frequency basis. In contrast Figure 51, for the non-dispersive case, shows that energy at all frequencies is moving approximately at the same speed as the

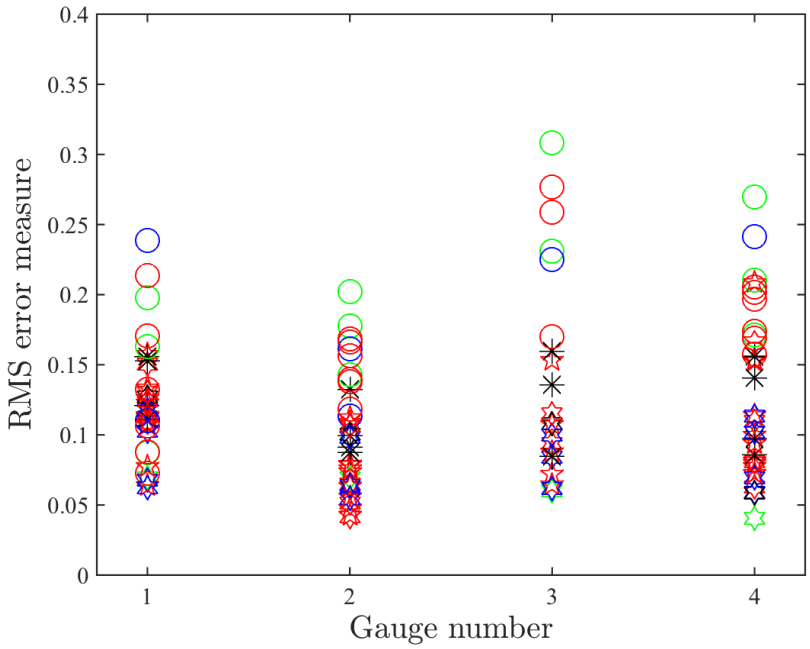

Figure 45: Distribution of RMS errors for all models by gauge.

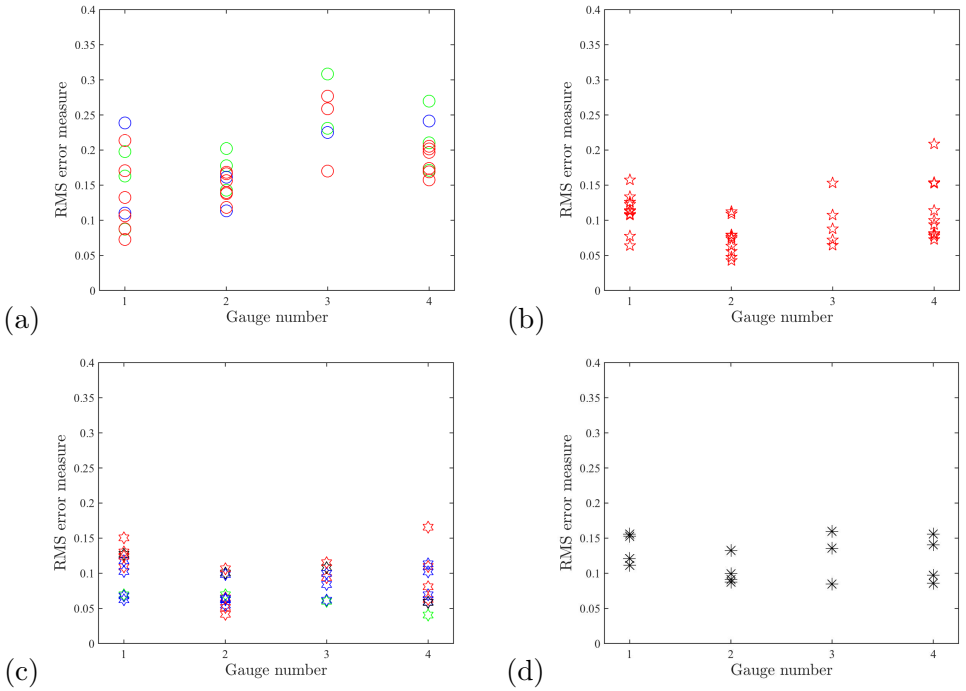

Figure 46: Distribution of RMS errors by hydrodynamic model type for each gauge. (a) Hydrostatic models, (b) Boussinesq models, (c) Non-hydrostatic models, (d) Navier-Stokes/VOF models.

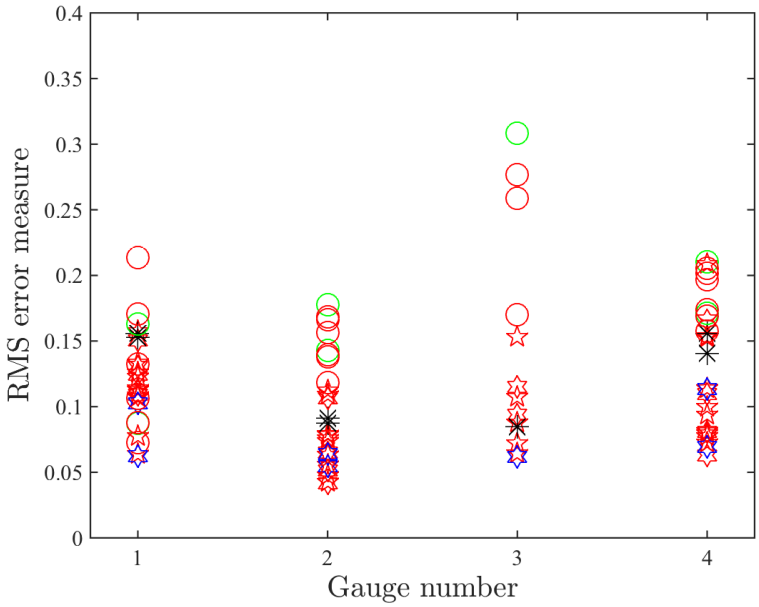

(a)

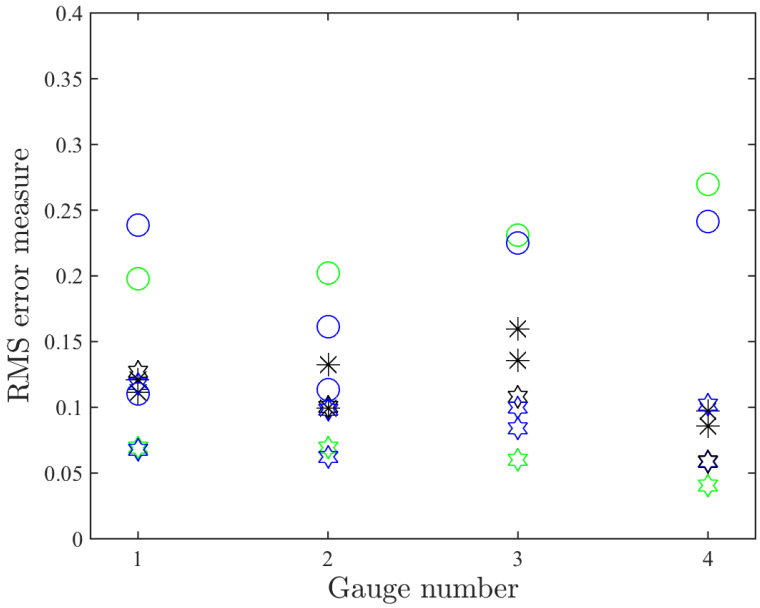

(b)

Figure 47: Distribution of RMS errors for all models by gauge for (a) Benchmark 2, $d =$ .061 m and $d =$ .120 m, and (b) Benchmark 4, Test 17.

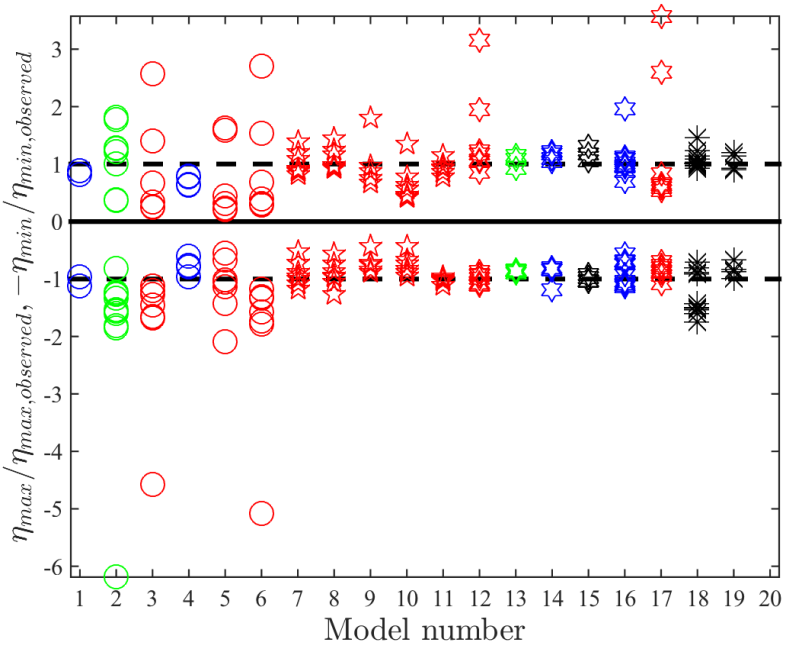

Figure 48: Normalized maximum positive and negative elevations for all cases.

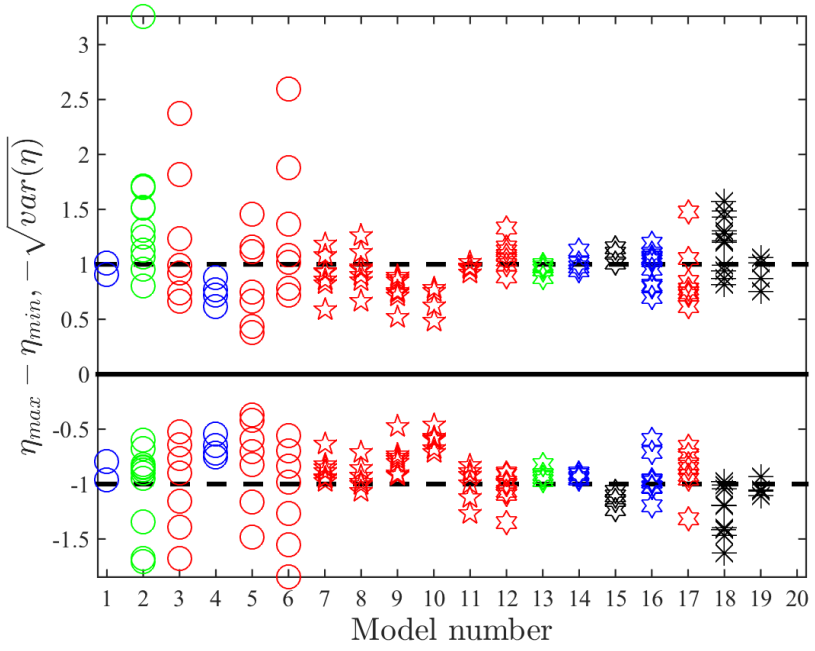

Figure 49: Normalized total excursion and variance for all cases.

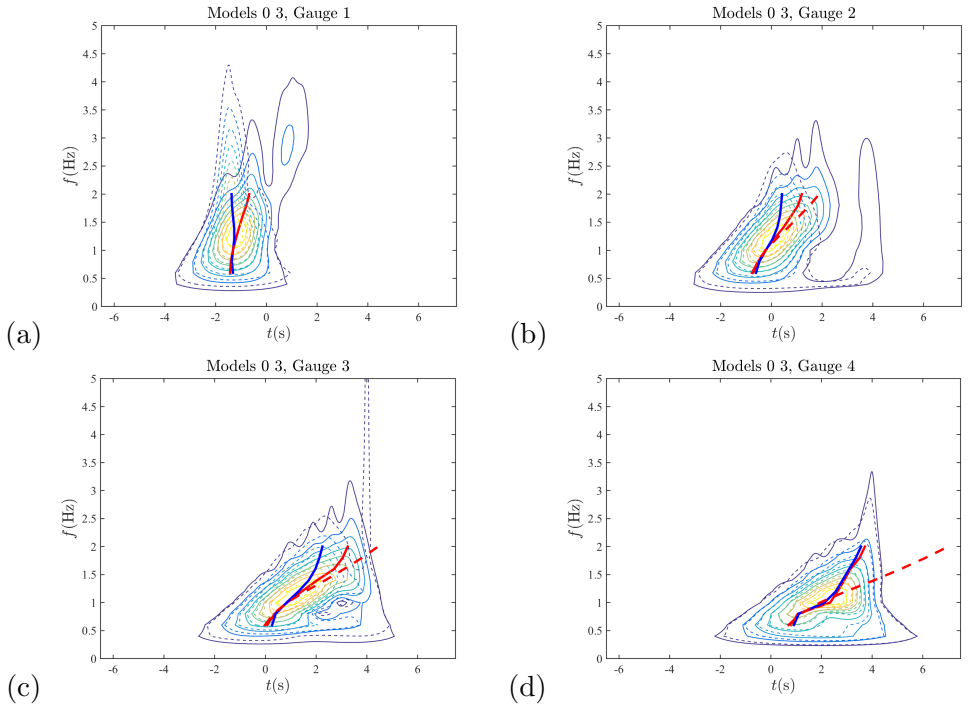

Figure 50: Wavelet transforms and arrival times for Benchmark 4, Model 3 (NHWAVE. granular slide, non-hydrostatic).

lower frequency components, which is consistent with the frequency-independent speed of $\sqrt{gh}$ for all frequencies in this limit.

(PLOT linear, shallow limit, deep limit, peregrine, nwogu dispersion for BM4)

Results for the wavelet analysis of all gauges, relative to observations, are given in Appendices D, E and F for all models for Benchmarks 2 ($d = 61$ mm), 2 ($d = 120$ mm) and 4, respectively.

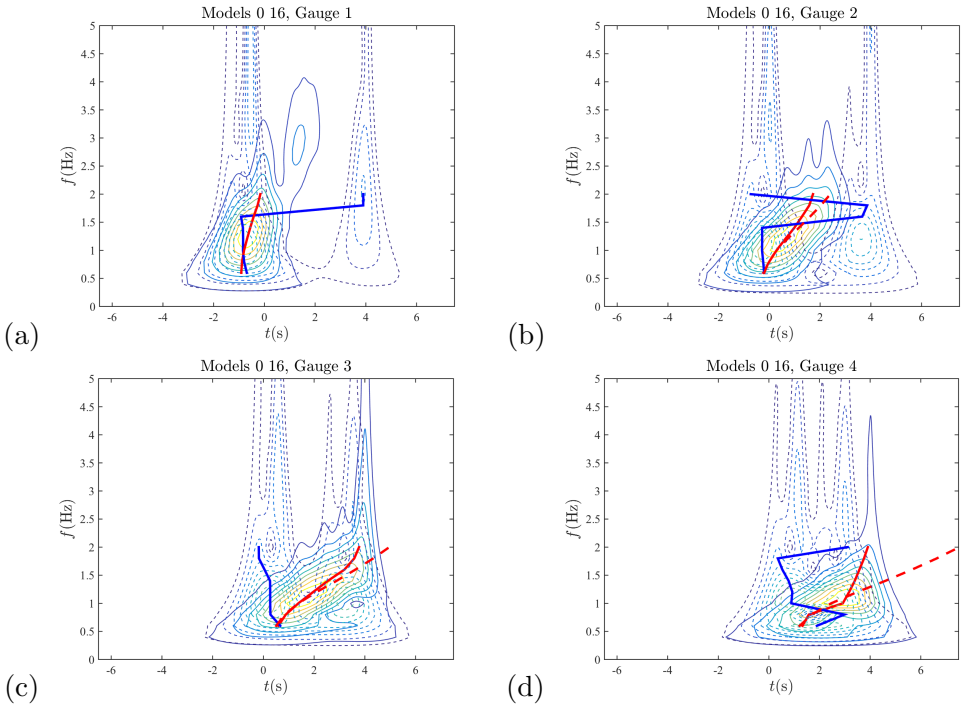

Figure 51: Wavelet transforms and arrival times for Benchmark 4, Model 16 (NHWAVE. granular slide, hydrostatic).

6.3 Benchmark 7: Qualitative analysis

Benchmark 7 differs from Benchmarks 2 and 4 in that there is less basis for a quantitative comparison to observations. In addition, results are subject to the choices made by each modeler in setting up the simulation, and thus it is possible that different results could be obtained by different modelers using the same model code. We proceed here by displaying the available results for

1. Water surface elevation time series at the Navigation Light and Valdez Hotel. (2, 8, 12, 14, 17)
2. Water surface elevation time series at points P37 and P38. (2, 8, 14, 17)
3. Maximum water surface elevation occurring over the Port Valdez domain. (2, 8, 14, 17)
4. Inundation line in Old Valdez (2, 8, 12, 14, 17)
5. Runups at points identified in *Plafker et al.* (1969) (2, 12)

where the numbers in brackets represent the models for which the data in question is available. Results were submitted for five models: NHWAVE (Model 2), TSUNAMI3D (Model 8), LS3D (Model 12), Alaska GI-L (Model 14) and Landslide-HYSEA (Model 17). Details for the setup of each model considered may be found in the individual model write-ups.

Time series of surface elevation at the Navigation Light, Hotel Valdez and points 37 and 38 are shown in Figures 52 - 55, with the results of both slides being superposed if they were provided separately. Time zero was taken to be the first indication of drawdown above Point 37, which is located over the HPV slide in front of Old Valdez. In the event that results for the two slides were superposed, it was assumed that the start times for each separate slide simulation were the same.

The results show interesting patterns of both agreement and difference. At Point 37, where the initial motion is simply the drawdown associated with the HPV slide failure, models 2 and 8, which utilize the same viscous slide model, show nearly similar results up until about 10 minutes in to the simulation, which coincides with the arrival of the SBM first wave front. In contrast, the granular slide used in Model 17 shows a drawdown which is more organized around the time following initial motion, reminiscent of the isolated drawdown at Gauge 1 seen in Benchmark 2 tests. The drawdown seen from TSUNAMI3D (Model 8) is more featureless in time and does not show nearly as much higher-frequency structure. Time series for Point 38 (at the Valdez shoreline) and the Valdez Hotel show the progression of the first wave resulting from the HPV slide, with the wave arriving at Point 38 slightly sooner in Model 14 (Hydrostatic) and in Models 2 and 17 (non-hydrostatic). Arrival times for the first wave at Hotel valdez are very consistent and are slightly higher for model 14 than for 2 and 17. (The reason for the apparent lag in model 8 results is

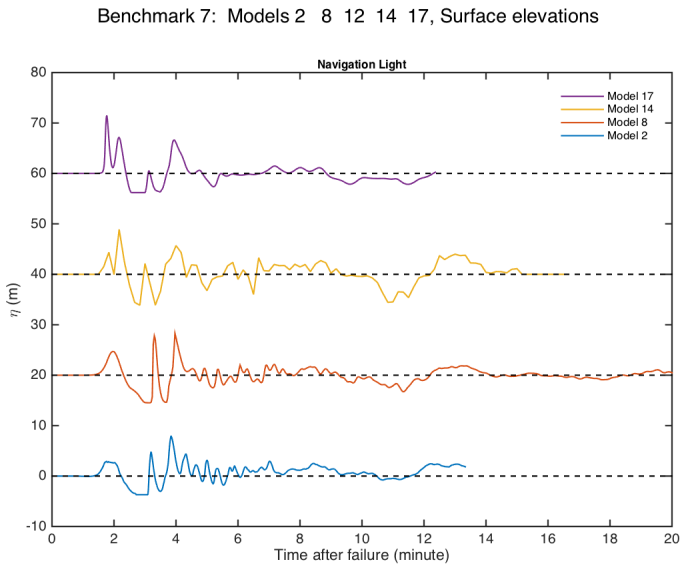

Figure 52: Simulated time series of water surface elevation at the Navigation Light.

being investigated.) (Time series results for Model 12 are qualitatively strange, indicating, for example, large drawdowns in the area of the Valdez waterfront in areas where any drawdown would expose land surface. These results are not displayed here, and reference is made to the individual modeler report.)

The first arrival at the Navigation Light results from the SBM slide in the western portion of the domain. In this case, Models 14 (viscous slide) and 17 (granular slide) give very consistent results for wave height at the Navigation Light, while Model 2 has a very different pattern of arriving waves. This result is discussed further below in connection with the spatial maps of maximum water level.

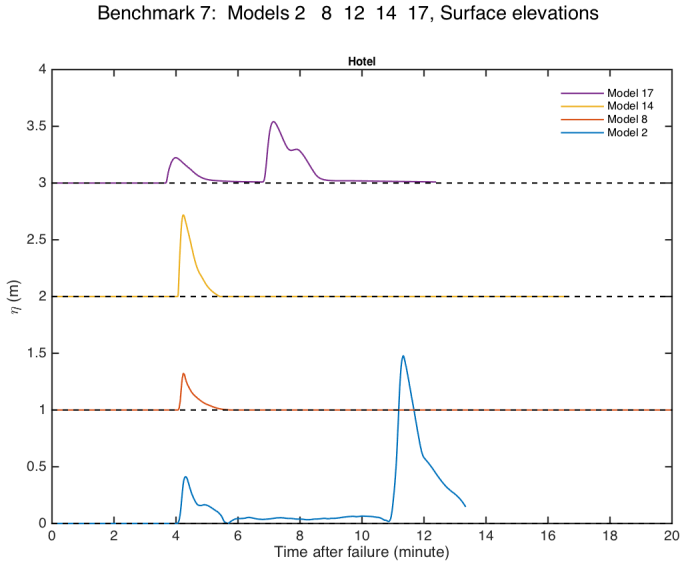

Figure 53: Simulated time series of water surface elevation at Hotel Valdez.

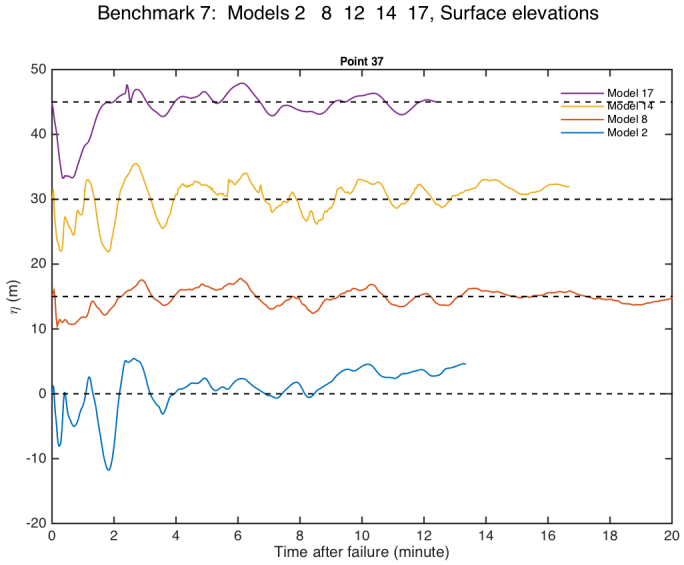

Figure 54: Simulated time series of water surface elevation at Point 37.

Lon.°	Lat.°	Plafker (m)	Model 2 (m)	Model 12 (m)
-146.5663	61.1224	51.	33.07	49.28
-146.5947	61.1309	6.	16.73	5.53
-146.6236	61.1168	21.	22.42	24.17
-146.6357	61.1118	37.	35.98	38.32
-146.6759	61.0833	18.	16.14	19.37
-146.6732	61.0786	23.	14.67	19.42
-146.6530	61.0811	11.	7.91	NaN
-146.6443	61.0724	17.	22.80	21.65
-146.6354	61.0758	23.	18.10	21.71
-146.6144	61.0829	10.	15.07	13.29
-146.5989	61.0839	15.	19.90	18.36
-146.5727	61.0777	15.	19.24	12.98
-146.5611	61.0783	20.	22.67	18.30
-146.5428	61.0789	20.	23.36	20.62
-146.5367	61.0793	24.	31.83	24.91
-146.4695	61.0781	12.	22.25	11.26
-146.4594	61.0805	23.	20.67	25.59
-146.4216	61.0850	11.	20.51	12.40
-146.3796	61.0888	9.	11.84	6.34
-146.4453	61.1340	10.	22.98	8.87
-146.4584	61.1339	9.	22.19	10.92
-146.4851	61.1300	18.	20.12	23.77
-146.4959	61.1266	12.	12.95	24.16
-146.5132	61.1232	11.	27.03	17.49
-146.5382	61.1244	27.	44.95	24.99

Table 8: Maximum runup at points reported by *Plafker et al.* (1969).

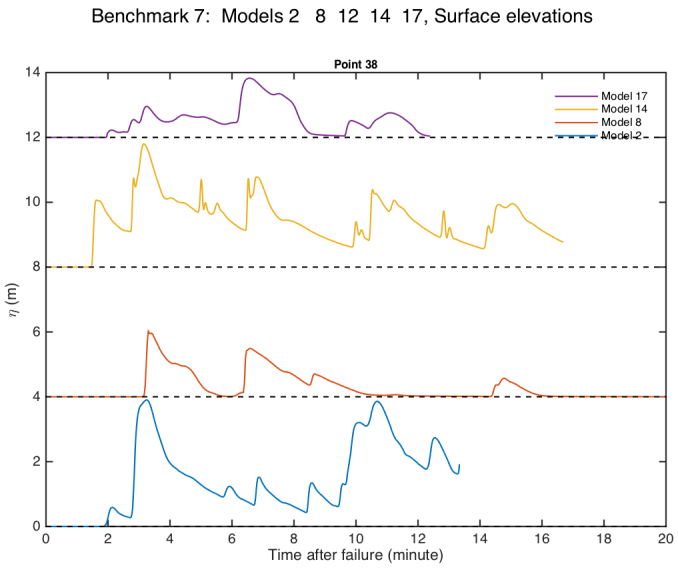

Figure 55: Simulated time series of water surface elevation at Point 38.

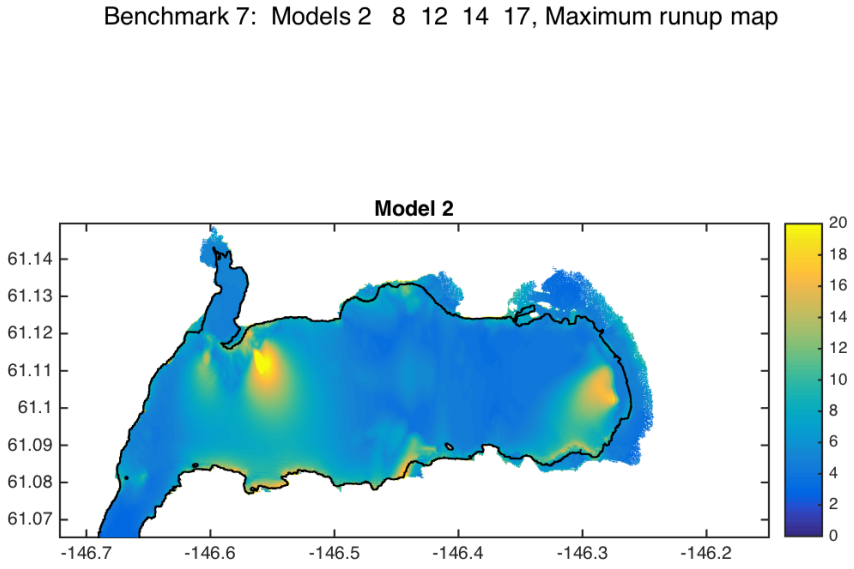

Figure 56: Maximum occurring water surface elevations over the Port Valdez domain. Model 2 (NHWAVE, viscous slide). Locations of Hotel Valdez and Navigation Light marked by ref and black triangles.

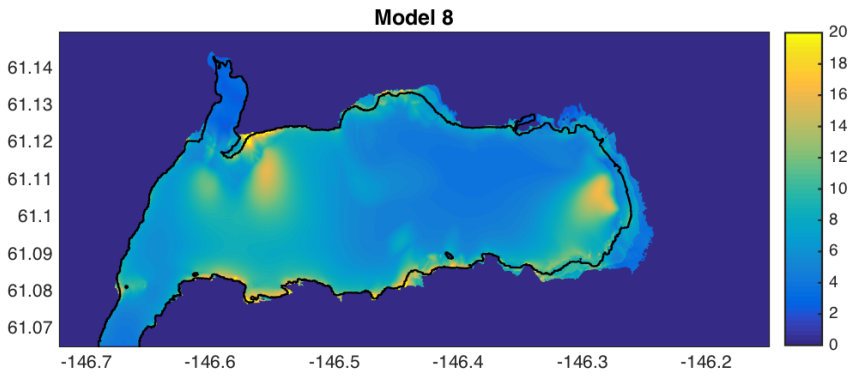

Figure 57: Maximum occurring water surface elevations over the Port Valdez domain. Model 8 (TSUNAMI3D).

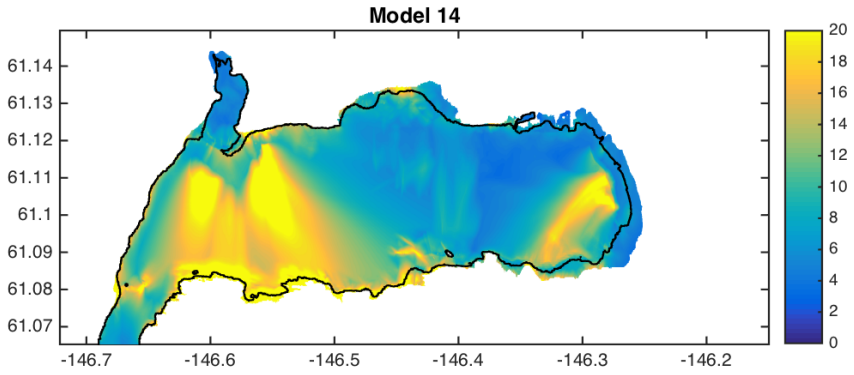

Figure 58: Maximum occurring water surface elevations over the Port Valdez domain. Model 14 (Alaska GI-L).

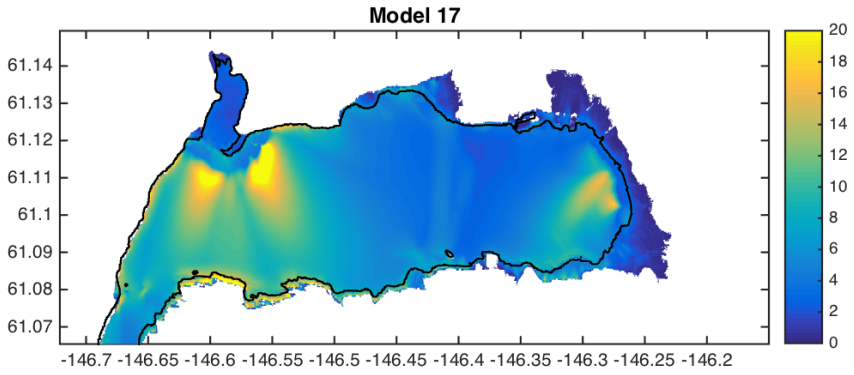

Figure 59: Maximum occurring water surface elevations over the Port Valdez domain. Model 17 (Landslide_HYSEA).

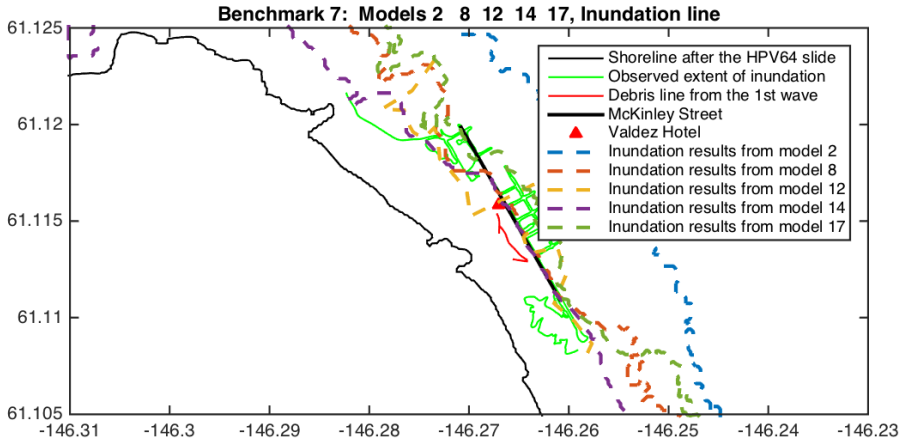

Figure 60: Simulated inundation lines around Old Valdez.

7 Conclusions and recommendations

7.1 Brief summary of Jan 11th, 2017 closing discussion

Before closing the workshop, an open discussion moderated by S. Grilli took place among participants. Below are some of the questions that were debated and some brief comments made, which inform the conclusions drawn at the end of this report.

(1) Comparison of models - can we draw conclusions on what models to use or not use for landslide modeling ?

- Phil Liu - comparing models to laboratory data - how does this affect validity with respect to field applications. Conclusions are relative to applications.
- Jorge Macias - does better modeling relative to benchmarks improve results of hazard assessments?
- Stephan Grilli - a number of experiments have been motivated by field cases - PNG/Enet, Lituya Bay/Fritz

(2) What is acceptable in terms of accuracy of models relative to benchmarks? Impact of source (slide) modeling.

- Accuracy threshold - may be able to get runup for Benchmark #2 and #4 - include in benchmark test evaluation?
- Stephan Grilli - Thresholds can be selected based on model performances versus the benchmarks.

(3) NTHMP - impact of rheology choices and modeling on inundation mapping?

(4) Gaps in modeling? Where should we go? What is next?

(5) What direction to move in modeling?

- Realistic geometries actually are quasi-stable, in terms of initial deposit.
- Scaling issues with respect to multi-material experiments.
- Collection of a better set of field cases is desirable, development of data sets as benchmark tests should made available for use.
- Limitations of field cases? Is modeling well enough constrained by available data?
- Finn Løvholt - deformable slide cases depend on reproduction of slide as well as hydrodynamics. It would be useful to develop a case where the slide kinematics are fixed? item How to proceed choosing slides?

- Homma Lee - there is no better guess than what you know. Keep using events you know well and move them around (proxy approach).
- Don't specify the use of some particular rheology in models.

(5) Dispersion effects on results?

- Importance of dispersion for runup behind the slides? May be reduced in some cases? (run demonstration to see)
- Dmitry Nicholsky - recommend when using a non-dispersive model is OK. Run some cases with and without dispersion to decide.
- Finn Løvholt - maybe one can utilize scaling arguments in relation to this distinction (Kajiura)
- Giorgio Bellotti - what parameters and aspects of slide behavior are critical in terms of controlling the hydrodynamic results?
- Pat Lynett - why use non-dispersive models since dispersive models are available?

(6) How should the workshop report be prepared?

- Rick Wilson - the report should contain some background based on invited presentations.
- Phil Liu - Report structure - intro and background; description of benchmark testing of models; discussions and directions for the future.
- Discussion of NTHMP/NOAA mandated caveats in report.

7.2 Conclusions and recommendations

Models ranging from non-dispersive, nonlinear shallow water equation (NLSWE) type to full Navier-Stokes solvers were applied and their results compared to the reference benchmark data; model results were also compared to each other to determine consistency within model type or class.

The most obvious outcome of the model/data comparison was that models of NLSWE type were found to be inappropriate for describing seaward propagation of landslide-generated waves for almost any distance away from the source region for the events considered. In contrast, all models which retained a degree of frequency dispersion were seen to be adequate in predicting wave evolution away from the source region, with comparable accuracy seen for Navier-Stokes models and non-hydrostatic models at all distances and with a slow increase in error with distance noted for Boussinesq models. The marked discrepancy between NLSWE models and other models was less distinct in the field benchmark case, where results from different models were more different largely due to variations in model setup.

Acknowledgements: This activity was supported by the National Tsunami Hazard Mitigation Program, NOAA, through grant NA15NWS4670029 to the University of Delaware. Logistical support for the workshop was provided by TAMUG.

References

Abadie, S., D. Morichon, S. Grilli, and S. Glockner (2010), Numerical simulation of waves generated by landslides using a multiple-fluid Navier-Stokes model, *Coastal Engineering*, *57*(9), 779–794.

Abadie, S., J. C. Harris, S. T. Grilli, and R. Fabre (2012), Numerical modeling of tsunami waves generated by the flank collapse of the Cumbre Vieja Volcano (La Palma, Canary Islands) : tsunami source and near field effects, *J. Geophys. Res.*, *117*, C05,030, doi: 10.1029/2011JC007646.

Addison, P. S. (2018), Introduction to redundancy rules: the continuous wavelet transform comes of age, *Philosophical Transactions of the Royal Society A*, *376*(20170258), doi: 10.1098/rsta.2017.0258.

Assier-Rzadkiewicz, S., C. Mariotti, and P. Heinrich (1997), Numerical simulation of submarine landslides and their hydraulic effects, *J. Waterway Port Coastal and Ocean Engng.*, *123*(6), 149–157.

Ataie-Ashtiani, B., and A. Najafi-Jilani (2008), Laboratory investigations on impulsive waves caused by underwater landslide, *Coastal Engineering*, *55*(12), 989–1004.

Ataie-Ashtiani, B., and G. Shobeyri (2008), Numerical simulation of landslide impulsive waves by incompressible smoothed particle hydrodynamics, *Intl. J. Num. Meth. Fluids*, *56*(2), 209–232.

Bai, Y., and K. F. Cheung (2013), Dispersion and nonlinearity of multi-layer non-hydrostatic free-surface flow, *Journal of Fluid Mechanics*, *726*, 226–260, doi:10.1017/jfm.2013.213.

Chaytor, J. D., E. L. Geist, C. K. Paull, D. W. Caress, R. Gwiazda, R. Urrutia Fucugauchi, and M. Rebolledo Vieyra (2016), Source characterization and tsunami modeling of submarine landslides along the Yucatán Shelf/Campeche Escarpment, southern Gulf of Mexico, *Pure and Applied Geophysics*, *173*(12), 4101–4116.

Coulter, H. W., and R. R. Migliaccio (1966), Effects of the earthquake of March 27, 1964 at Valdez, Alaska, *Geological Survey Professional Paper 542-C*, United States Dept. of Interior - Geological Survey.

Day, S. J., P. Watts, S. T. Grilli, and J. T. Kirby (2005), Mechanical models of the 1975 Kalapana, Hawaii earthquake and tsunami, *Marine Geology*, *215*(1-2), 59–92.

Enet, F., and S. T. Grilli (2007), Experimental study of tsunami generation by three-dimensional rigid underwater landslides, *Journal of Waterway, Port, Coastal and Ocean Engineering*, *133*(6), 442–454.

Fine, I., A. Rabinovich, B. Bornhold, R. Thomson, and E. Kulikov (2005), The Grand Banks landslide-generated tsunami of Novermber 18, 1929: Preliminary analysis and numerical modeling, *Marine Geology*, *215*, 45–57.

Fine, I. V., A. B. Rabinovich, and E. A. Kulikov (1998), Numerical modelling of landslide generated tsunamis with application to the Skagway Harbor tsunami of November 3, 1994, in *Proc. Intl. Conf. on Tsunamis, Paris*, pp. 211–223.

Fritz, H., W. Hager, and H.-E. Minor (2001), Lituya Bay case: Rockslide impact and wave run-up, *Sci. Tsunami Hazards*, *19*, 3–22.

Fritz, H., F. Mohammed, and J. Yoo (2009), Lituya Bay landslide impact generated mega-tsunami 50th anniversary, *Pure Appl. Geophys.*, *166*, 153–175.

Fritz, H. M., W. H. Hager, and H.-E. Minor (2004), Near-field characteristics of landslide generated impulse waves, *J. Waterw. Port Coastal Ocean Eng.*, *130*, 287–302.

Geist, E., P. Lynett, and J. Chaytor (2009), Hydrodynamic modeling of tsunamis from the Currituck landslide, *Marine Geology*, *264*, 41–52, doi:10.1016/j.margeo.2008.09.005.

George, D. L., and R. M. Iverson (2011), A two-phase debris-flow model that includes coupled evolution of volume fractions, granular dilatancy, and pore-fluid pressure, *Italian Journal of Engineering Geology and Environment*, *43*, 415–424.

George, D. L., and R. M. Iverson (2014), A depth-averaged debris-flow model that includes the effects of evolving dilatancy. ii. numerical predictions and experimental tests, *Proc. R. Soc. A*, *470*(2170), 20130,820.

Greene, H., and S. Ward (2003), Mass movement features along the central California margin and their modeled consequences for tsunami generation, in *Submarine Mass Movements and Their Consequences*, pp. 343–356, Springer Netherlands.

Greene, H., L. Murai, P. Watts, N. Maher, M. A. Fisher, C. Paull, and P. Eichhubl (2005), Submarine landslides in the Santa Barbara Channel as potential tsunami sources, *Natural Hazards and Earth System Science*, *6*(1), 63–88.

Grilli, S. T., and P. Watts (1999), Modeling of waves generated by a moving submerged body. Applications to underwater landslides, *Engng. Anal. Boundary Elements*, *23*, 645–656.

Grilli, S. T., and P. Watts (2005), Tsunami generation by submarine mass failure. i: Modeling, experimental validation, and sensitivity analysis, *Journal of Waterway, Port, Coastal and Ocean Engineering*, *131*(6), 283–297, doi:10.1061/(ASCE)0733-950X(2005)131:6(283).

Grilli, S. T., S. Vogelmann, and P. Watts (2002), Development of a 3D numerical wave tank for modeling tsunami generation by underwater landslides, *Engng. Anal. Boundary Elements*, *26*(4), 301–313.

Grilli, S. T., O.-D. S. Taylor, C. D. Baxter, and S. Maretzki (2009), Probabilistic approach for determining submarine landslide tsunami hazard along the upper East Coast of the United States, *Marine Geology*, *264*(1-2), 74–97, doi:10.1016/j.margeo.2009.02.010.

Grilli, S. T., S. Dubosq, N. Pophet, Y. Pérignon, J. T. Kirby, and F. Shi (2010), Numerical simulation and first-order hazard analysis of large co-seismic tsunamis generated in the Puerto Rico trench: near-field impact on the north shore of Puerto Rico and far-field impact on the US East Coast, *Natural Hazards and Earth System Sciences*, *10*, 2109–2125, doi:10.5194/nhess-2109-2010.

Grilli, S. T., C. O'Reilly, J. C. Harris, T. Tajalli-Bakhsh, B. Tehranirad, S. Banihashemi, J. T. Kirby, C. D. P. Baxter, T. Eggeling, G. Ma, and F. Shi (2015), Modeling of SMF tsunami hazard along the upper US East Coast: Detailed impact around Ocean City, MD, *Natural Hazards*, *76*(2), 705–746, doi:10.1007/s11069-014-1522-8.

Grilli, S. T., M. Shelby, O. Kimmoun, G. Dupont, D. Nicolsky, G. Ma, J. T. Kirby, and F. Shi (2017), Modeling coastal tsunami hazard from submarine mass failures: effect of slide rheology, experimental validation, and case studies off the U S East Coast, *Natural Hazards*, *86*, 353–391, doi:10.1007/s11069-016-2692-3.

Harbitz, C., G. Pedersen, and B. Gjevik (1993), Numerical simulations of large water waves due to landslides, *J. Hydraul. Engng.*, *119*, 1,325–1,342.

Heinrich, P. (1992), Nonlinear water waves generated by submarine and aerial landslides, *J. Waterway Port Coastal and Ocean Engng.*, *118*, 249–266.

Heller, V., and W. H. Hager (2010), Impulse product parameter in landslide generated impulse waves, *J. Waterway Port Coastal and Ocean Engng.*, *136*, 145–155.

Horrillo, J., A. Wood, G.-B. Kim, and A. Parambath (2013), A simplified 3-D Navier-Stokes numerical model for landslide-tsunami: Application to the Gulf of Mexico, *J. Geophys. Res. Oceans*, *118*, 6934–6950.

Horrillo, J., S. Grilli, D. Nicolsky, V. Roeber, and J. Zhang (2014), Performance benchmarking tsunami operational models for NTHMP's' inundation mapping activities, *Pure Appl Geophysics*, *172*, 869–884, doi:10.1007/s00024-014-0891-y.

Ichinose, G., P. Somerville, H. Thio, R. Graves, and D. O'Connell (2007), Rupture process of the 1964 Prince William Sound, Alaska, earthquake from the combined inversion of seismic, tsunami, and geodetic data, *J. Geophys. Res., Solid Earth*, *112*(B7).

Kirby, J. T. (2016), Boussinesq models and their application to coastal processes across a wide range of scales, *Journal of Waterway, Port, Coastal and Ocean Engineering*, (03116005), doi:10.1061/(ASCE)WW.1943-5460.0000350.

Kirby, J. T., F. Shi, D. Nicolsky, and S. Misra (2016), The 27 April 1975 Kitimat, British Columbia submarine landslide tsunami: A comparison of modeling approaches, *Landslides*, *13*, 1421–1434, doi:10.1007/s10346-016-0682-x.

Liu, P. L.-F., T.-R. Wu, F. Raichlen, C. E. Synolakis, and J. C. Borrero (2005), Runup and rundown generated by three-dimensional sliding masses, *Journal of Fluid Mechanics*, *536*, 107–144, doi:10.1017/S0022112005004799.

López-Venegas, A., U. ten Brink, and E. Geist (2008), Submarine landslide as the source for the October 11, 1918 Mona Passage tsunami: Observations and modeling, *Mar. Geol.*, *254*(1), 35–46.

López-Venegas, A., J. Horrillo, A. Pampell-Manis, V. Huérfano, and A. Mercado (2015), Advanced tsunami numerical simulations and energy considerations by use of 3D–2D coupled models: the October 11, 1918, Mona Passage Tsunami, *Pure Appl. Geophys.*, *172*(6), 1679–1698.

Løvholt, F., G. Pedersen, and G. Gisler (2008), Oceanic propagation of a potential tsunami from the La Palma Island, *J. Geophys. Res.*, *113*(C09026).

Løvholt, F., S. Bondevik, J. S. Laberg, J. Kim, and N. Boylan (2017), Some giant submarine landslides do not produce large tsunamis, *Geophysical Research Letters*, *44*(16), 8463–8472.

Lynett, P., and P.-F. Liu (2003), A numerical study of submarine landslide-generated waves and runup, *Proc. Roy. Soc.*, *A*(458), 2885–2910.

Lynett, P., and thirty-seven alia (2017), Inter-model analysis of tsunami-induced coastal currents, *Ocean Modelling*, *114*, 14–32, doi:10.1016/j.ocemod.2017.04.003.

Ma, G., F. Shi, and J. T. Kirby (2012), Shock-capturing non-hydrostatic model for fully dispersive surface wave processes, *Ocean Modelling*, *43–44*, 22–35, doi:10.1016/j.ocemod.2011.12.002.

Ma, G., J. T. Kirby, and F. Shi (2013), Numerical simulation of tsunami waves generated by deformable submarine landslides, *Ocean Modelling*, *69*, 146–165, doi:10.1016/j.ocemod.2013.07.001.

Ma, G., J. T. Kirby, T.-J. Hsu, and F. Shi (2015), A two-layer granular landslide model for tsunami wave generation: Theory and computation, *Ocean Modelling*, *93*, 40–55, doi:10.1016/j.ocemod.2015.07.012.

Mohammed, F., and H. M. Fritz (2012), Physical modeling of tsunamis generated by three-dimensional deformable granular landslides, *Journal of Geophysical Research*, *117*(C11015), doi:10.1029/2011JC007850.

Nicolsky, D., E. N. Suleimani, P. J. Haeussler, H. F. Ryan, R. D. Koehler, R. A. Combellick, and R. A. Hansen (2013), Tsunami inundation maps for port valdez, alaska, *Report of Investigations 2013-1*, State of Alaska Department of Natural Resources.

Parsons, T., E. L. Geist, H. F. Ryan, H. J. Lee, P. J. Haeussler, P. Lynett, P. E. Hart, R. Sliter, and E. Roland (2014), Source and progression of a submarine landslide and tsunami: The 1964 great alaska earthquake at valdez, *Journal of Geophysical Research: Solid Earth*, *119*, 8502–8516, doi:10.1002/2014JB011514.

Plafker, G., R. Kachadoorian, E. B. Eckel, and L. R. Mayo (1969), Effects of the earthquake of March 27, 1964 on various communities, *Geological Survey Professional Paper 542-G*, United States Dept. of Interior - Geological Survey.

Popinet, S. (2003), Gerris: a tree-based adaptive solver for the incompressible euler equations in complex geometries, *Journal of Computational Physics*, *190*, 572–600, doi:10.1016/S0021-9991(03)00298-5.

Salmanidou, D., S. Guillas, A. Georgiopoulou, and F. Dias (2017), Statistical emulation of landslide-induced tsunamis at the rockall bank, ne atlantic, *Proc. R. Soc. A*, *473*(2200), 20170,026.

Stelling, G. S., and M. Zijlema (2003), An accurate and efficient finite-difference algorithm for non-hydrostatic free-surface flow with application to wave propagation, *International Journal for Numerical Methods in Fluids*, *43*, 1–23, doi:10.1002/fld.595.

Tappin, D. R., S. T. Grilli, J. C. Harris, R. J. Geller, T. L. Masterlark, J. T. Kirby, F. Shi, G. Ma, K. Thingbaijamg, and P. Mai (2014), Did a submarine landslide contribute to the 2011 Tohoku tsunami ?, *Marine Geology*, *357*, 344–361, doi:10.1016/j.margeo.2014.09.043.

Tehranirad, B., J. C. Harris, A. R. Grilli, S. T. Grilli, S. Abadie, J. T. Kirby, and F. Shi (2015), Far-field tsunami hazard in the north Atlantic basin from large scale flank collapses of the Cumbre Vieja volcano, La Palma, *Pure and Applied Geophysics*, *172*(12), 3589–3616, doi:10.1007/s11069-014-1522-8.

ten Brink, U., and X. alia (2008), Evaluation of tsunami sources with the potential to impact the U.S. Atlantic and Gulf Coasts, *An updated report to the Nuclear Regulatory Commission by Atlantic and Gulf of Mexico Tsunami Hazard Assessment Group*, US Nuclear Regulatory Commission.

ten Brink, U. S., J. D. Chaytor, E. L. Geist, D. S. Brothers, and B. D. Andrews (2014), Assessment of tsunami hazard to the US Atlantic margin, *Marine Geology*, *353*, 31–54.

Torrence, C., and G. P. Campo (1998), A practical guide to wavelet analysis, *Bulletin of the American Meteorological Society*, *79*, 61–78.

Viroulet, S., A. Sauret, and O. Kimmoun (2014), Tsunami generated by granular collapse down a rough inclined plane, *European Physics Letters*, *105*(3), 34,004, doi:10.1209/0295-5075/105/34004.

Ward, S. N., and S. Day (2001), Cumbre Vieja volcano—potential collapse and tsunami at La Palma, Canary Islands, *Geophys. Res. Lett.*, *28*(17), 3397–3400.

Watts, P., S. T. Grilli, J. T. Kirby, G. J. Fryer, and D. R. Tappin (2003), Landslide tsunami case studies using a Boussinesq model and a fully nonlinear tsunami generation model, *Natural Hazards and Earth System Sciences*, *3*, 391–402.

Watts, P., S. T. Grilli, D. R. Tappin, and G. J. Fryer (2005), Tsunami generation by submarine mass failure Part II : Predictive equations and case studies, *J. Waterway Port Coastal and Ocean Engng.*, *131*(6), 298–310, doi:10.1061/(ASCE)0733-950X(2005)131:6(298).

Weiss, R., H. M. Fritz, and K. Wuennemann (2009), Hybrid modeling of the mega-tsunami runup in Lituya Bay after half a century, *Geophys. Res. Lett.*, *36*(L09602), doi:10.1029/2009GL037814.

Wilson, B., and A. Torum (1972), *The Great Alaska Earthquake of 1964:*, chap. Effects of the tsunamis - An engineering study, pp. 361– 526., National Academy of Sciences - Engineering, Washington DC.

Wu, T.-R. (2004), A numerical study of three-dimensional breaking waves and turbulence effects, Ph.D. thesis, Cornell University.

Yavari-Ramshe, S., and B. Ataie-Ashtiani (2016), Numerical modeling of subaerial and submarine landslide generated tsunami waves - Recent advances and future challenges, *Landslides*, *13*(6), 1325–1368.

A Model simulation results: Benchmark 2, $d = 61$ mm

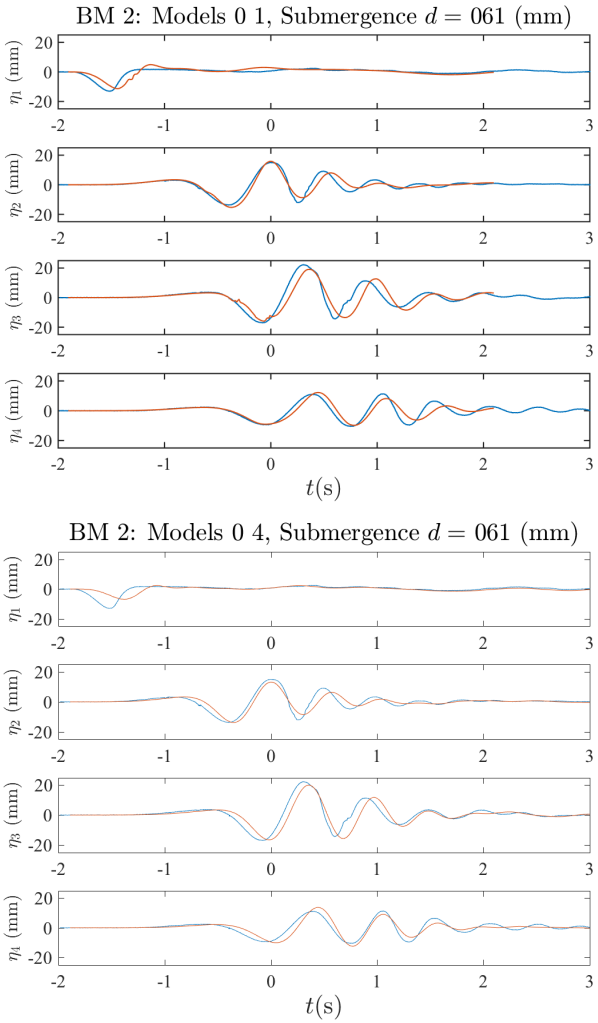

Figure 61: Benchmark 2: $d = 61$ mm. Models 1, 4. Observed and simulated water surface displacements.

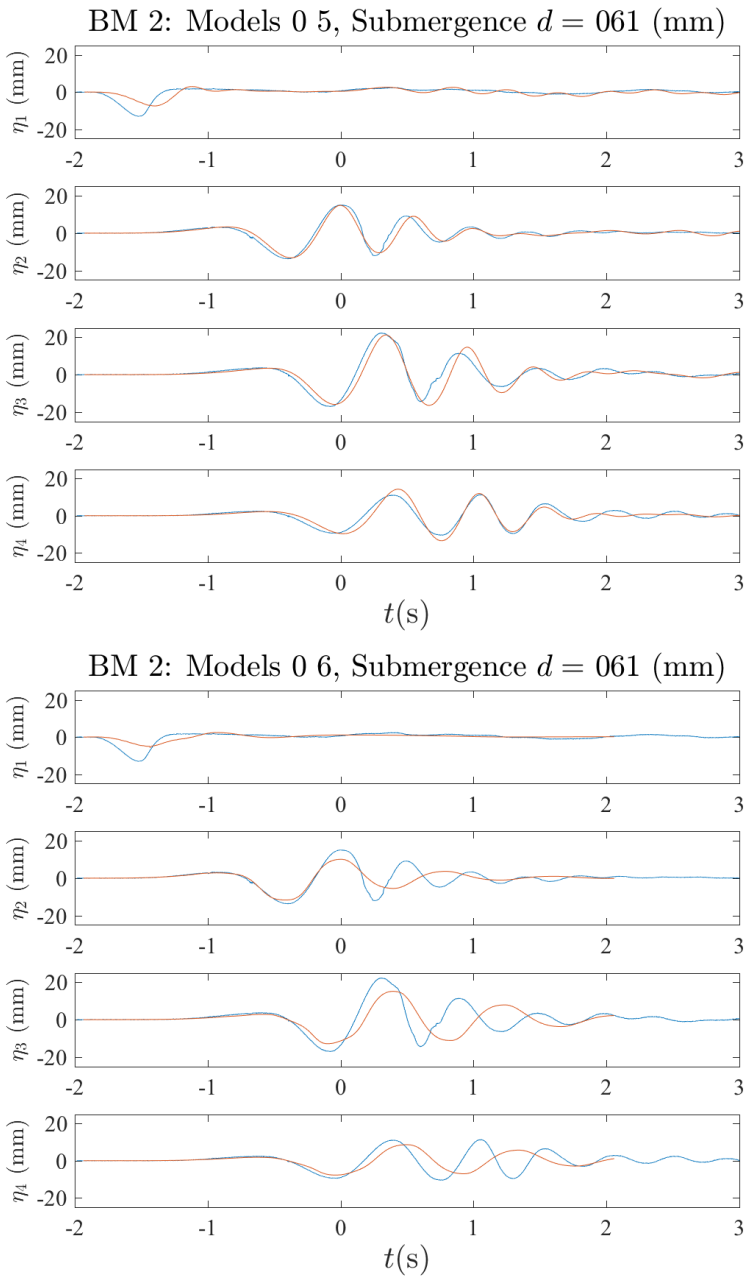

Figure 62: Benchmark 2: $d = 61$ mm. Models 5, 6. Observed and simulated water surface displacements.

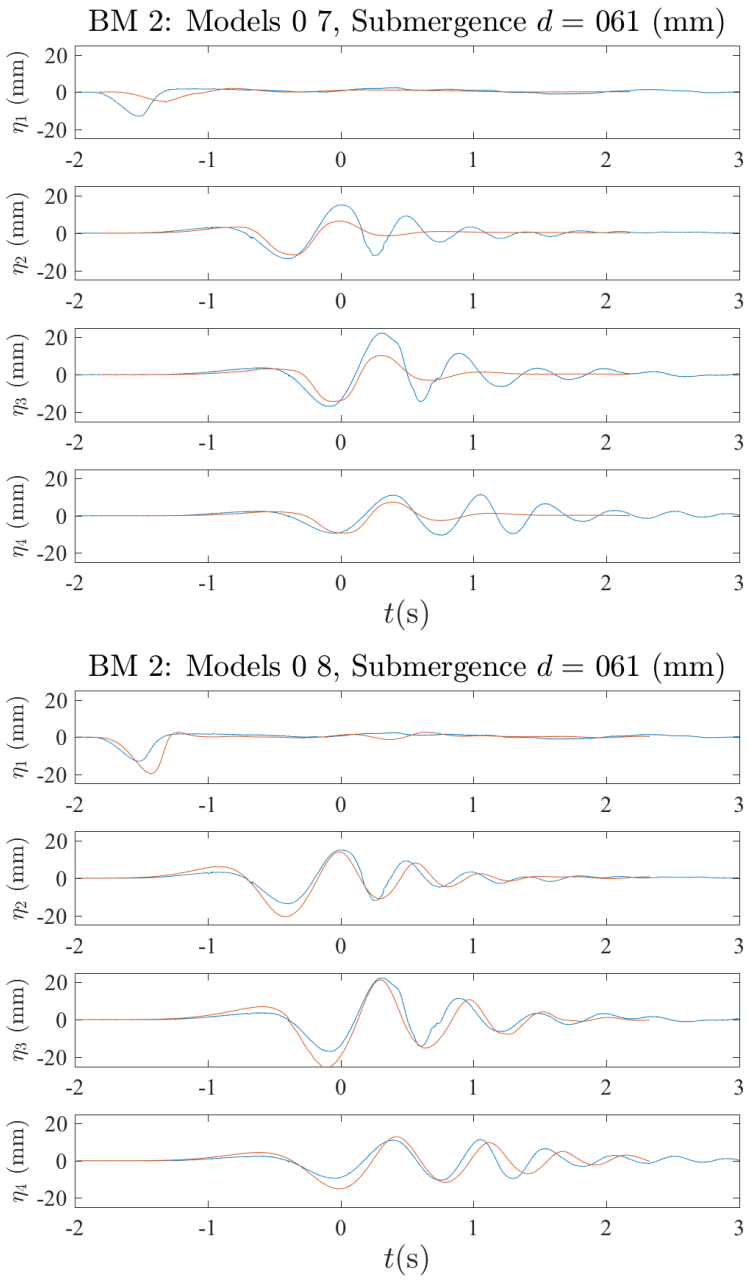

Figure 63: Benchmark 2: $d = 61$ mm. Models 7, 8. Observed and simulated water surface displacements.

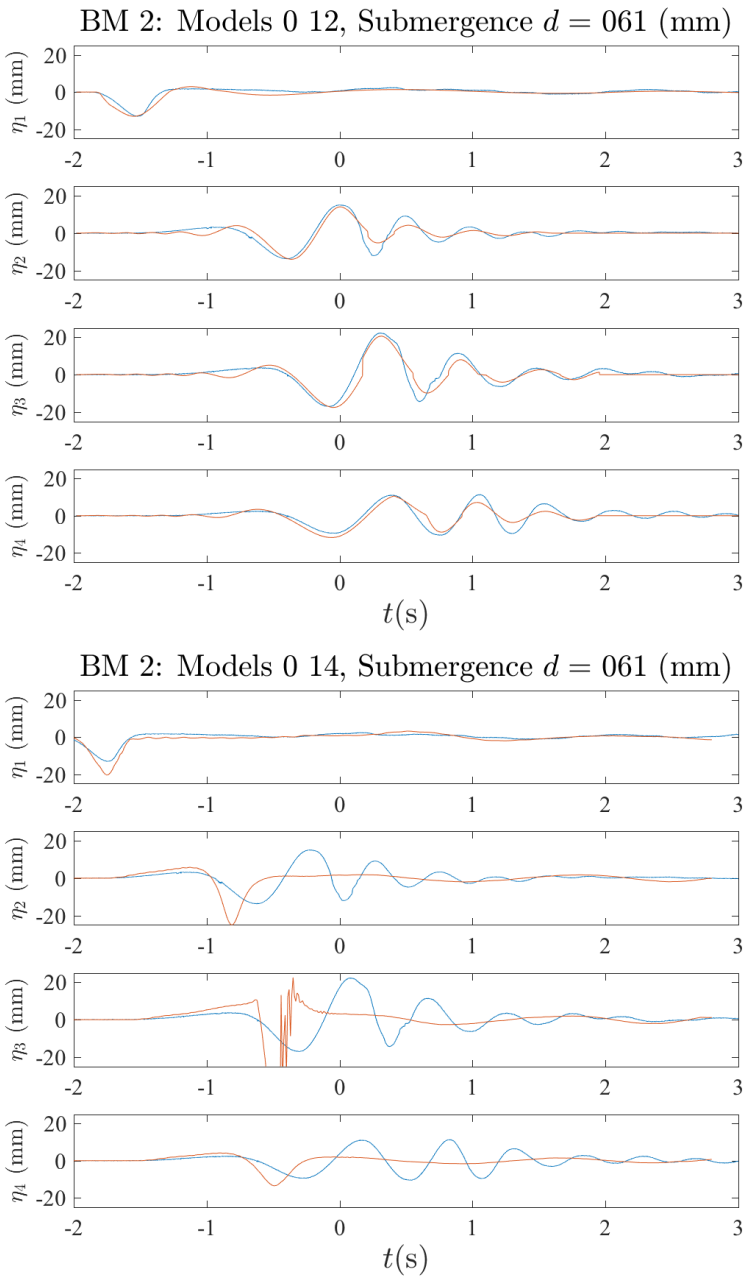

Figure 64: Benchmark 2: $d = 61$ mm. Models 12, 14. Observed and simulated water surface displacements.

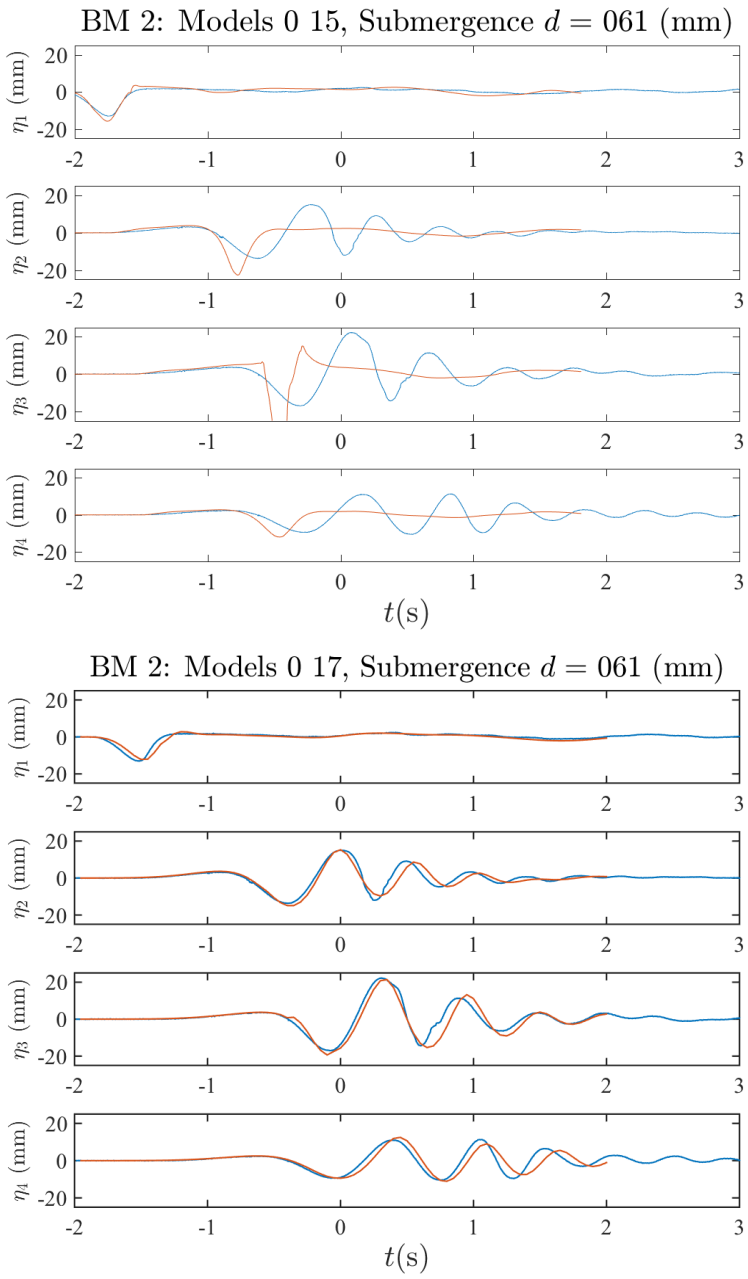

Figure 65: Benchmark 2: $d = 61$ mm. Models 15, 17. Observed and simulated water surface displacements.

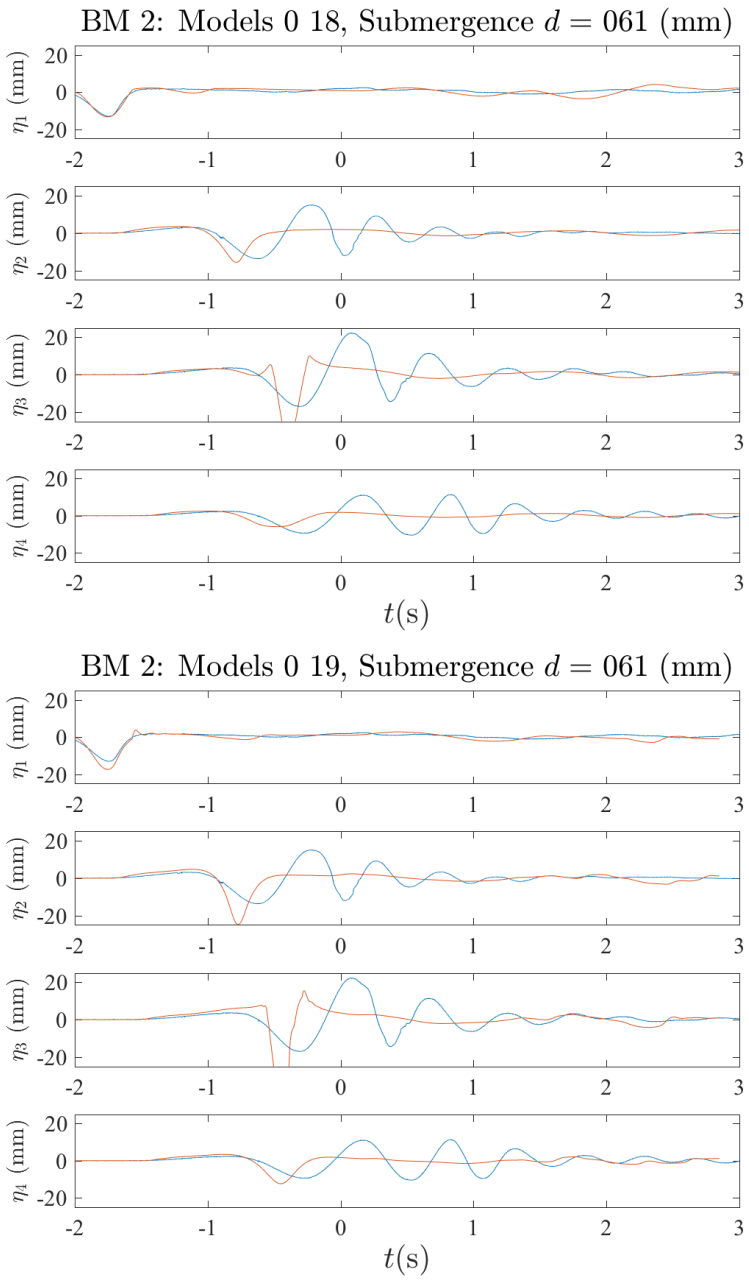

Figure 66: Benchmark 2: $d = 61$ mm. Models 18, 29. Observed and simulated water surface displacements.

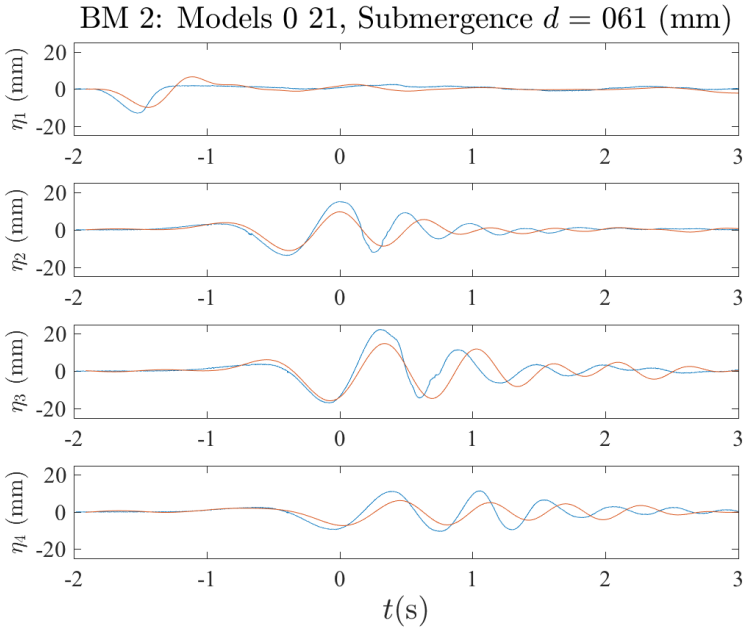

Figure 67: Benchmark 2: $d = 61$ mm. Model 21. Observed and simulated water surface displacements.

B Model simulation results: Benchmark 2, $d = 120$ mm

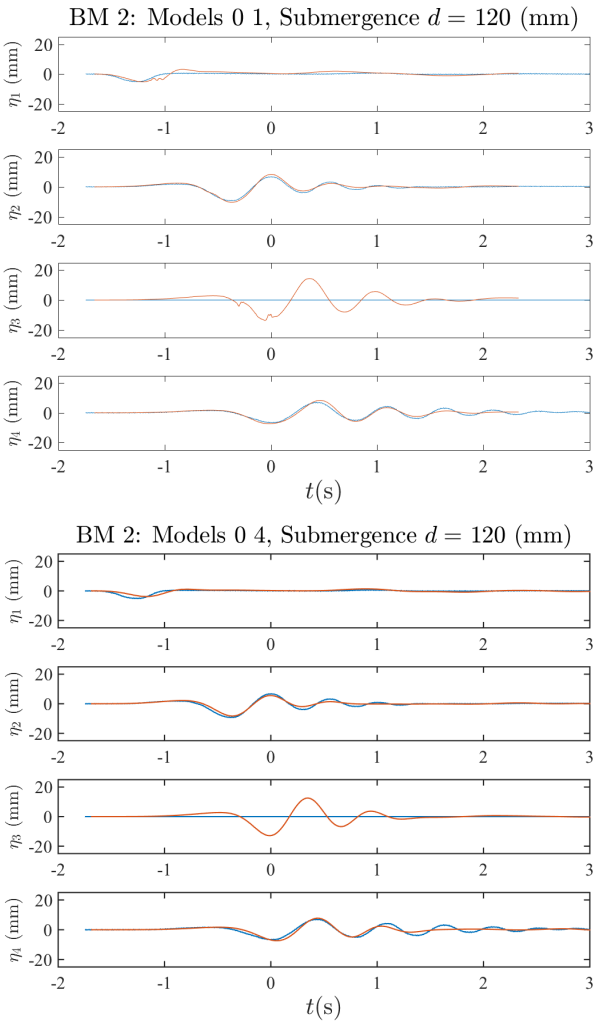

Figure 68: Benchmark 2: $d = 120$ mm. Models 1, 4. Observed and simulated water surface displacements.

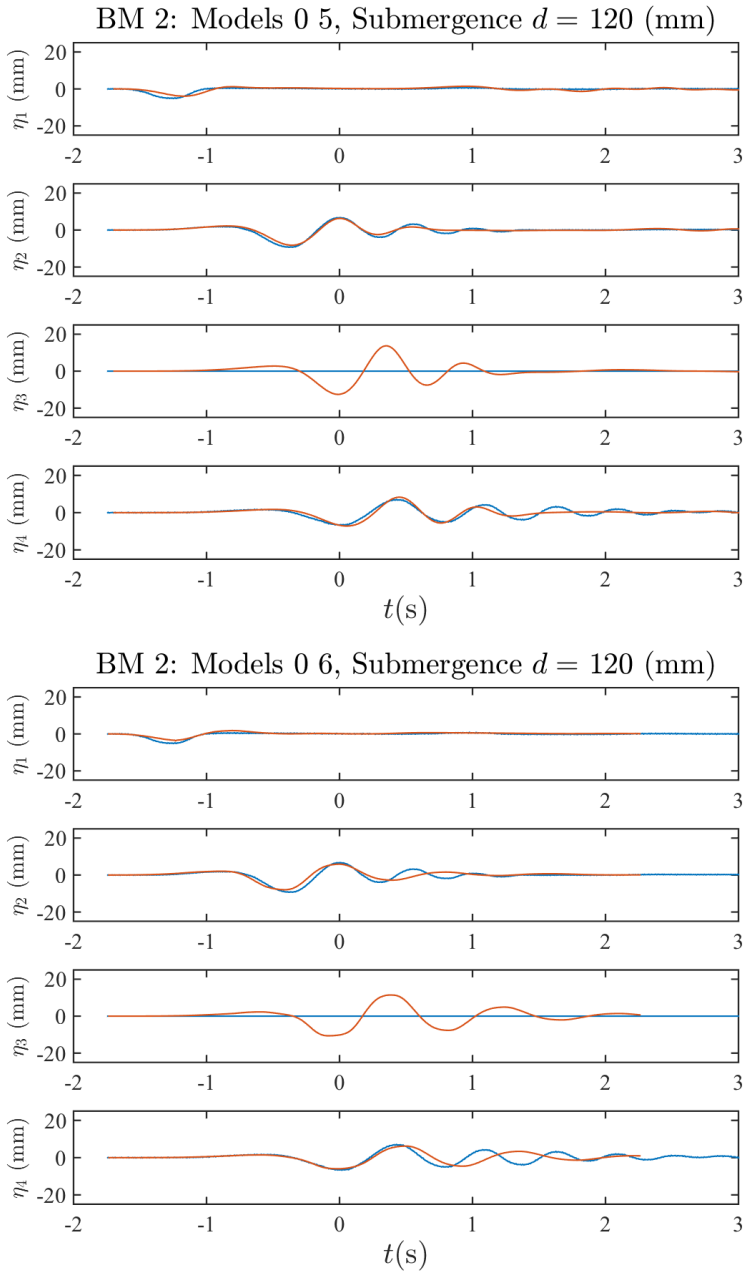

Figure 69: Benchmark 2: $d = 120$ mm. Models 5, 6. Observed and simulated water surface displacements.

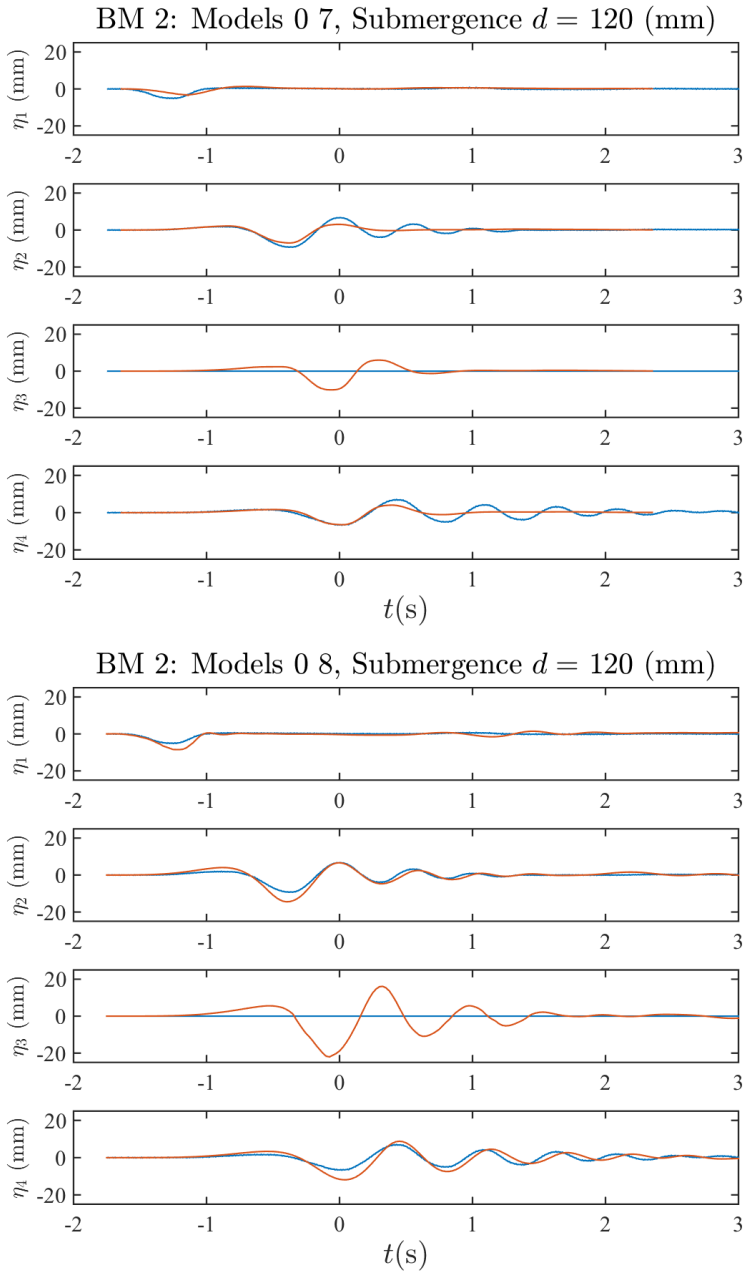

Figure 70: Benchmark 2: $d = 120$ mm. Models 7, 8. Observed and simulated water surface displacements.

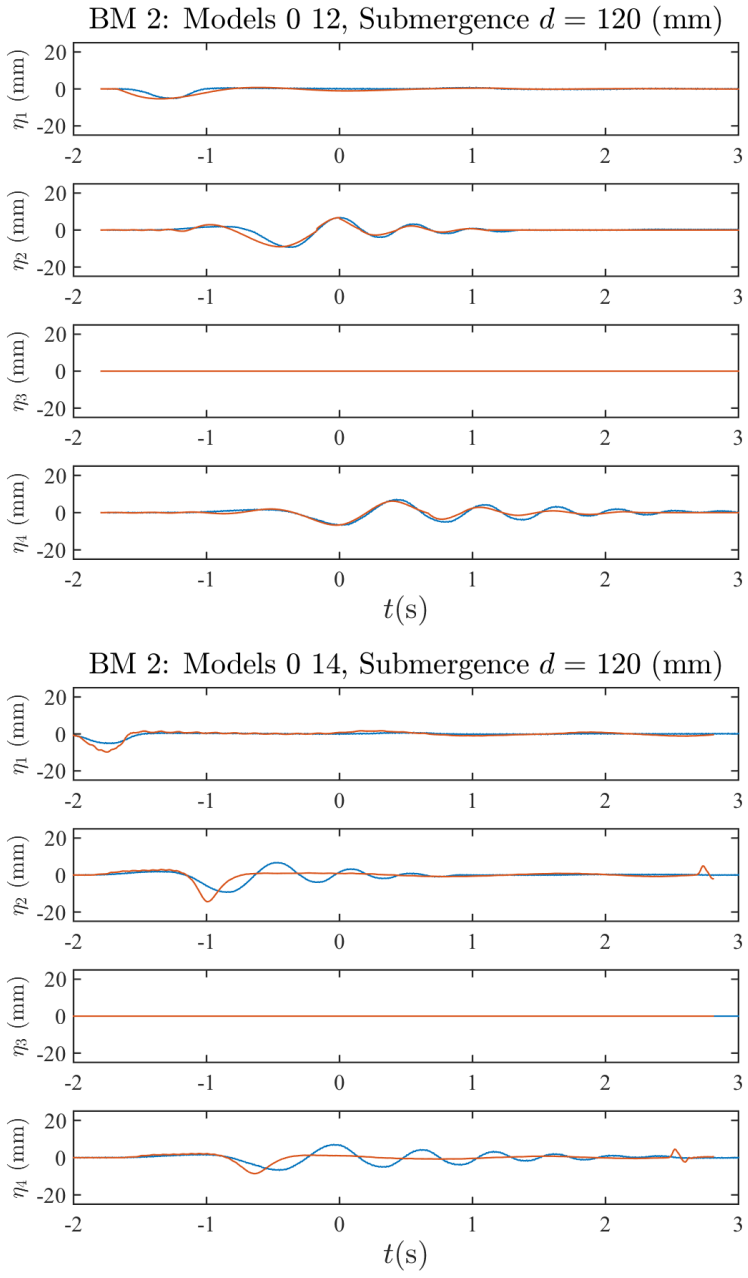

Figure 71: Benchmark 2: $d = 120$ mm. Models 12, 14. Observed and simulated water surface displacements.

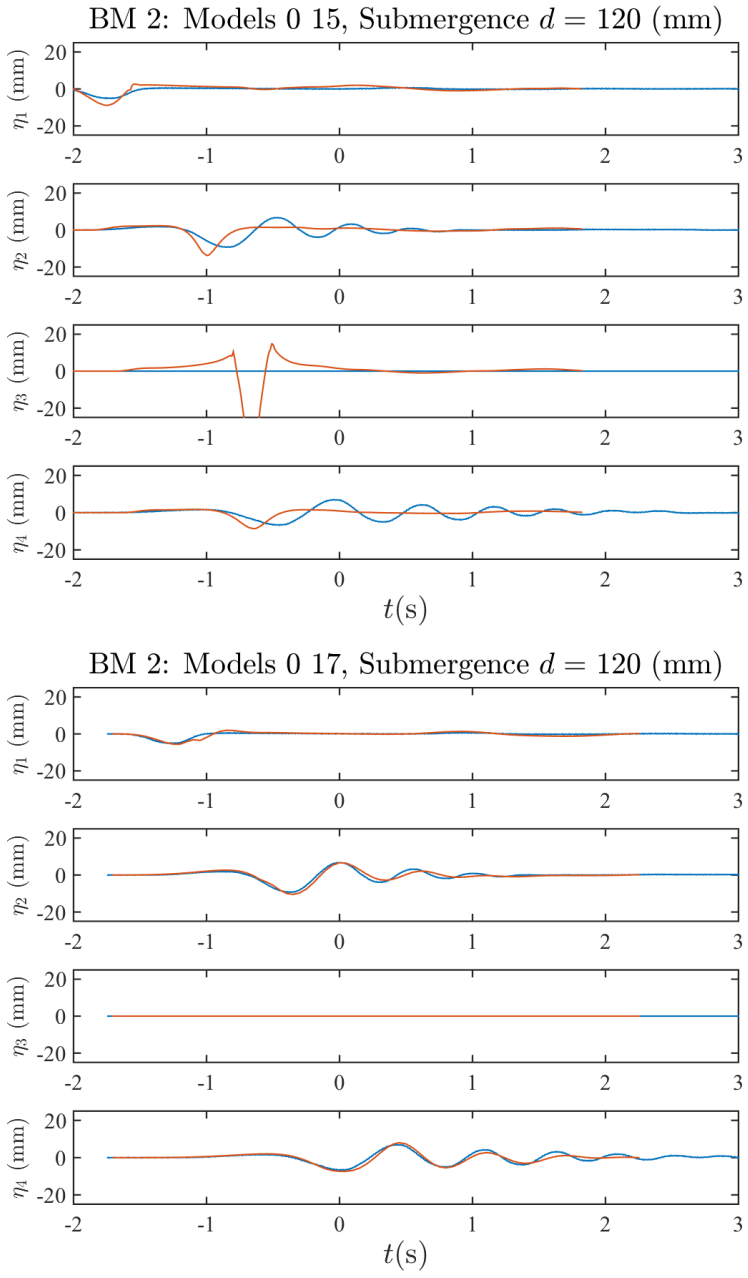

Figure 72: Benchmark 2: $d = 120$ mm. Models 15, 17. Observed and simulated water surface displacements.

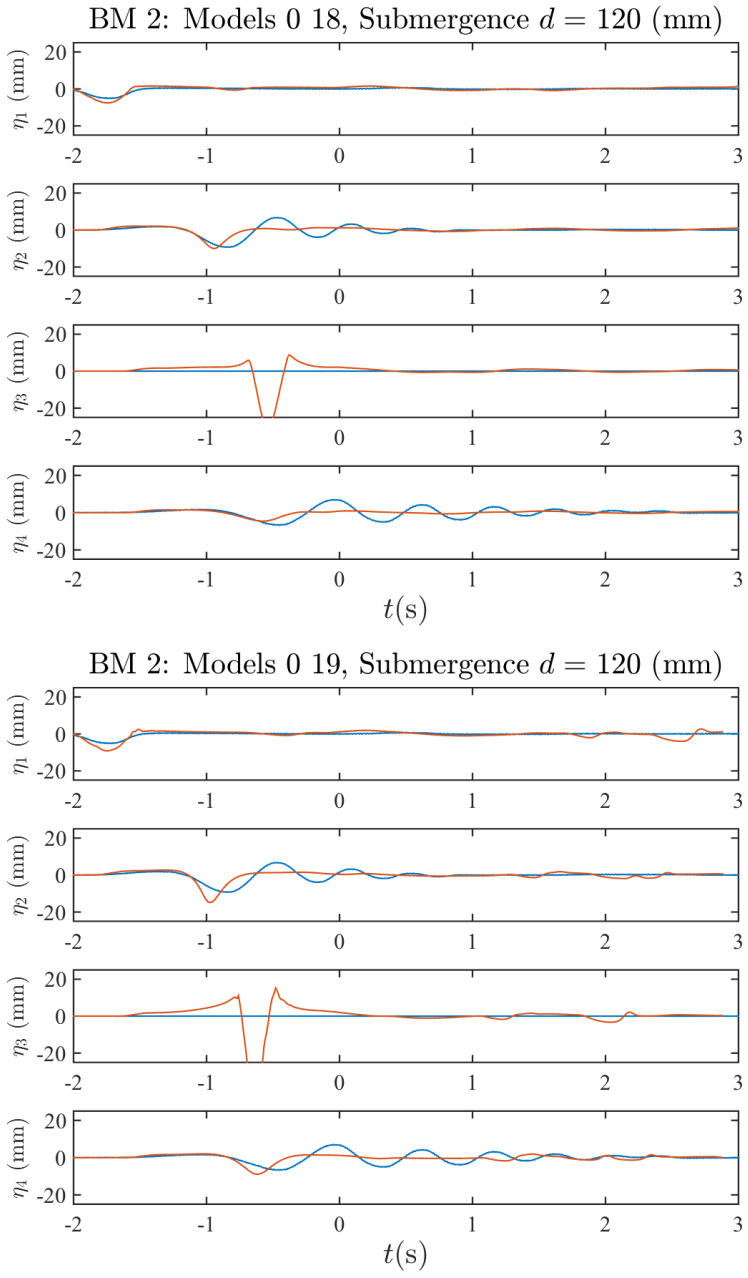

Figure 73: Benchmark 2: $d = 120$ mm. Models 18, 19. Observed and simulated water surface displacements.

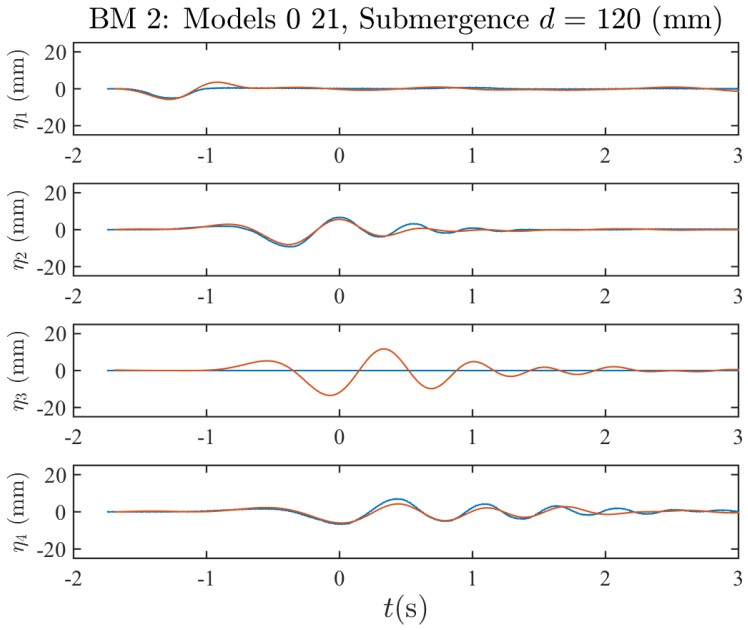

Figure 74: Benchmark 2: $d = 120$ mm. Model 21. Observed and simulated water surface displacements.

C Model simulation results: Benchmark 4 (Test 17)

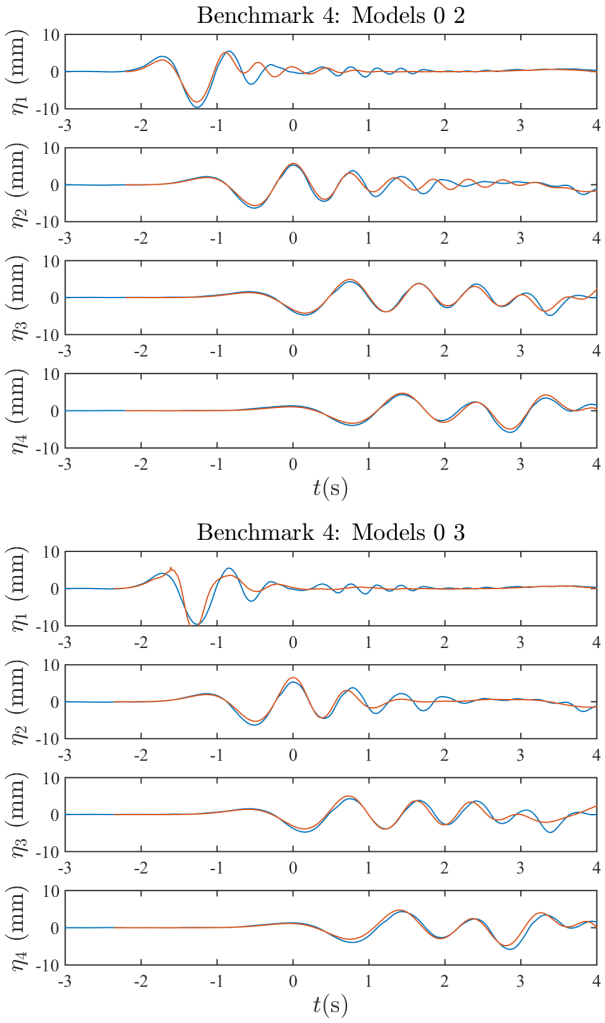

Figure 75: Benchmark 4. Models 2, 3. Observed and simulated water surface displacements.

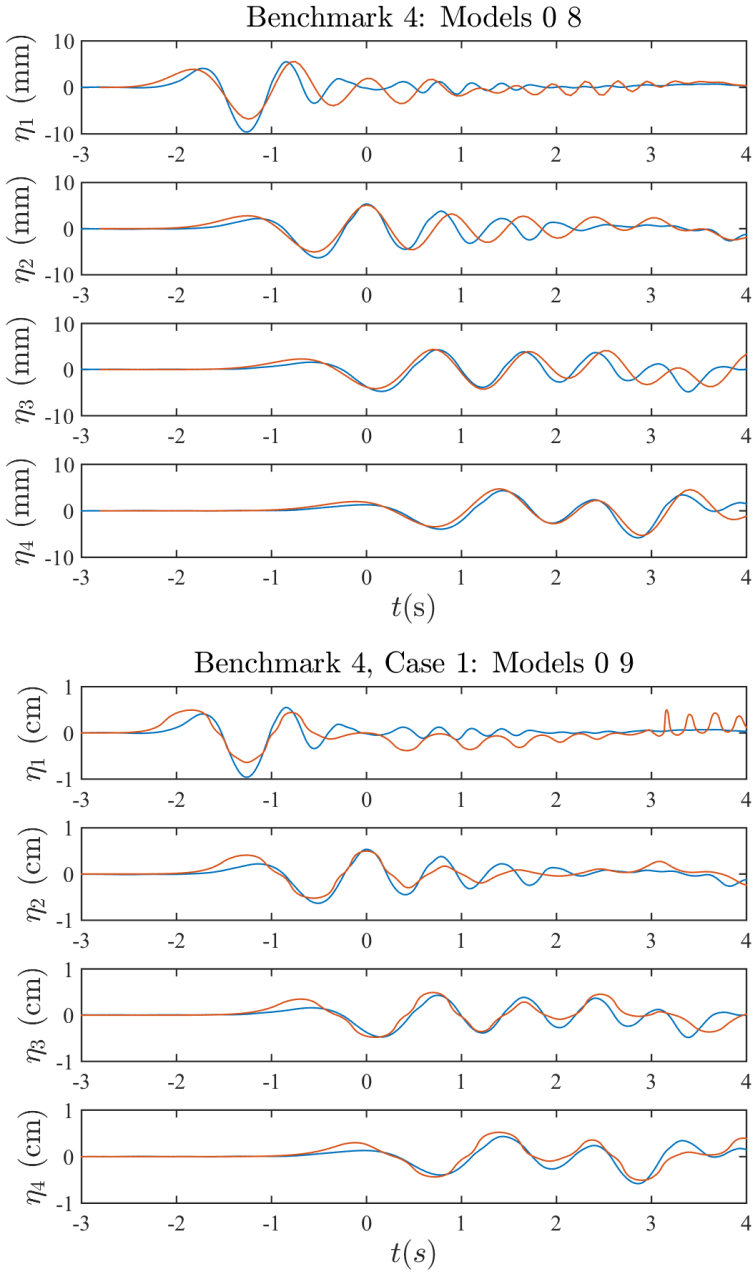

Figure 76: Benchmark 4. Models 8, 9. Observed and simulated water surface displacements.

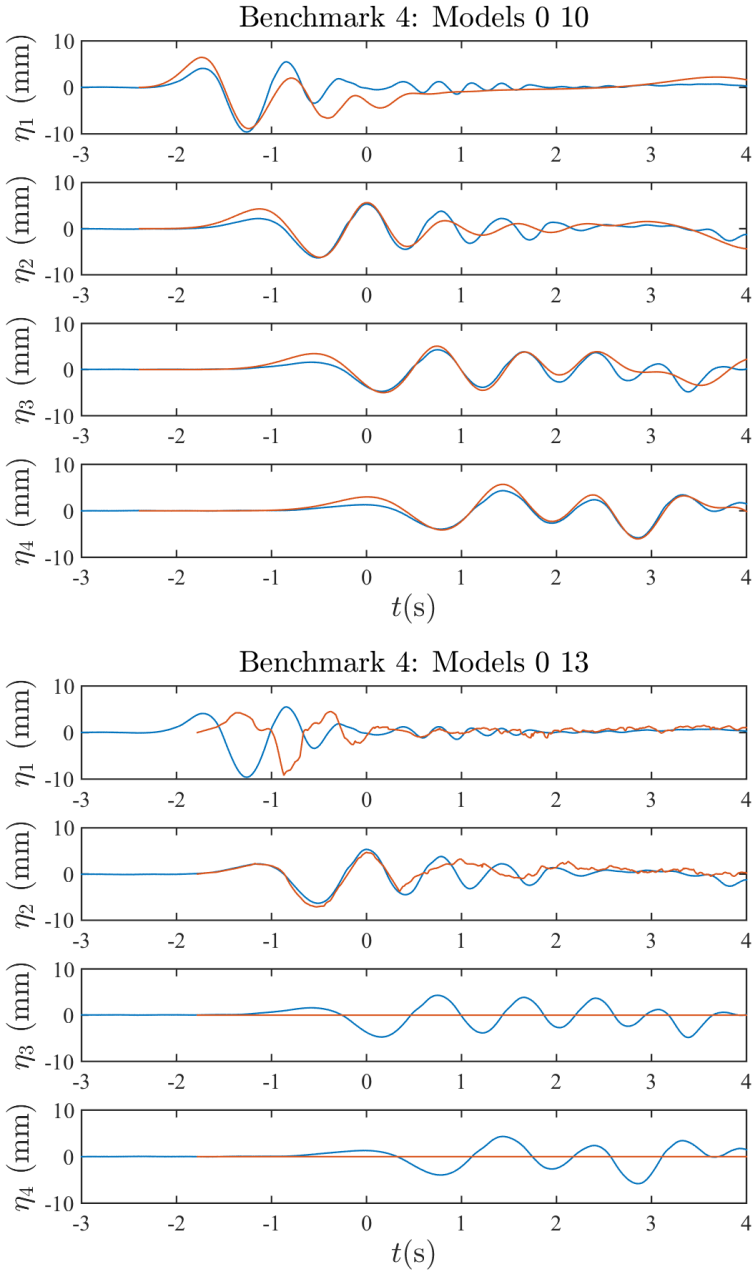

Figure 77: Benchmark 4. Models 10, 13. Observed and simulated water surface displacements.

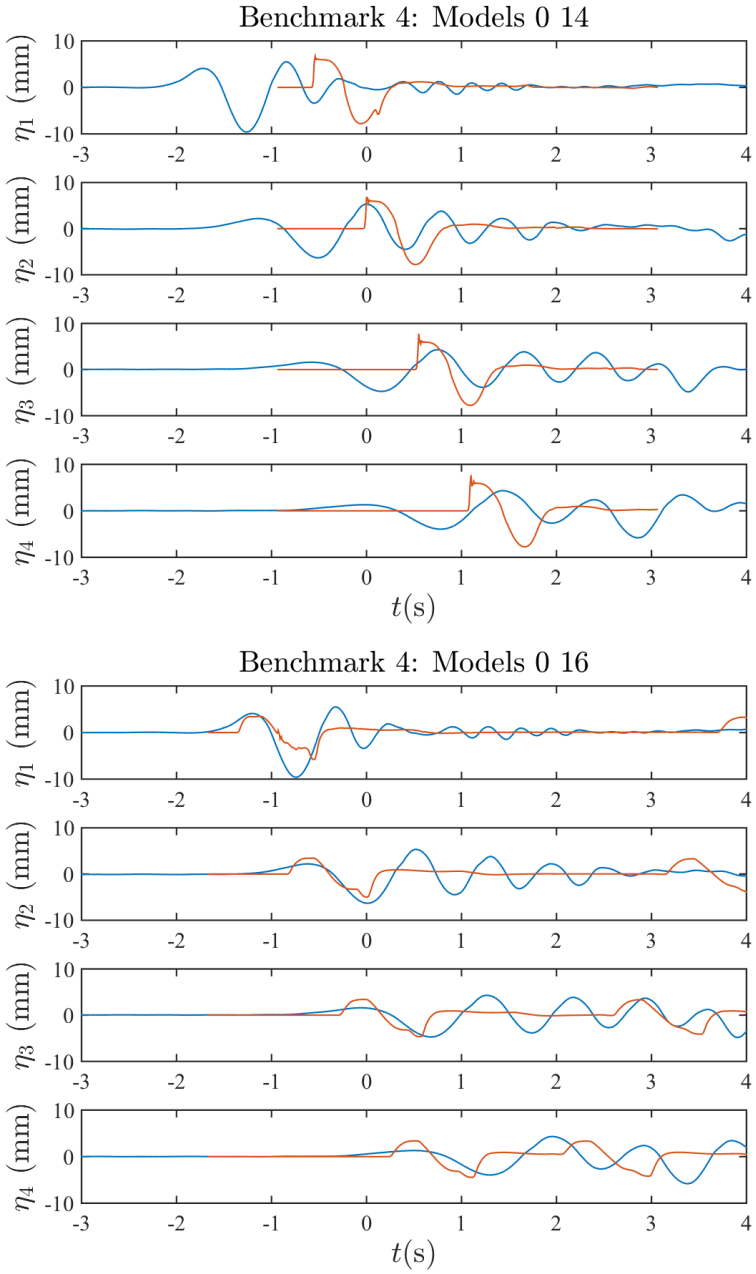

Figure 78: Benchmark 4. Models 14, 16. Observed and simulated water surface displacements.

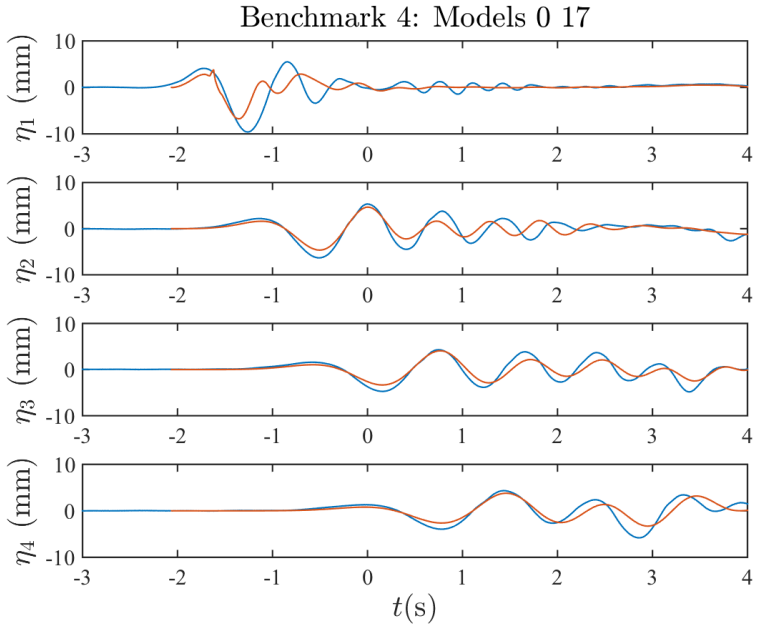

Figure 79: Benchmark 4. Model 17. Observed and simulated water surface displacements.

D Wavelet transform results: Benchmark 2, $d = 61$ mm.

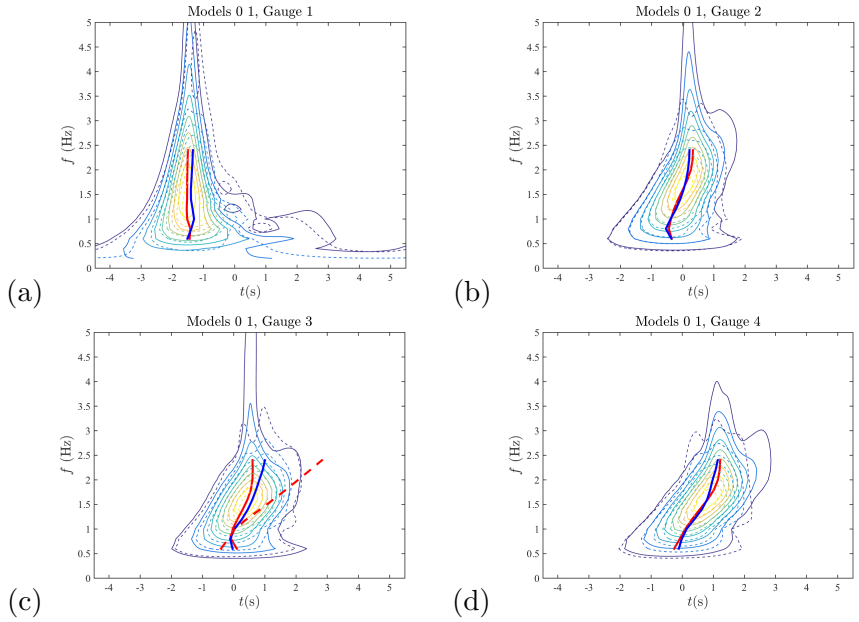

Figure 80: Wavelet transforms and arrival times for Benchmark 2, Model 1 (NHWAVE. solid slide, non-hydrostatic).

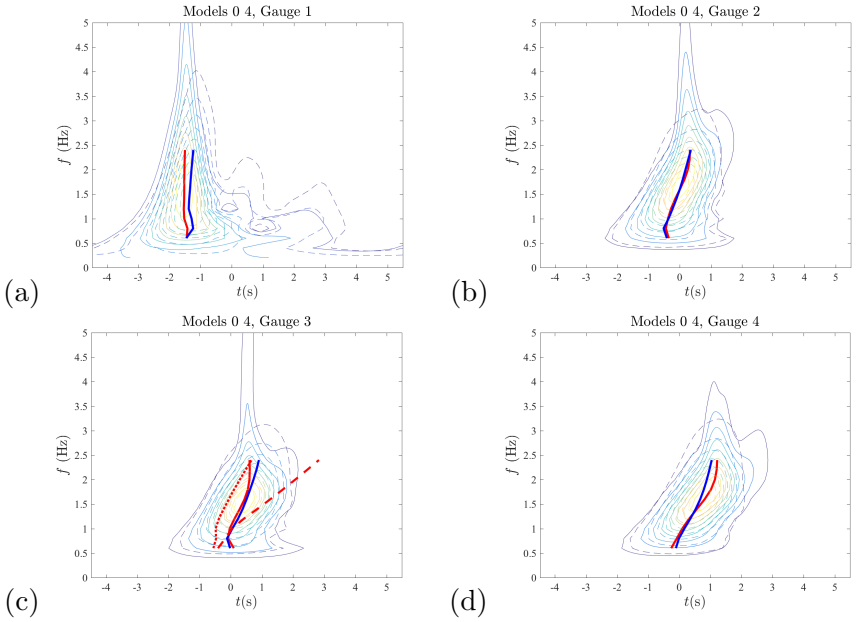

Figure 81: Wavelet transforms and arrival times for Benchmark 2, Model 4 (GloBouss. solid slide, Boussinesq, linear).

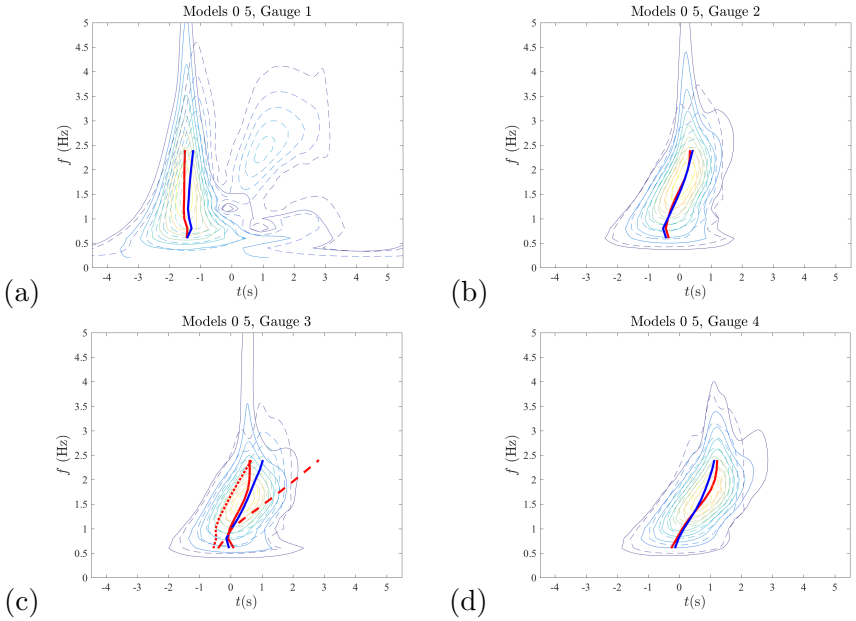

Figure 82: Wavelet transforms and arrival times for Benchmark 2, Model 5 (Globouss. solid slide, Boussinesq).

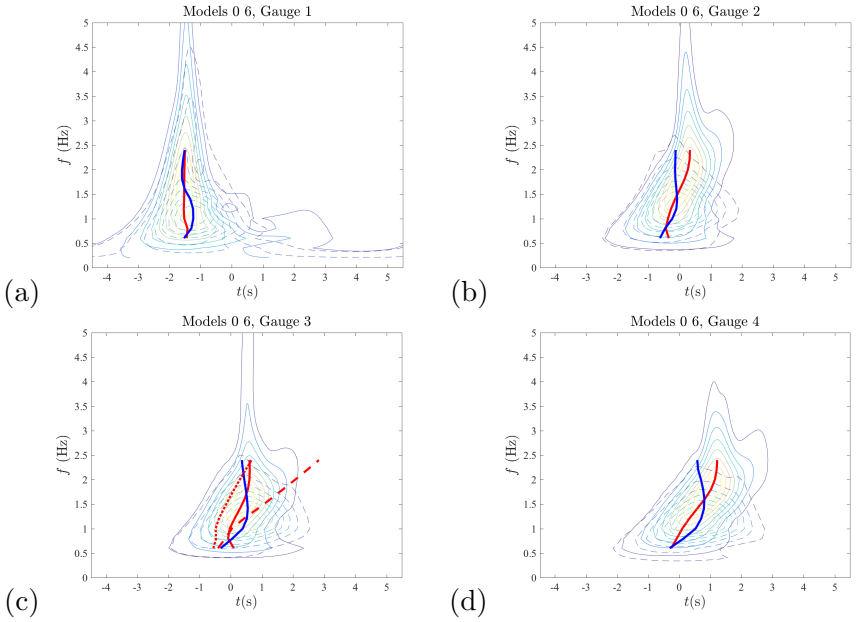

Figure 83: Wavelet transforms and arrival times for Benchmark 2, Model 6 (BoussCLAW. solid slide, Boussinesq, Peregrine dispersion).

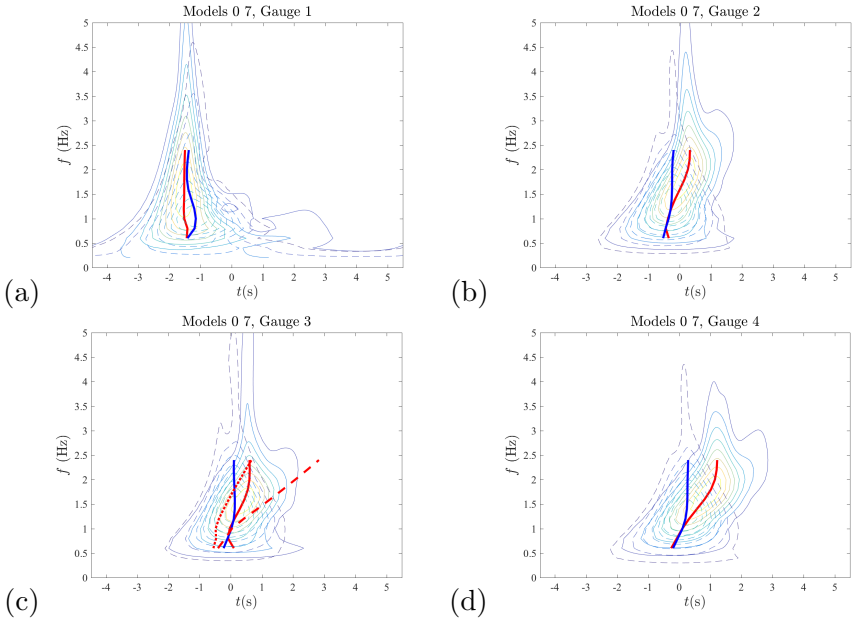

Figure 84: Wavelet transforms and arrival times for Benchmark 2, Model 7 (BoussCLAW. solid slide, Boussinesq, Nwogu dispersion).

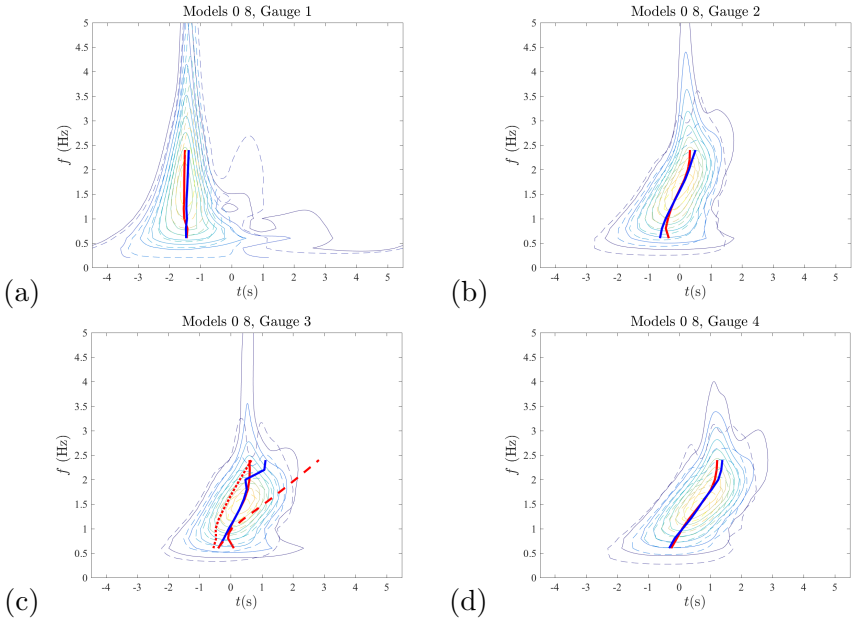

Figure 85: Wavelet transforms and arrival times for Benchmark 2, Model 8 (Tsunami3D. Viscous slide, Navier-Stokes).

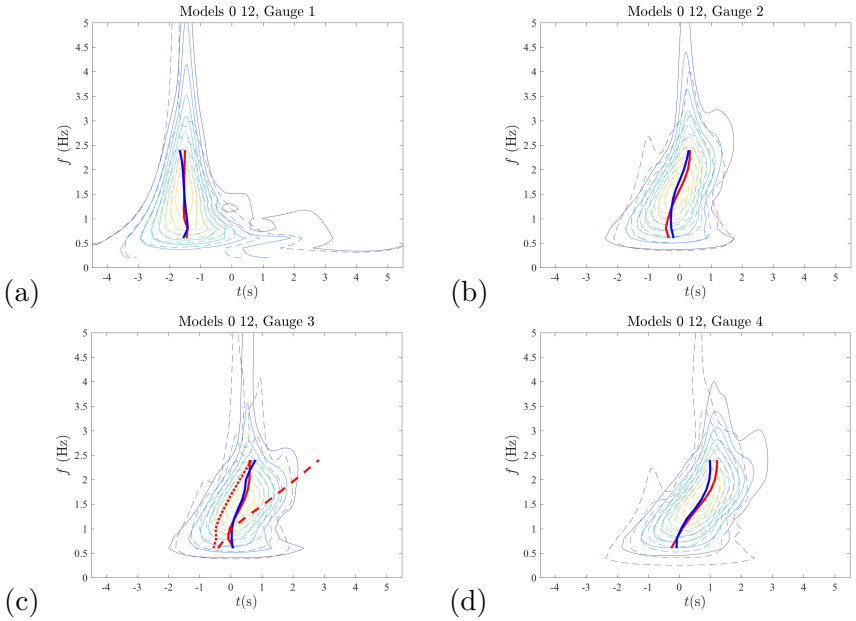

Figure 86: Wavelet transforms and arrival times for Benchmark 2, Model 12 (LS3D. solid slide, Boussinesq).

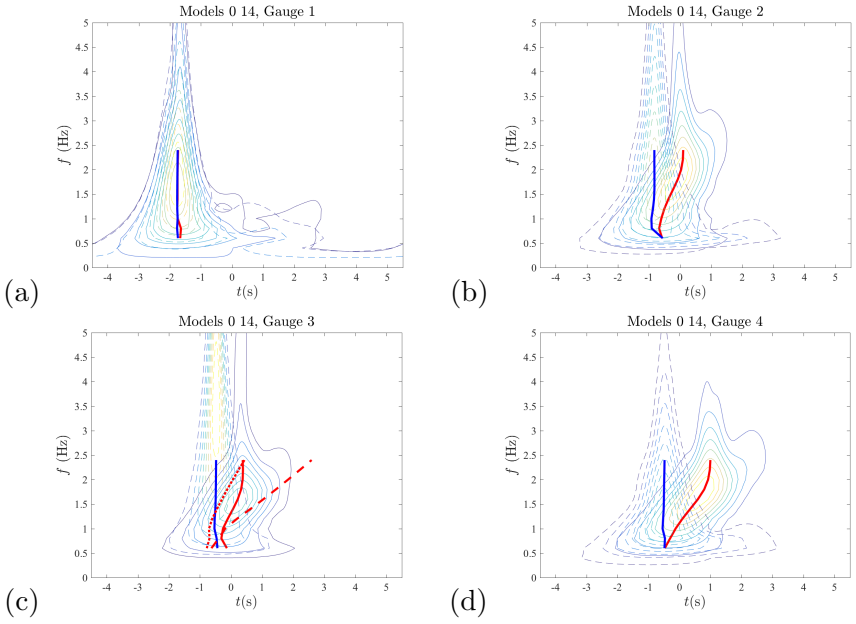

Figure 87: Wavelet transforms and arrival times for Benchmark 2, Model 14 (Alaska GI-L. Viscous slide, hydrostatic).

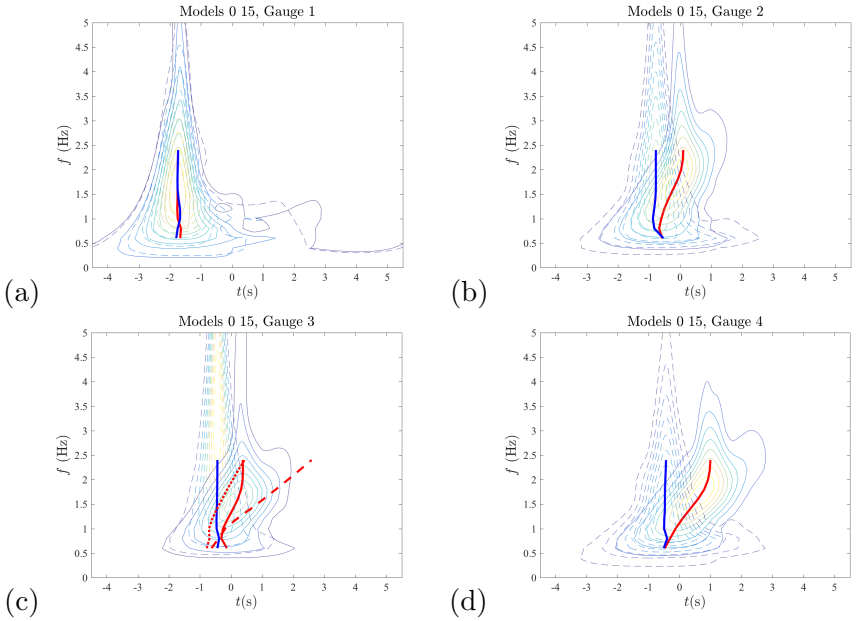

Figure 88: Wavelet transforms and arrival times for Benchmark 2, Model 15 (NHWAVE. solid slide, hydrostatic).

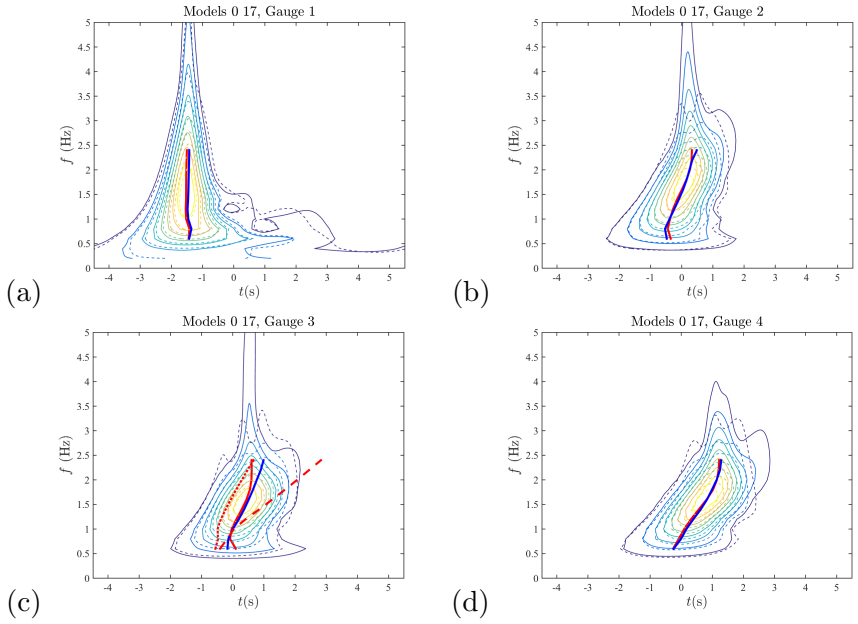

Figure 89: Wavelet transforms and arrival times for Benchmark 2, Model 17 (Landslide-HYSEA. Granular slide, non-hydrostatic).

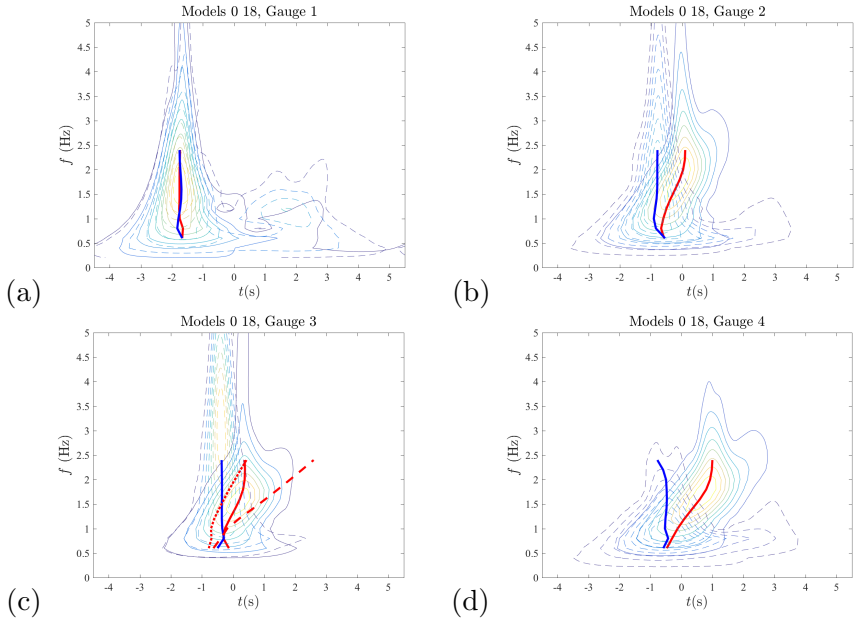

Figure 90: Wavelet transforms and arrival times for Benchmark 2, Model 18 (FBSlide. Solid slide, hydrostatic).

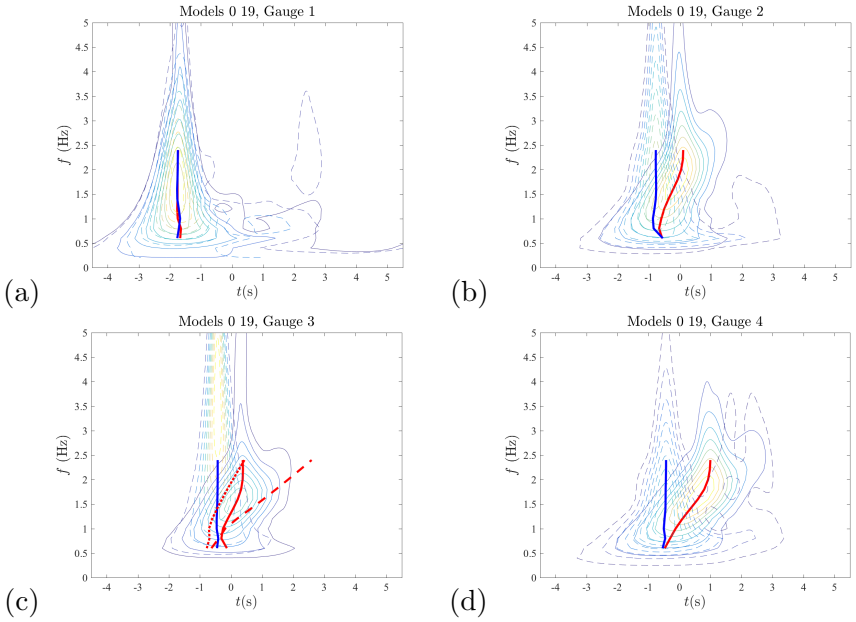

Figure 91: Wavelet transforms and arrival times for Benchmark 2, Model 19 (NLSW (Lynett). solid slide, hydrostatic).

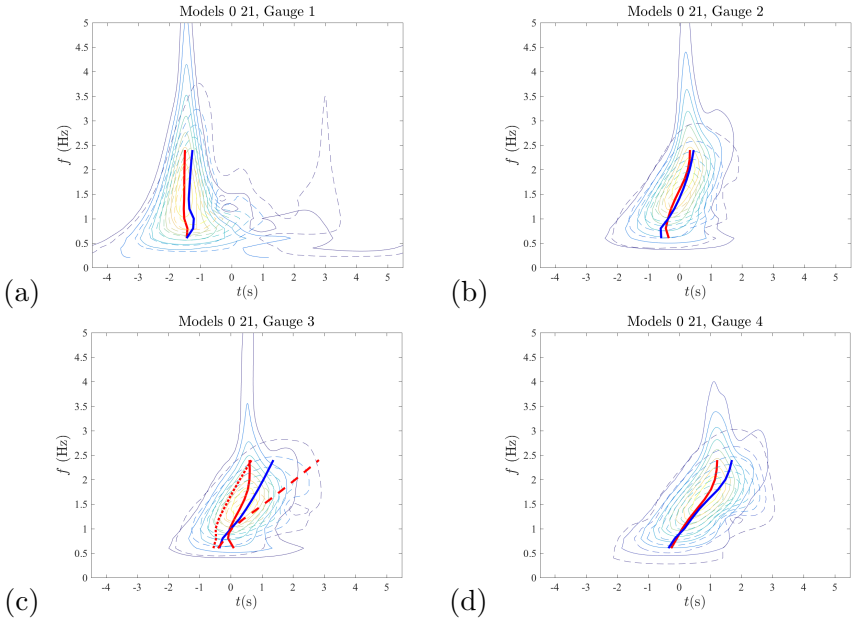

Figure 92: Wavelet transforms and arrival times for Benchmark 2, Model 21 (Mild slope equation Lynett). Solid slide, non-hydrostatic).

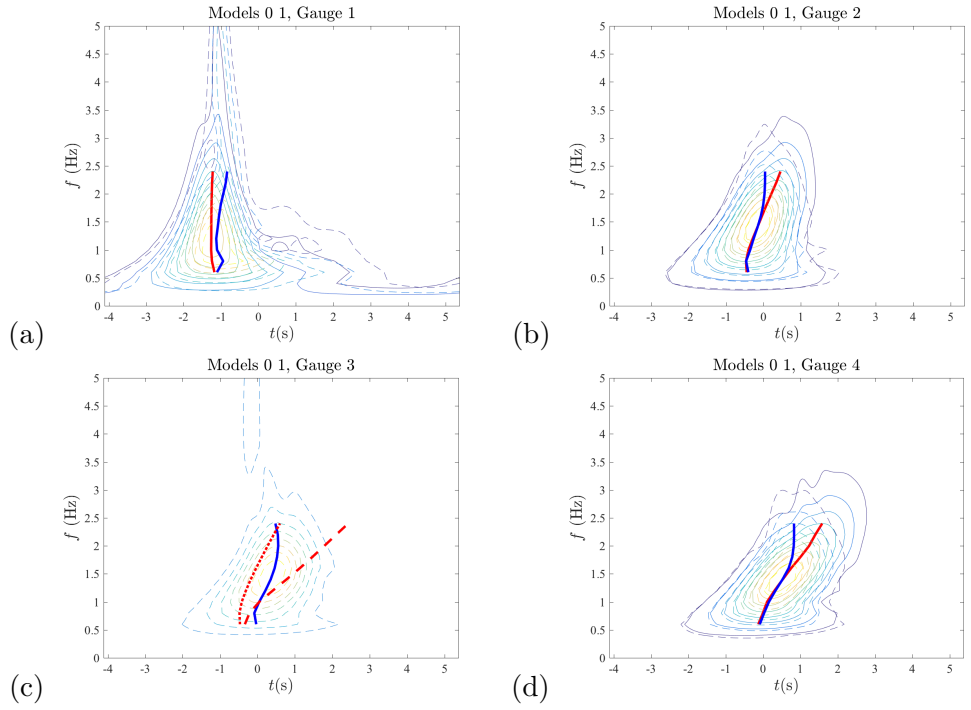

Figure 93: Wavelet transforms and arrival times for Benchmark 2, Model 1 (NHWAVE. solid slide, non-hydrostatic).

E Wavelet transform results: Benchmark 2, $d = 120$ mm.

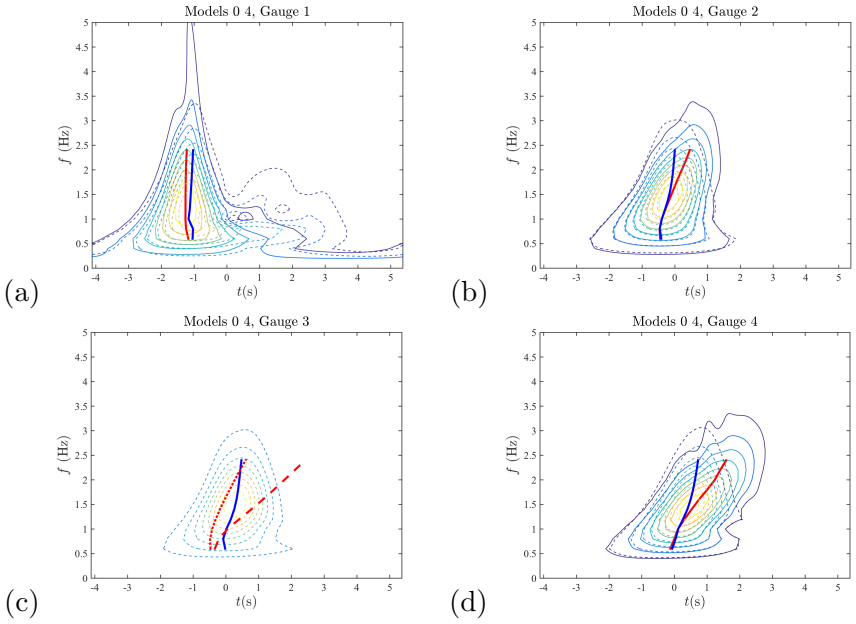

Figure 94: Wavelet transforms and arrival times for Benchmark 2, Model 4 (GloBouss. solid slide, Boussinesq, linear).

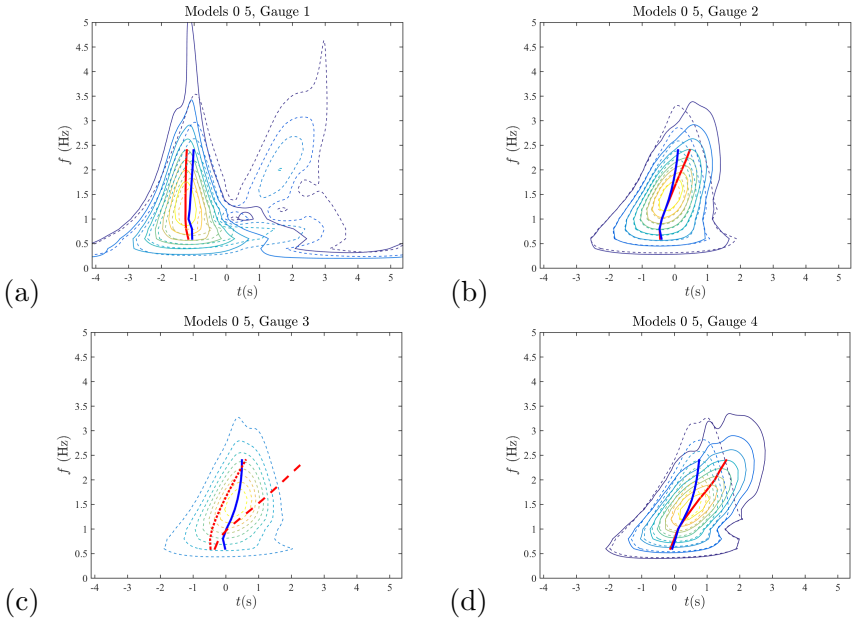

Figure 95: Wavelet transforms and arrival times for Benchmark 2, Model 5 (Globouss. solid slide, Boussinesq).

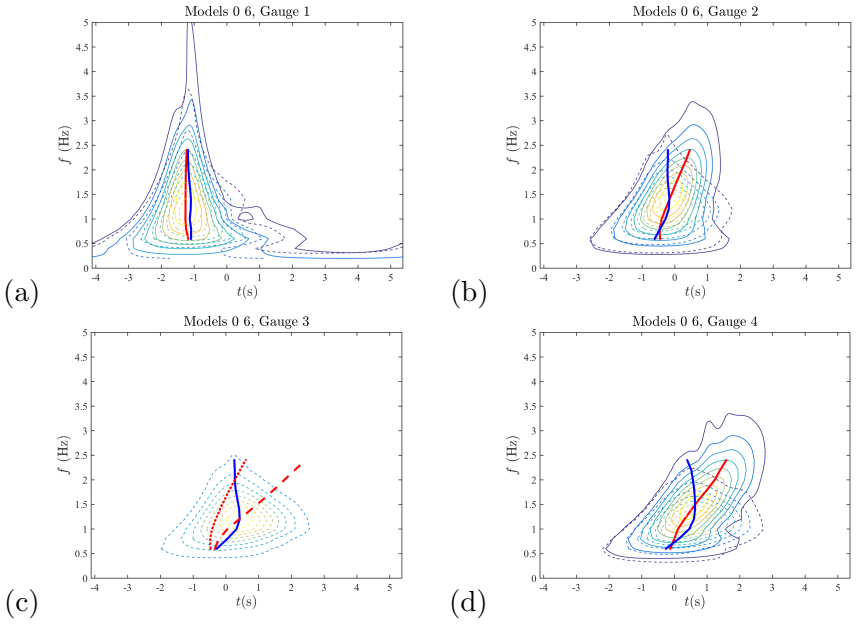

Figure 96: Wavelet transforms and arrival times for Benchmark 2, Model 6 (BoussCLAW. solid slide, Boussinesq, Peregrine dispersion).

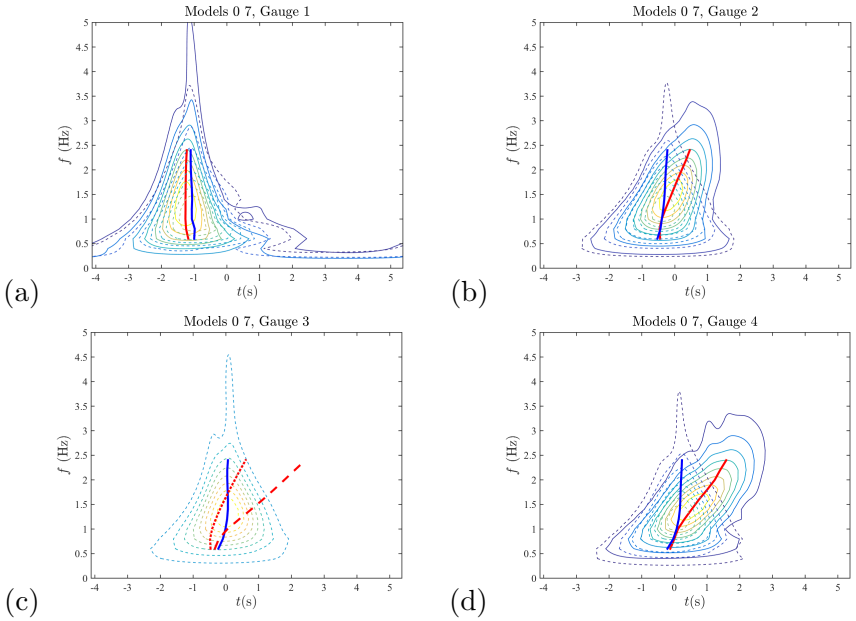

Figure 97: Wavelet transforms and arrival times for Benchmark 2, Model 7 (BoussCLAW. solid slide, Boussinesq, Nwogu dispersion).

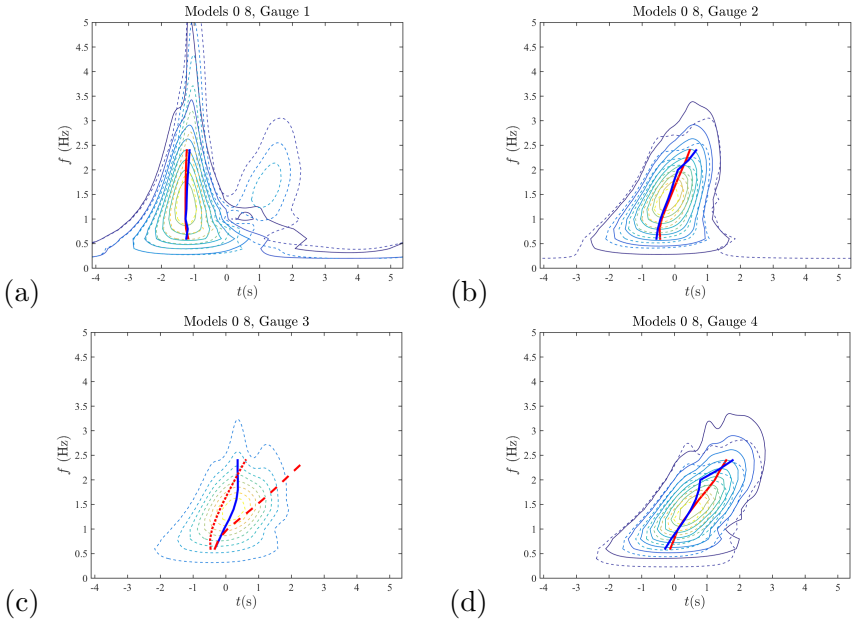

Figure 98: Wavelet transforms and arrival times for Benchmark 2, Model 8 (Tsunami3D. Viscous slide, Navier-Stokes).

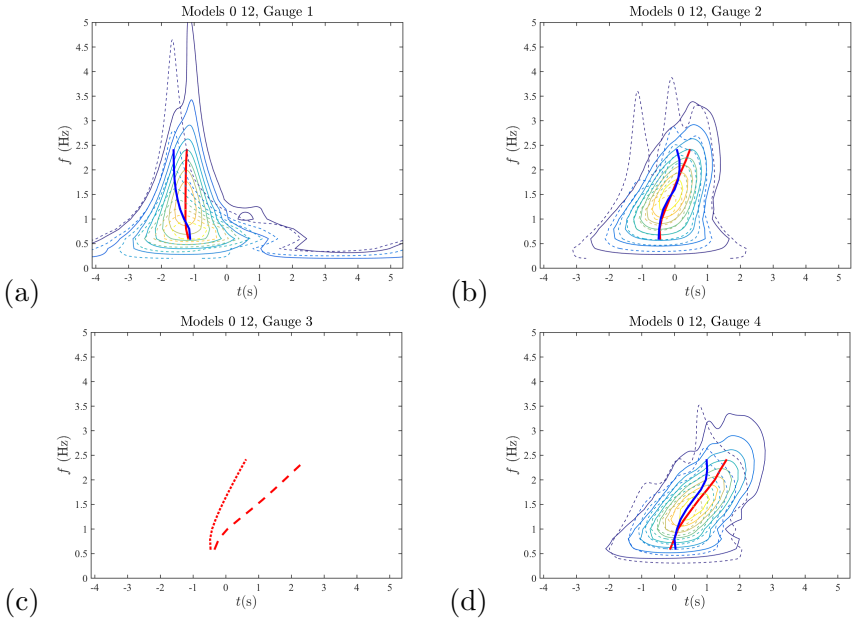

Figure 99: Wavelet transforms and arrival times for Benchmark 2, Model 12 (LS3D. solid slide, Boussinesq).

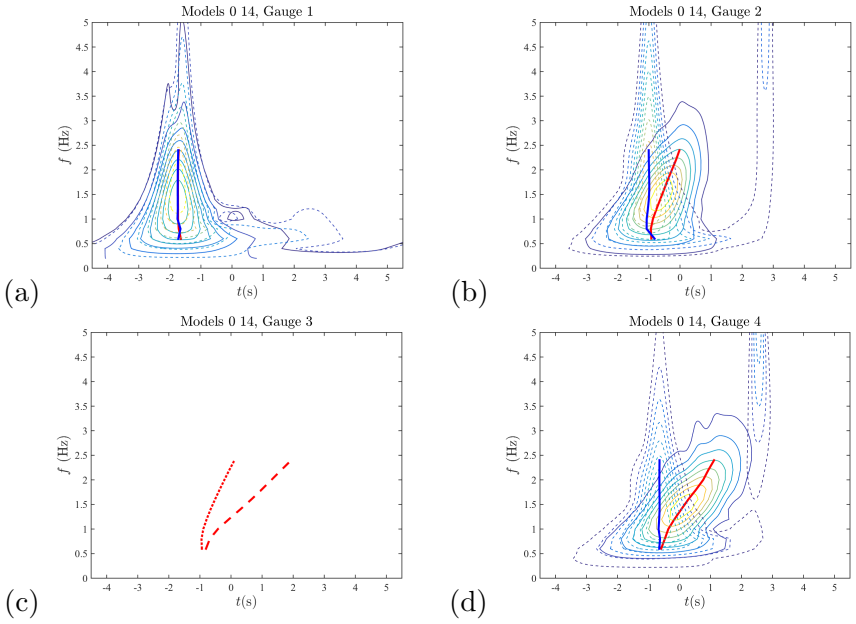

Figure 100: Wavelet transforms and arrival times for Benchmark 2, Model 14 (Alaska GI-L. Viscous slide, hydrostatic).

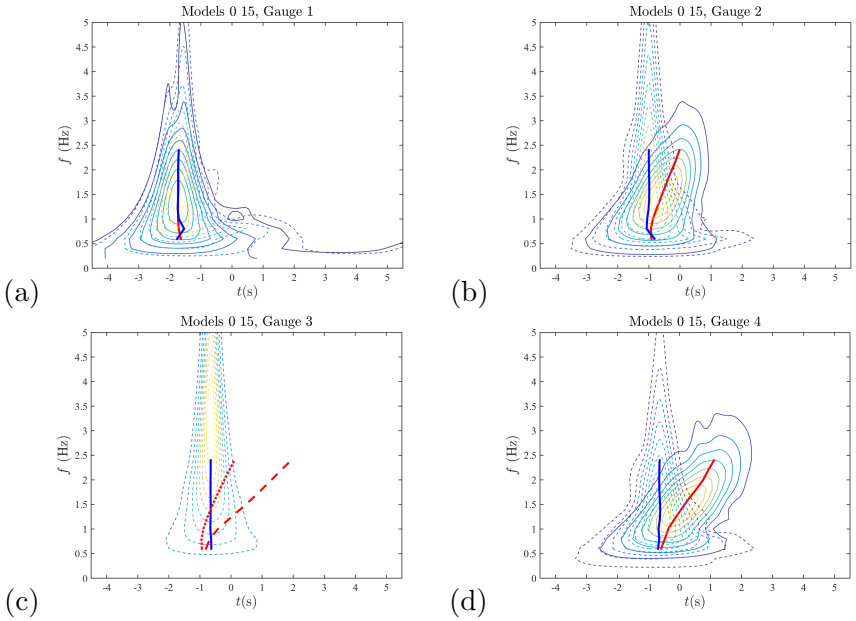

Figure 101: Wavelet transforms and arrival times for Benchmark 2, Model 15 (NHWAVE. solid slide, hydrostatic).

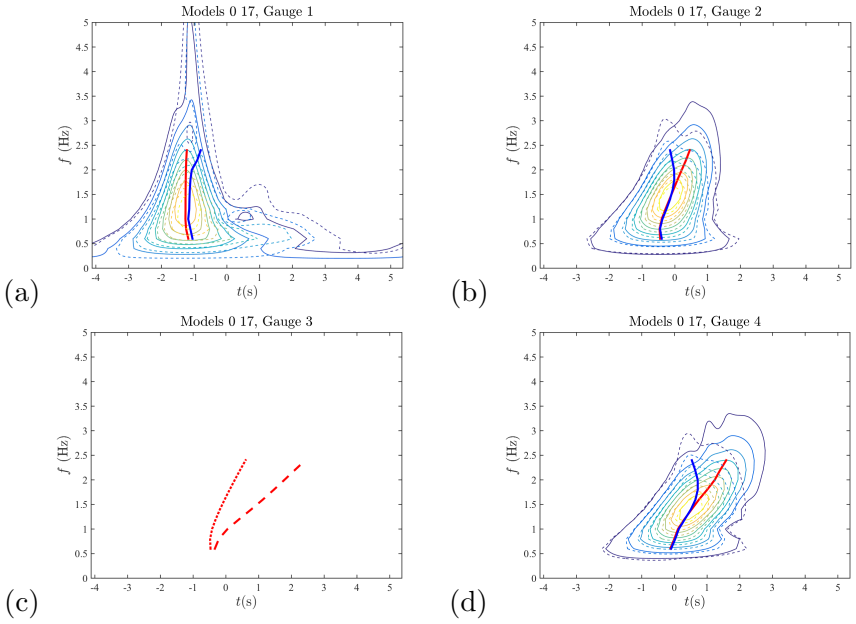

Figure 102: Wavelet transforms and arrival times for Benchmark 2, Model 17 (Landslide-HYSEA. Granular slide, non-hydrostatic).

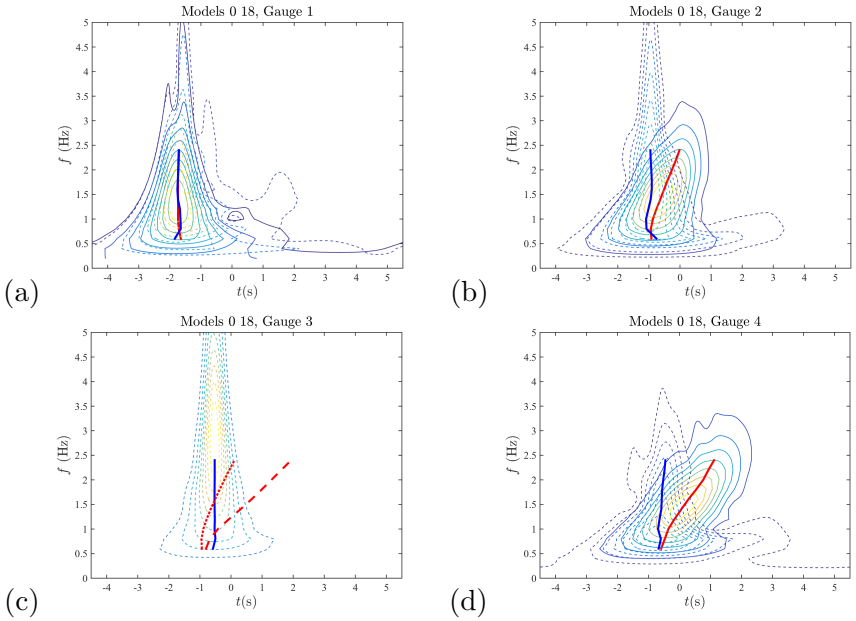

Figure 103: Wavelet transforms and arrival times for Benchmark 2, Model 18 (FBSlide. Solid slide, hydrostatic).

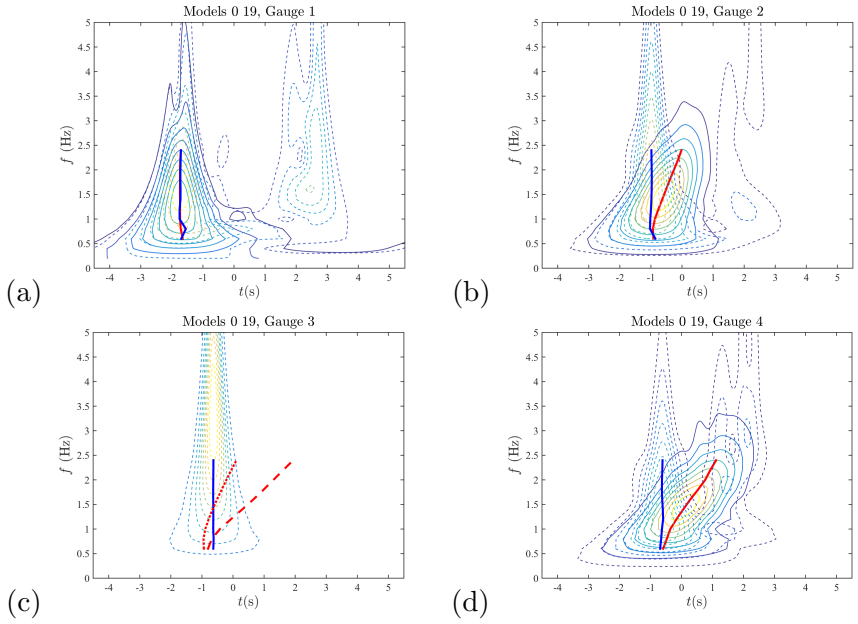

Figure 104: Wavelet transforms and arrival times for Benchmark 2, Model 19 (NLSW (Lynett). solid slide, hydrostatic).

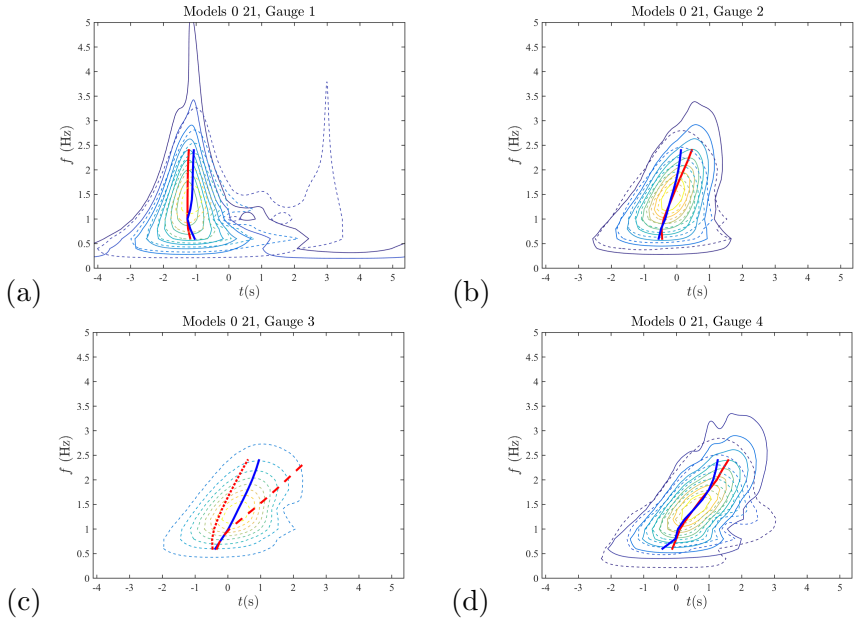

Figure 105: Wavelet transforms and arrival times for Benchmark 2, Model 21 (Mild slope equation Lynett). Solid slide, non-hydrostatic).

F Wavelet transform results: Benchmark 4.

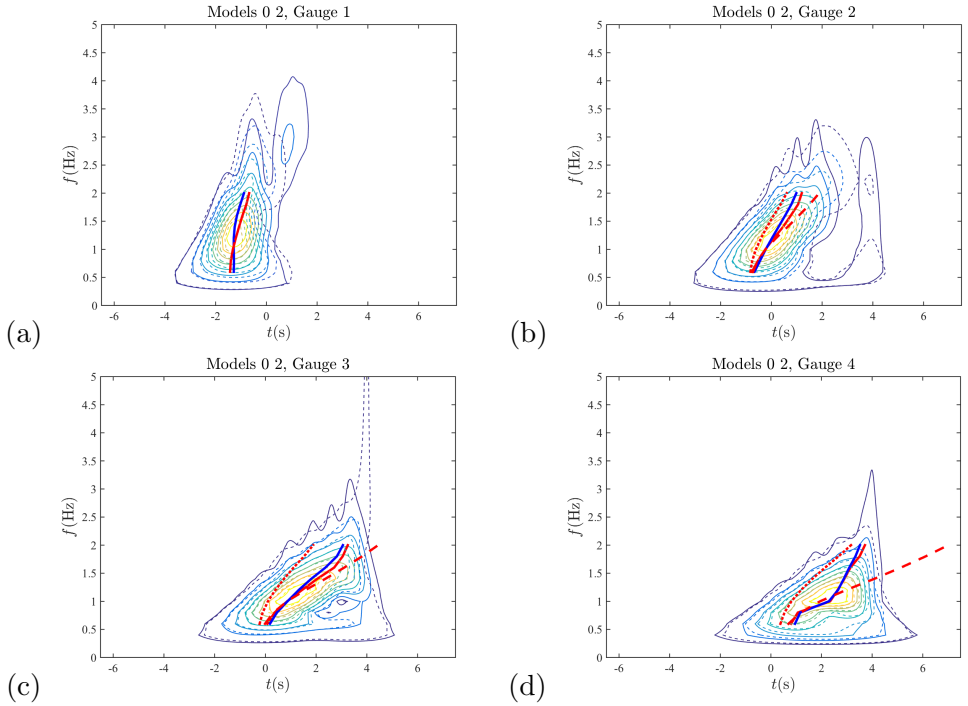

Figure 106: Wavelet transforms and arrival times for Benchmark 4, Model 2 (NHWAVE, viscous slide, non-hydrostatic).

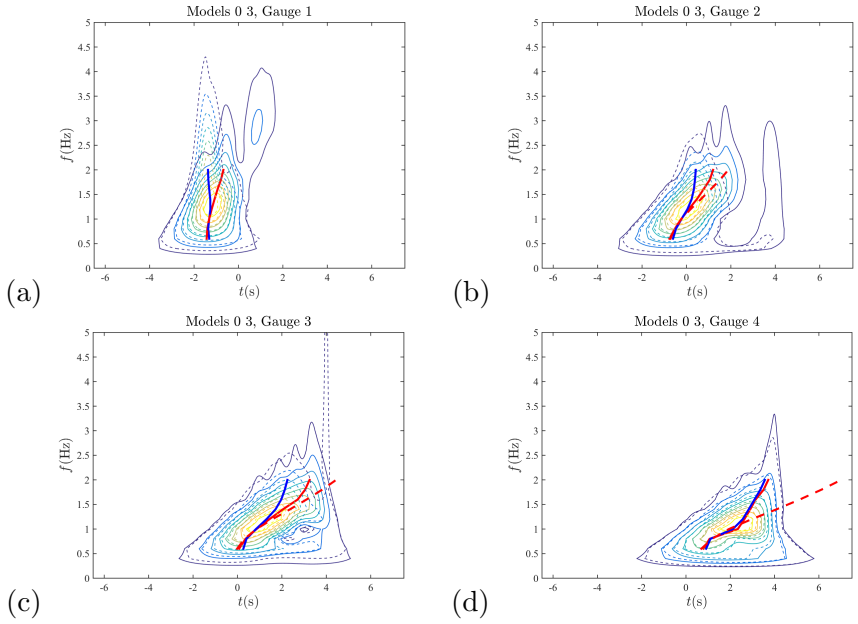

Figure 107: Wavelet transforms and arrival times for Benchmark 4, Model 3 (NHWAVE, granular slide, non-hydrostatic).

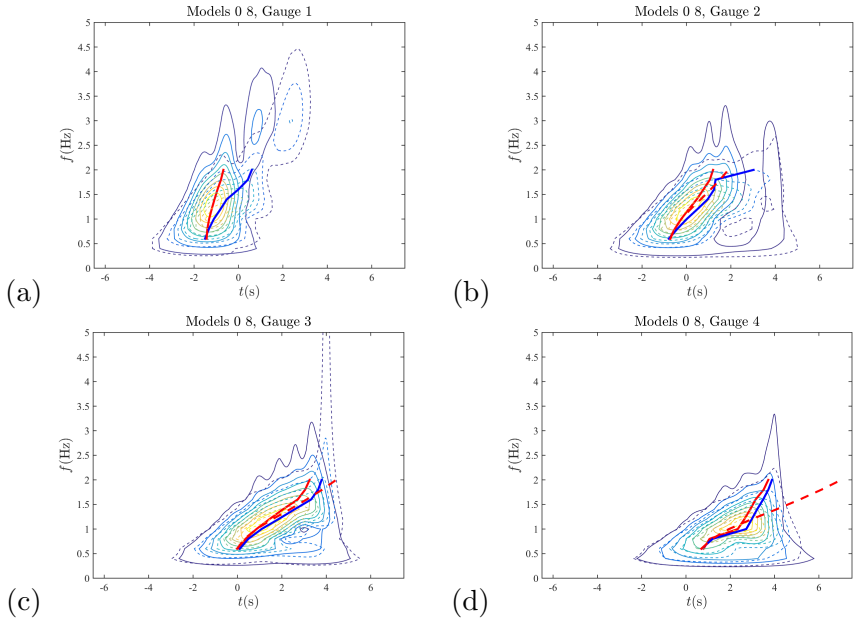

Figure 108: Wavelet transforms and arrival times for Benchmark 4, Model 8 (Tsunami3D, Navier-Stokes, Newtonian rheology).

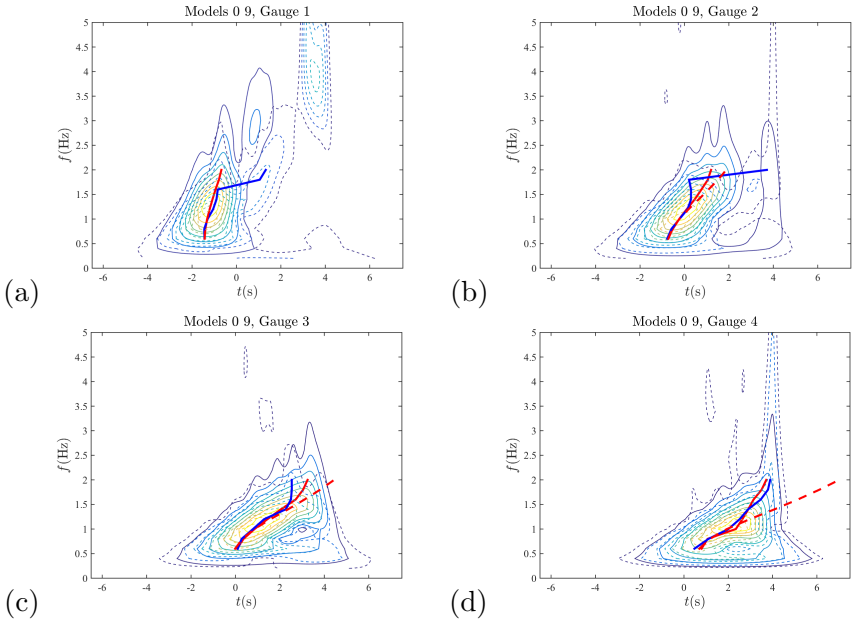

Figure 109: Wavelet transforms and arrival times for Benchmark 4, Model 9 (THETIS, Navier-Stokes, Newtonian rheology).

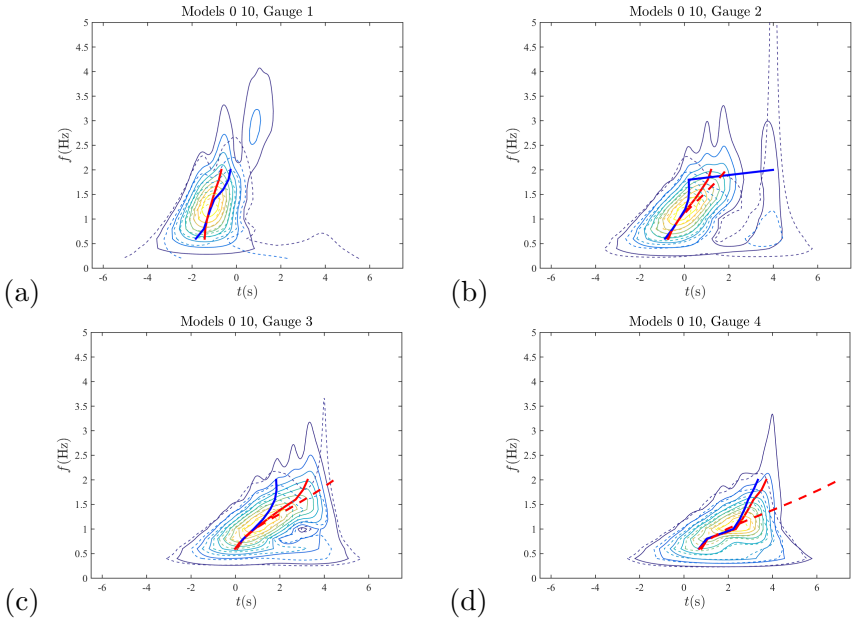

Figure 110: Wavelet transforms and arrival times for Benchmark 4, Model 10 (NHWAVE (3D), Newtonian rheology).

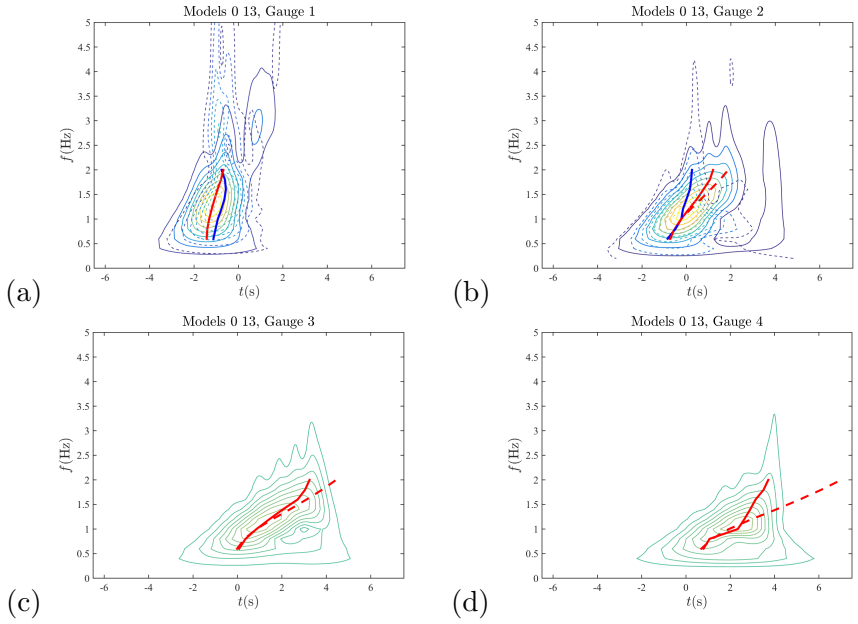

Figure 111: Wavelet transforms and arrival times for Benchmark 4, Model 13 (2LCMFlow, hydrostatic, granular slide).

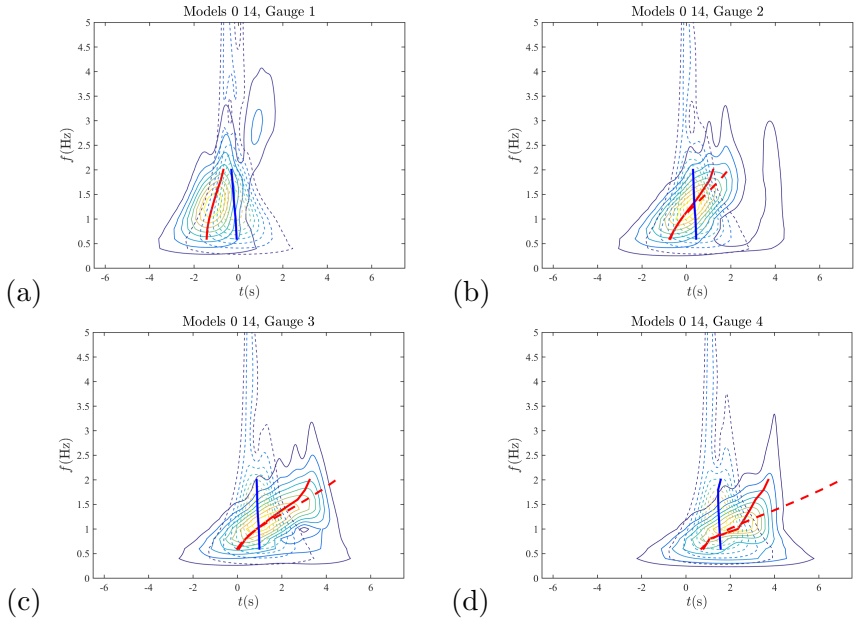

Figure 112: Wavelet transforms and arrival times for Benchmark 4, Model 14 (Alaska GI-L, hydrostatic, viscous slide).

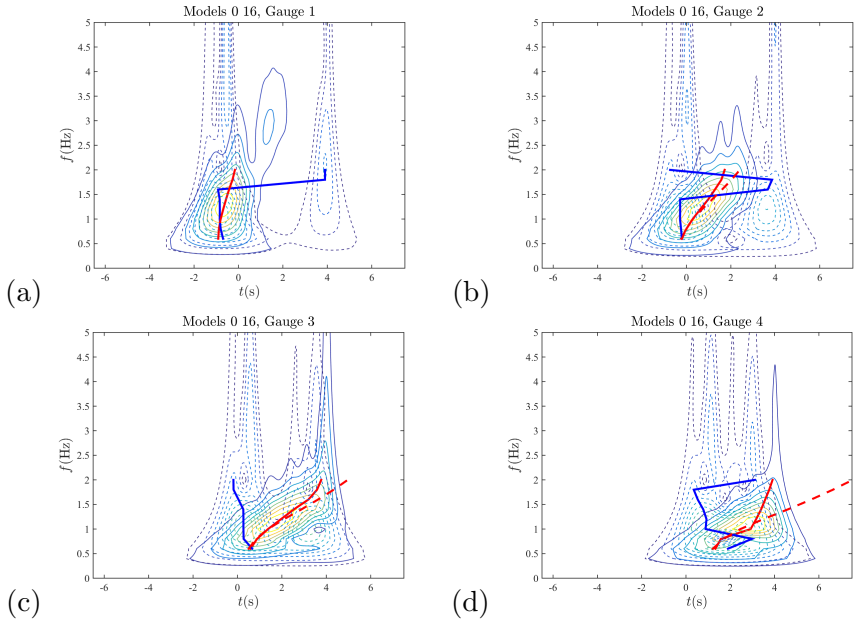

Figure 113: Wavelet transforms and arrival times for Benchmark 4, Model 16 (NHWAVE, hydrostatic, granular slide).

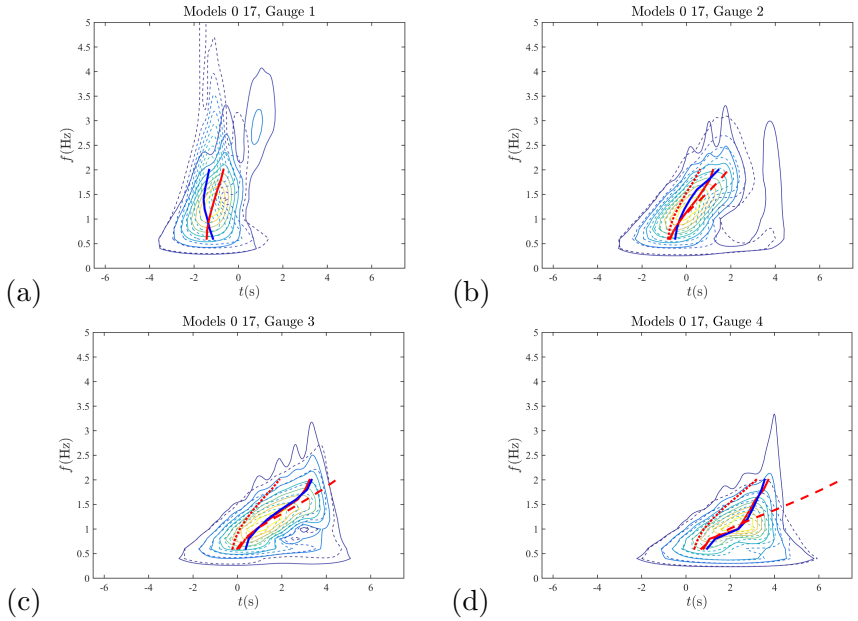

Figure 114: Wavelet transforms and arrival times for Benchmark 4, Model 17 (Landslide-HYSEA, non-hydrostatic, granular slide).